universität wien

DISSERTATION

Titel der Dissertation

„Quantenchemische Untersuchungen von tumorhemmenden Ruthenium(III) Komplexen“

Verfasser

Mag. Ion Chiorescu

angestrebter akademischer Grad

Doktor der Naturwissenschaften (Dr. rer. nat.)

Wien, September 2009

Studienkennzahl lt. Studienblatt:	A 091 419
Dissertationsgebiet lt. Studienblatt:	Chemie
Betreuerin / Betreuer:	O. Univ.-Prof. DDr. Bernhard K. Keppler

universität wien

Ph.D.-Thesis

„Quantum Chemical Studies of Ruthenium(III) Anticancer Complexes“

Written by:

Ion Chiorescu

Vienna, September 2009

This work is based on the following papers and manuscripts:

Quantum Chemical Studies of Ruthenium(III) Anticancer Complexes

Chiorescu, I.; Deubel, D. V.*; Arion, V. B.; Keppler, B. K. *in preparation*.

Computational electrochemistry of ruthenium anticancer agents. Unprecedented benchmarking of implicit solvation methods

Chiorescu, I.; Deubel, D. V.*; Arion, V. B.; Keppler, B. K. *J. Chem Theory Comput.* **2008**, *4*, 499–506.

An electrochemical study of antineoplastic gallium, iron and ruthenium complexes with redox non-innocent α-N-heterocyclic chalcogensemicarbazones

Kowol, C. R.; Reisner, E.*; Chiorescu, I.; Arion, V. B.*; Galanski, M.; Deubel, D. V.; Keppler, B. K. “” *Inorg. Chem.* **2008**, *47*, 11032–11047.

(only theoretical contribution is submitted as part of the thesis)

Supervised by:

Dr. Dirk V. Deubel

Ao. Univ.-Prof. Dr. Vladimir Arion

O. Univ.-Prof. DDr. Bernhard Keppler

Acknowledgment

I would like to acknowledge and thank all the wonderful persons who made possible this thesis to be written.

Dr. Dirk V. Deubel for his supervision and great support, for interesting and helpful discussions. I have learnt a lot of the quantum chemistry along with chemistry and biology since our direct collaboration started in summer 2007. He patiently thought me the theoretical insights and computational approaches to solve difficult problems. During this period I became an expert in finding transition structures of any substitution reaction.

Prof. Vladimir B. Arion for supervision, support and parental advises, for the patience and confidence. For stimulation my work, for proofreading of my texts and posters, for helpful discussions.

Prof. Bernhard K. Keppler for supervision, generous support and for the opportunity to work on this interesting subject in this superb group.

My colleagues Dr. Christian R. Kowol and Dr. Erwin Reisner for fruitful collaboration.

My friends Dr. Alexey A. Nazarov, Dr. Iryna Stepanenko and her husband Andrey, Mag. Anatoly Dobrov, DI. Dr. Ladislav Habala for their support, discussions, out-lab activities etc. etc.

Finally, I would like tot thank my parents, my sister and her husband for their great emotional support during whole this period.

Zusammenfassung

Die vorliegende Dissertation befasst sich mit der Anwendung von quantenchemischen Berechnungen zur Untersuchung von zytostatischen Ruthenium-Komplexen. In den letzten Jahren wurden quantenchemische Methoden erfolgreich auf dem Gebiet der krebshemmenden Metallkomplexe angewendet.

Zu dem Zeitpunkt meiner Doktorarbeit waren die krebshemmenden Ruthenium-Verbindungen nicht ausreichend aus quantenchemischer Sicht untersucht worden, deshalb habe ich mit einem sorgfältigen Methodenvergleich begonnen. Gasphasen-Berechnungen wurden auf dem DFT-Niveau mit Hilfe der ubiquitären B3LYP-Funktional durchgeführt und die Leistungsfähigkeit der von zur Verfügung stehenden Solvatisierungsmethoden für die Berechnung von Standardredoxpotentialen (SRP) wurde verglichen. Demzufolge habe ich die SRP-Werte von Ru(III/II)-Paaren berechnet, deren elektrochemisches Verhalten in der Literatur bereits beschrieben wurde. Ein Vergleich mit experimentellen Werten hat beträchtliche Fehler bei bestimmten Kombinationen von Solvatisierungsmethoden und Solut-Hohlraum ergeben. Zum Beispiel, der absoluter Fehler (mean unsigned eehler, MUE) mit der PCM/UA0-Kombination, die eine Methode der Wahl in Gaussian 03 darstellt, beträgt 0.23 V (5.4 kcal/mol). Die Poisson-Boltzmann Finite-Element-Methode (PBF), implementiert in Jaguar 7 zusammen mit Standard-Hohlraum, liefert geringfügig bessere Ergebnisse mit MUE von 0.16 V (3.7 kcal/mol). Da die betrachteten Redox-Paare eine Ladung von +3/+2 bis –1/-2 tragen und die Voraussage von Solvatisierungsenergien am schwierigsten für hochgeladene Ionen ist, finden diese Ergebnisse Anwendung auch bei DFT-Studien von Reaktionen anderer Metall-Komplexe, die in der Katalyse, Biologie und Medizin involviert sind.

Das erfolgreichste Berechnungsverfahren wurde wie angegeben für das Studium von vier potentiellen tumorhemmenden Ruthenium(III)-Komplexen verwendet (Abbildung): **1** – *trans*-tetrachlorido(dimethylsulfoxid)imidazolruthenat(III) (NAMI-A), **2** – *trans*-tetrachloridobis(1H-imidazol)ruthenat(III) (ICR), **3**- *trans*-tetrachloridobis(1H-pyrazol)ruthenat(III), und **4** – *trans*-tetrachloridobis(1H-indazol)ruthenat(III) (KP1019) und deren reduzierte Analoga. Elektronische Aspekte, die deren elektrochemisches Verhalten bestimmen, wurden untersucht mit Hilfe der Energy Decomposition Analysis und lassen die entscheidende Rolle von π-Elektronen-Akzeptor-Charakter von DMSO- und Indazol-

Liganden bei der Stabilisierung der Ru(II)-Spezies erkennen. Der Einfluss der Elektronen-Donor-Eigenschaften von Protein- und DNA-Modellen mit Direktbindung zum Metall, des mittleren pH-Wertes, und der dielektrischen Konstante auf die SRP-Werte wurde untersucht. Zusätzlich gibt die Studie Aufschluss über den mechanistischen Verlauf des Aquations-Prozesses. In Übereinstimmung mit den verfügbaren experimentellen Daten und im Gegensatz zu einem Teil der früher publizierten quantenchemischen Berechnungen (die für den Aquations-Prozess einen Interchange-Mechanismus von assoziativem Charakter annehmen (**Ia**)), habe ich eine Bevorzugung des stark dissoziativen Interchange-Mechanismus festgestellt (**Id**). Darüber hinaus habe ich zum ersten Mal den limitierenden dissoziativen Mechanismus (**D**) für die Aquation von Ru(II)-Analoga untersucht und dessen Bevorzugung gegenüber dem Austauschmechanismus festgestellt. Der Aquations-Prozess wurde ausführlich untersucht durch die Erstellung der Energie-Profile bis zum zweiten Aquationsschritt. Die Bedeutung von Aquationsprodukten, Mono- und *cis*-Diaquakomplexen, als Vorstufen bei der biologischen Wirkung wurde ausgewertet. Die Kinetik und Thermodynamik von Reaktionen in Bezug auf die Biomodelle wurde berechnet und keine klare Bevorzugung für Stickstoff- oder Schwefelproteinbindungsstellen gefunden. Bei der Bindung zu isolierten Purin-Basen als Modell für die Reaktion mit DNA wurde eine kinetische Präferenz für die Bindung zu Guanin gegenüber Adenin in reduzierten *cis*-Diaqua-Komplexen nachgewiesen; mit Stabilisierung der charakteristischen Übergangszustand durch Wasserstoffbrücken - ähnlich wie bei Reaktionen von Cisplatin. Die Wasserstoffbindung zwischen O6 von Guanin und dem cis-Aqua-Liganden stabilisiert die Reaktionsprodukte in beiden Oxidationszuständen. Die mögliche Beteiligung von Ru(III)-Komplexen am Redox-Kreislauf in den Krebszellen, der eine Produktion von reaktiven Hydroxyl-Radikalen katalysieren kann, wurde ebenfalls erörtert.

Die quantenchemischen Berechnungen wurden angewendet, um die elektronischen Aspekte der Elektrochemie von krebshemmenden Gallium- und Eisenkomplexen mit redox-aktiven α-N-Thiosemicarbazonen zu beschreiben. Die intuitive Annahme, dass die Reduktion von einer Verbindung nach der Bindung zu einem Metallion erleichtert wird, scheint nur dann gültig zu sein, wenn der freie Ligand, in unserem Fall Thiosemicarbazonat, als Referenz-Substanz betrachtet wird, wobei ein Proton die Reduktion von Thiosemicarbazon stärker begünstigt als das Fe(II)-Ion mit seiner d^6-Low-Spin-Konfiguration. Die berechneten Redoxpotentiale korrelieren sowohl mit den berechneten Hirshfeld-Partialladungen auf dem

Thiosemicarbazon-Rest dieser Verbindungen, als auch mit den Energieniveaus deren LUMO-Orbitale.

Die potentiell krebshemmenden Ruthenium(III)-Verbindungen:

1 – *trans*-tetrachlorido(dimethylsulfoxid)imidazolruthenat(III) (NAMI-A), **2** – *trans*-tetrachloridobis(1H-imidazol)ruthenat(III) (ICR), **3**- *trans*-tetrachloridobis(1H-pyrazol)ruthenat(III), und **4** – *trans*-tetrachlorido-bis(1H-indazol)ruthenat(III) (KP1019)

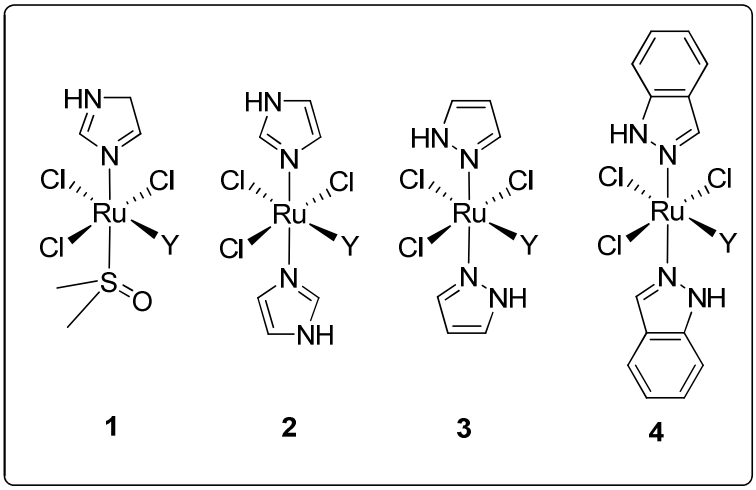

Table of contents

Summary

This thesis focuses on the applications of the computational chemistry methods for the study of ruthenium(III) potential anticancer complexes. Since recently the computational chemistry has emerged the vast area of anticancer metallo-drugs research with great success. Particularly the outstanding contributions were made in the revealing the factors governing the mode of action of cisplatin (the most successful product of the medicinal inorganic chemistry for cancer treatment).

At the moment of starting my thesis, the ruthenium(III) anticancer compounds were neglected by computational chemists, therefore I began with a careful methodological benchmarking. The gas phase calculations were performed at DFT level by using the ubiquitous B3LYP functional and the performances of available solvation methods in the computations of the standard redox potentials (SRPs) have been compared. For this purpose I have calculated SRP values of Ru(III/II) pairs that were electrochemically characterized in the literature. Comparison with experimental data revealed substantial errors in some of the combinations of solvation method and solute cavity. For example, the overall mean unsigned error (MUE) with the PCM/UA0 combination, which is the popular default in Gaussian 03, amounts to 0.23 V (5.4 kcal/mol). The Poisson-Boltzmann finite element method (PBF) implemented in Jaguar 7 together with the default cavity performs slightly better, with the overall MUE being 0.16 V (3.7 kcal/mol). Because the redox pairs considered bear molecular charges from +3/+2 to –1/–2 and the prediction of solvation free energies is most challenging for highly charged species, these results may be used also for DFT studies of the reactions of other metal complexes involved in catalysis, biology, and medicine.

In this way revealed, the most successful computational setup has been used for exploration of the chemical behavior of four potential anticancer ruthenium(III) species (Chart): **1** - *trans*-tetrachlorido(dimethylsulfoxide)imidazoleruthenate(III) (NAMI-A), **2** - *trans*-tetrachloridobis(1H-imidazole)ruthenate(III) (ICR), **3** - *trans*-tetrachloridobis(1H-pyrazole)ruthenate(III), and **4** - *trans*-tetrachloridobis(1H-indazole)ruthenate(III) (KP1019) and their reduced analogs. The electronic aspects governing their electrochemical behavior

have been investigated by using the bond energy decomposition analysis revealing the decisive role of π-electron acceptor character of DMSO and indazole ligands in stabilization of Ru(II) species. Influence of the electron donor properties of the protein and DNA models directly bound to the metal, the medium pH and dielectric constant on the SRPs were examined. Furthermore, the study sheds light into the mechanistic insights of the aquation process. In agreement with experimental data available and contrary to part of the previous computational works (which study the aquation of the Ru(III) species to proceed via an interchange mechanism of associative character (**Ia**)) I found the preference for strong dissociative character of the interchange mechanism (**Id**). Moreover, for the first time I have studied the limiting dissociative mechanism (**D**) of the aquation of Ru(II) analogs and have found it to be prefered over the interchange mechanism. The aquation process was investigated in detail by drawing the energy profiles up to the second aquation step. The importance of aquation products, mono- and *cis*-di-aqua complexes, as precursors for the biological actions is analyzed. The kinetics and thermodynamics of reactions towards biomodels have been computed and no clear preference for either nitrogen or sulfur protein binding sites was found. In the binding to isolated purinic nucleobases, to model the reaction with DNA, the kinetic preference for binding guanine over adenine is found for the reduced *cis*-di-aqua complexes; the characteristic transition structures being stabilized by a hydrogen bonding pattern similar to cisplatin reactions. The hydrogen bond between guanine O6 and *cis*-aqua ligand stabilizes the reaction products in both oxidation states. The possible involvement of Ru(III) complexes in the redox cycling inside the cancer cell that can catalyze the generation of reactive hydroxyl radicals is discussed as well.

The quantum chemical calculations were used to describe the electronic aspects of electrochemistry of antineoplastic gallium and iron complexes with redox non-innocent α-N-heterocyclic thiosemicarbazones. The intuitive assumption that the reduction of a compound is facilitated when it binds to a metal ion appears to be valid only if the *free ligand*, in our case the thiosemicarabazonate, is considered as the reference compound, whereas a proton promotes the reduction of the thiosemicarbazone more strongly than does the iron(II) ion with its d^6 low-spin electron configuration. The computed redox potentials correlate both with the calculated Hirshfeld partial charges on the thiosemicarbazone moieties in these compounds and with the energy levels of their LUMOs.

Potential anticancer ruthenium(III) species:

1 - *trans*-tetrachlorido(dimethylsulfoxide)imidazoleruthenate(III) (NAMI-A), **2** - *trans*-tetrachloridobis(1H-imidazole)ruthenate(III) (ICR), **3** - *trans*-tetrachloridobis(1H-pyrazole)ruthenate(III), and **4** - *trans*-tetrachloridobis (1H-indazole) ruthenate(III) (KP1019)

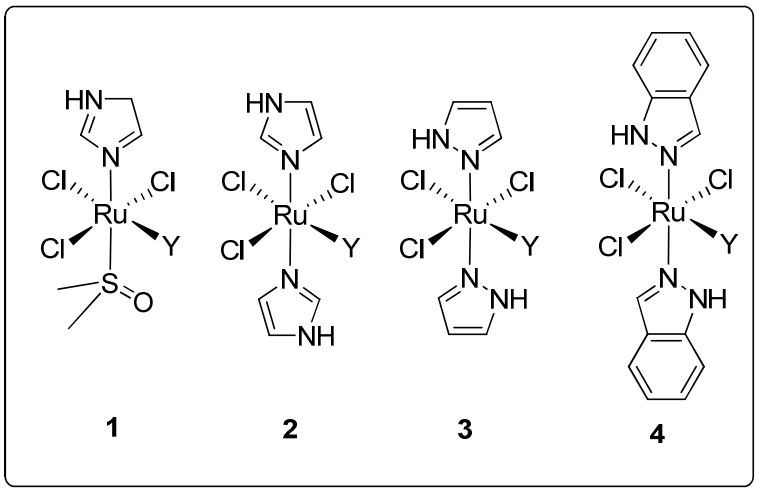

I. Introduction

I.1. Cancer Therapy

Roughly one person in eight in the world will die of cancer.[1] The disease is characterized by the disturbances of the most fundamental rules of behavior of the cells in a multicellular organism. As a result of the failure of growth or division regulatory systems, the affected cells proliferate boundlessly and colonize tissues normally reserved for other cells.[2] The methods of cancer treatment include surgery, radiation therapy, chemotherapy, and immunotherapy. The choice of therapy depends upon the cancer type and the stage of the disease, as well as the general condition of the patient. Complete removal of the affected tissue with least harm to the rest of the body is the treatment goal. The surgery alone is effective mainly in the cases of benign tumors (their cells do not have the ability to invade the surrounding tissue, and stay clustered together in a single mass). In contrast, the malignant tumors have the tendency to invade adjacent tissue or to spread through the bloodstream and lymphatic vessels to form metastasis at other sites of the body, which often limits surgery effectiveness. In such cases the surgery is combined with other methods, and frequently with chemotherapy.

The modern era of cancer chemotherapy[3] started when the war gas sulfur mustard was used in patients in 1931 (abandoned because of high toxicity). The second generation mustard, nitrogen mustard, was tested in the 1940s subsequently in lymphoma treatment first in mice and then in a patient. The result was a dramatic reduction in the patient's tumor masses. Although this effect lasted only a few weeks, this was the first step to the realization that cancer could be treated by pharmacological agents. Since then, a number of drugs (which act as alkylating agents, antimetabolites, mitotic inhibitors, antibiotics or hormones) were approved and largely used in the cancer chemotherapy.[4] Among them metal-based anticancer drugs play a crucial role. Three platinum complexes, cisplatin, carboplatin, and oxaliplatin, which act as alkylating-like agents, are used in about 50% of all tumor therapies, displaying significant therapeutic activity in a series of solid tumors.[5] Chemotherapy acts by killing rapidly dividing cells, one of the main properties of cancer cells. Consequently, the fast-

dividing cells of the body, such as the cells of the bone marrow, digestive tract and hair follicles, are affected, giving rise to a range of side effects. Common side effects associated with chemotherapy include: immunosuppression, anemia and myelosuppression (caused by partial or total destruction of bone marrow), mucositis (inflammation of the lining of the digestive tract), nausea and vomiting, nephrotoxicity, diarrhea or constipation, and alopecia (hair loss). The effectiveness of chemotherapy is often limited by general toxicity to other tissues in the body. The understanding of the mode of action of the anticancer drugs at molecular level is essential to rational drug development.

I.2. Computational Chemistry

Along with physiologists, the chemists actively participate in the mode of action assessment of the drugs. This is possible due to the vast chemical experience and the diversity of physico-chemical methods available for investigation of the microscopic world. Predicting properties of the molecular systems by computer simulations is one of the relatively new methods successfully adopted by chemists. The medium for scientific research in computational chemistry is the computer's processor, the methods are physical models, and the tools are mathematical algorithms. The *in silico* experiments are nowadays used to determine the spatial structures of the molecules, and the obtained electronic information is directly compared with a variety of spectroscopic data (Infrared, Raman and NMR). But most important the computers improve continuously the accuracy in the prediction of microscopic and macroscopic chemical systems behavior otherwise not accessible, or often too expensive for conventional methods. For example computationally can be investigated the reaction intermediates and transition states, which, being crucial species in chemical processes but having a very short lifetime, are difficult to observe experimentally. Thus, experimentally proposed and theoretically possible competing reaction mechanisms can be rigorously investigated by computation chemists. In the humans fight against cancer computational chemistry already proves its distinctive value. The hydrolysis of the most successful metallo-drug cisplatin[6] was rigorously investigated,[7] along with the factors governing its *in vivo* binding preferences and reactivity.[8] The theoretical predictions correlate very well with experimental findings. Despite the fact that ruthenium(III) complexes[9] are known for years to have similar or even better anticancer potency than cisplatin, at the moment of starting my

thesis systematic computational investigation of the ruthenium(III) anticancer drugs was not carried out.

The work is focused on the elucidation of the chemical behavior at molecular level of two ruthenium(III) complexes NAMI-A[10] (imidazolium [*trans*-tetrachlorido(dimethylsulfoxide)imidazoleruthenate(III)]) and KP1019[11] (indazolium [*trans*-tetrachloridobis(1H-indazole)ruthenate(III)]) (Chart 1) which successfully completed phase I clinical trials.[12] Chapter II has been entirely dedicated to the basic theoretical and computational concepts used in the study. In chapter III the systematic benchmarking of the available solvation models by predicting redox potentials of ruthenium(III) complexes is presented. In chapter IV, by using carefully benchmarked method, an *in silico* four-species-evolution approach which includes *trans*-tetrachloridobis(1H-imidazole)ruthenate(III) (ICR) and *trans*-tetrachloridobis(1H-pyrazole)ruthenate(III) to rationally connect NAMI-A and KP1019 has been used to investigate the behavior of potential ruthenium(III) anticancer drugs. In this sense, along with aquation, the reactions of the selected compounds with biological protein and DNA models have been investigated, in both the kinetic and thermodynamic aspects. In chapter V an example of the use of the computational methods to analyze the electrochemistry of some metal complexes with non-innocent α-N-heterocyclic chalcogensemicarbazones is presented.

Chart 1. NAMI-A and KP1019, successful Ru(III) anticancer complexes in clinical trials.

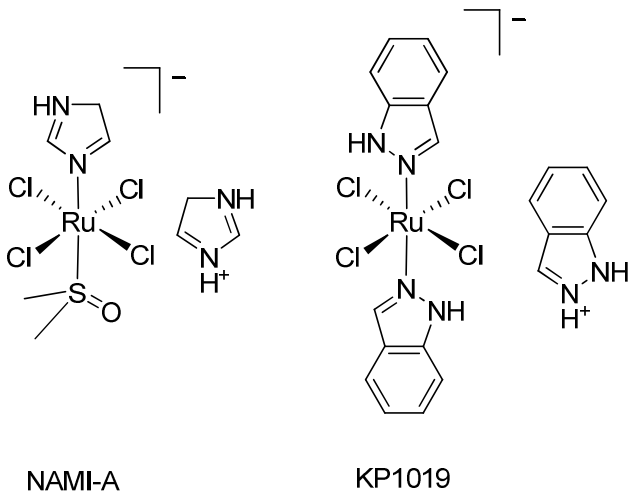

NAMI-A KP1019

I.3. References

(1) World Health Organization: http://www.who.int/. (Accessed on June 13th 2009: http://www.who.int/entity/healthinfo/global_burden_disease/GBD_report_2004update_part2.pdf; Figure 4).

(2) Alberts. B.; Bray, D.; Lewis, J.; Raff, M.; Roberts, K.; Watson, J. D. *Molecular biology of the cell* Garland Publishing, Inc. New York, 1994, p. 1255.

(3) DeVita, V. T.; Chu, E. *Cancer Res.* **2008**, *68*, 8643.

(4) National Cancer Institute (NCI) web page, accessed on June 13th 2009. http://www.cancer.gov/cancertopics/druginfo/alphalist;

(5) (a) Hambley, T. W. *Science* **2007**, *318*, 1392. (b) Jakupec, M. A.; Galanski, M.; Arion, V. B.; Hartinger, C. G.; Keppler, B. K. *Dalton Trans.* **2008**, *2*, 183.

(6) (a) Jamieson, E. R.; Lippard, S. J. *Chem. Rev.* **1999**, *99*, 2467. (b) Fuertes, M. A.; Alonso, C.; Pérez, J. M. *Chem. Rev.* **2003**, *103*, 645. (c) Jakupec, M. A.; Galanski, M.; Keppler, B. K. *Rev. Physiol. Bioch. Pharmacol.* **2003**, *146*, 1. (d) Jung, Y.; Lippard, S. J. *Chem. Rev.* **2007**, *107*, 1387.

(7) (a) Zhang, Y.; Guo, Z. J.; You, X. Z. *J. Am. Chem. Soc.* **2001**, *123*, 9378. (b) Cooper, J.; Ziegler, T. *Inorg. Chem.* **2002**, *41*, 6614 (c) Robertazzi, A.; Platts, J. A. *J. Comput. Chem.* **2004**, *25*, 1060. (d). Burda, J. V.; Zeizinger, M.; Leszczynski, J. *Comput. Chem.* **2005**, *26*, 907. (e) Lau, J. K.-C.; Deubel, D. V. *J. Chem. Theory Comput.* **2006**, *2*, 103.

(8) (a) Baik, M.-H.; Friesner, R. A.; Lippard, S. J. *J. Am. Chem. Soc.* **2002**, *124*, 4495. (b) Deubel, D. V. *J. Am. Chem. Soc.* **2002**, *124*, 5834. (c) Baik, M.-H.; Friesner, R. A.; Lippard, S. J. *J. Am. Chem. Soc.* **2003**, *125*, 14082. (d) Deubel, D. V. *J. Am. Chem. Soc.* **2004**, *126*, 5999. (e) Deubel, D. V. *J. Am. Chem. Soc.* **2006**, *128*, 1654. (f) Mantri, Y.; Lippard, S. J.; Baik, M.-H. *J. Am. Chem. Soc.* **2007**, *129*, 5023.

(9) Clarke, M. J. *Coord. Chem. Rev.* **2003**, *236*, 209.

(10) (a) Mestroni, G.; Alessio, E.; Sava, G.; Pacor, S.; Coluccia, M. In *Metal Complexes in Cancer Chemotherapy*. Keppler, B. K., Ed.; VCH: Weinheim, Germany, 1993, p. 157. (b) Sava, G.; Capozzi, I.; Clerici, K.; Gagliardi, R.; Alessio, E.; Mestroni, G. *Clin. Exp. Metastasis* **1998**, 16, 371. (c) Sava, G.; Alessio, E.; Bergamo, A.; Mestroni, G. *Top. Biol. Inorg. Chem.* **1999**, *1*, 143. (d) Alessio, E.; Mestroni, G.; Bergamo, A.; Sava, G. In *Metal*

Ions in Biological Systems. Sigel, A.; Sigel, H., Ed.; Marcel Dekker: New York, 2004, Vol. 42, p 323.

(11) (a) Keppler, B. K.; Rupp, W.; Juh, U. M.; Enders, H.; Niebl, R.; Balzer, W. *Inorg. Chem.* **1987**, *26*, 4366. (b) Keppler, B. K.; Berger, M. R.; Heim, M. H. *Cancer Treatments Rev.* **1990**, *17*, 261.

(12) (a) Galanski, M.; Arion, V. B.; Jakupec, M. A.; Keppler, B. K. *Curr. Pharm. Des.* **2003**, *9*, 2078. (b) Rademaker-Lakhai, J. M.; van den Bongard, D.; Pluim, D.; Beijnen, J. H.; Schellens, J. H. M. *Clin. Cancer Res.* **2004**, *10*, 3717. (c) Hartinger, C. G.; Zorbas-Seifried, S.; Jakupec, M. A.; Kynast, B.; Zorbas, H.; Keppler, B. K. *J. Inorg. Biochem.* **2006**, *100*, 891.

II. Theory

The chapter presents the basic concepts of the total energy calculation methods, in particular **DFT**, an overview of the solvation computational models, and shortly the structure optimization techniques used in molecular modeling. More information is available in excellent introductory manuals on the theory and applications of computations in chemistry and physics.[1]

II.1. Total Energy Calculation

The ground state properties of a molecular system are determined by the interactions between the electrons and nuclei and to describe these interactions it is necessary to use quantum mechanics. The nuclear Hamiltonian, $\hat{H}_n$, and the electronic Hamiltonian, $\hat{H}_e$, fully describe the molecular system in the *Schrödinger* equation:

$$(\hat{H}_n + \hat{H}_e)\Psi = E\Psi \tag{1}$$

where E is the total energy, $\Psi = \Psi(x_1, x_2, ..., x_n)$ is the wave function, and $\hat{H}$ is the Hamiltonian operator. Because the fundamental interaction at the atomic level is the electrostatic *Coulomb* interaction, along with kinetic component describing the particles motion, the Hamiltonian contains the electrostatic components. The electronic Hamiltonian has the form:

$$\hat{H}_e = -\frac{1}{2}\sum_i \nabla_i^2 - \sum_\alpha \sum_i \frac{Z_\alpha}{r_{i\alpha}} + \sum_{i,j>i} \frac{1}{r_{ij}} \tag{2}$$

where the three terms are the electron's kinetic energy, and electrostatics: the electron-nuclei and the electron-electron interaction. Despite the fact that the interactions make this equation

impossible to solve completely, manageable equations are obtained by using approximations. The adiabatic or *Born-Oppenheimer* approximation assumes that the electrons respond instantaneously to heavy nuclei motion and thus the total wavefunctions can be factorized into separate wavefunctions for the electrons and the nuclei respectively:

$$\Psi_T = \Psi_e * \Psi_n \tag{3}$$

The contributions to the electronic energy E_e of an N-electron molecular system consisting of α type nuclei, in the **HF** methods are:

$$\begin{aligned}
E_e &= E_T + E_V + E_J + E_X + E_C \\
E_T &= -\frac{1}{2}\sum_m^N \int dx_1 \chi_m^*(x_1)\nabla^2\chi_m(x_1) \\
E_V &= -\sum_m^N \int dx_1 \chi_m^*(x_1)\sum_\alpha \frac{Z_\alpha}{r_{1\alpha}}\chi_m(x_1) \\
E_J &= \frac{1}{2}\sum_m^N\sum_n^N \int dx_1 dx_2 \chi_m^*(x_1)\chi_n^*(x_2)\frac{1}{r_{12}}\chi_m(x_1)\chi_n(x_2) \\
E_X &= -\frac{1}{2}\sum_m^N\sum_n^N \int dx_1 dx_2 \chi_m^*(x_1)\chi_n^*(x_2)\frac{1}{r_{12}}\chi_n(x_1)\chi_m(x_2) \\
E_C &= 0
\end{aligned} \tag{4}$$

where E_T is the kinetic energy of electrons, E_V represents nuclei-electrons electrostatic interaction, and E_J is classic electrostatic interaction between electrons. The last two components describe the electron correlation: a pure quantum phenomenon that take into account the interactions between electrons, others than motion and classical electrostatics. E_X is the electron exchange component of energy (so called *Fermi correlation*) describes the correlation between electrons with parallel spin. This prevents the parrallel-spin electrons from being found at the same point in space. On the other hand, the second quantum term E_C (*Coulomb correlation*) describes the correlation between the spatial positions of electrons with opposite spin due to their *Coulomb* repulsion. The *Coulomb correlation* energy is not possible to describe within the *Hartree-Fock* **HF** approach. Numerically this term is equal to

the difference between the exact total energy of the system and the energy calculated at **HF** level using a complete basis set.

II.2. Density Functional Theory

The basis for the *Density Functional Theory* (**DFT)** is the proof by Hohenberg and Kohn[2] that the ground state electronic energy is determined completely by the electron density $\rho(r)$. While **DFT** is conceptually and computationally very similar to *Hartree–Fock* theory, it became popular due to results quality, and computational accessibility of large electronic systems. The significance of the *Hohenberg–Kohn* theorem is perhaps best illustrated by comparing it with the wave function approach. While the complexity of a wave function increases exponentially with the number of electrons, the electron density has the same number of variables, independent of the system size. A wave function for an N-electron system contains $4N$ variables: three spatial and one spin coordinate for each electron. The electron density being the square of the wave function, integrated over $N-1$ electron coordinates, has each spin density depending on three spatial coordinates, independent of the number of electrons (eq. 5). Although it has been proven that different density yields a different ground state energy, the functional connecting these two quantities is not known. The goal of **DFT** methods is to design functionals connecting the electron density with the energy.

$$\rho(r) = N\int\left|\Psi(r, r_2, \ldots r_N)\right|^2 dr_2 \ldots dr_N \qquad (5)$$

II.2.1. The Energy Functional and Energy Calculations in DFT

According to Kohn and Sham[3] the energy functional $E[\rho(r)]$ can be written as:

$$E[\rho(r)] = E_T + E_V + E_J + E_{XC} = \\ -\frac{1}{2}\int \nabla^2 \rho(r) d(r) + \int V(r)\rho(r) d(r) + \frac{1}{2}\int \frac{\rho(r)\rho(r')}{|r-r'|} d(r) d(r') + E_{XC}[\rho(r)] \quad (6)$$

where E_T is the kinetic energy of non-interacting electrons followed by the energy contribution from the interaction of electrons with the external nuclear potential $V(r)$, the electron-electron interaction term, and the last term $E_{XC}[\rho(r)]$ represents the exchange-correlation functional. Using the electron density as a parameter, there is a variational principle analogous to that in wave mechanics, i.e. given an approximate electron density $\rho(r)$ (assumed to be positive definite everywhere) that integrates to the number of electrons, the energy given by this density is an upper bound to the exact ground state energy, provided that the exact functional is used:

$$E_0 = E[\rho_0(r)] \leq E[\rho(r)] \quad (7)$$

The total energy functional for the interacting many-particle system can be transformed into a set of one-particle equations, called the *Kohn-Sham* (**KS**) equations. By using a set of one-electron orbitals:

$$\rho(r) = \sum_i |\varphi_i(r)|^2 \quad (8)$$

and Lagrange multipliers for constraining the system to a fixed number of atoms, the **KS** are:

$$\left[-\frac{1}{2}\nabla^2 + V_{eff}(r)\right]\varphi_i = \varepsilon_i\varphi_i \tag{9}$$

The effective potential $V_{eff}(r)$ (eq. 10) has a contribution from the nuclei-electron interaction, while the electron-electron interaction is divided into the *Hartree* term and the correlation potential $V_{XC}(r)$.

$$V_{eff}(r) = V(r) + \int \frac{\rho(r')}{|r-r'|}dr' + \mathrm{V_{XC}}(r) \tag{10}$$

The problem of finding the ground state of a molecule becomes a mean field problem where non-interacting electrons are moving in an effective potential of other electrons. Eq. 9 is solved *self-consistently* and the ground state electron density is determined by eq. 8. The *self-consistent scheme* is an iterative process to obtain the correct electron density of the molecular ground state. This is achieved by assigning trial wave functions which are used to calculate first the electron density $\rho(r)$, by eq. 8, then V_{eff} by eq. 10 and V_{eff} are then inserted into the *Kohn-Sham* equations. New trial wave functions are generated by solving the **KS** equations and the procedure is repeated until the convergence is achieved. The sum over the occupied one-electron energies ε_i has to be corrected with a Coulomb and an exchange-correlation term to give the correct total energy:

$$E[\rho(r)] = \sum_i \varepsilon_i - \frac{1}{2}\int \frac{\rho(r)\rho(r')}{|r-r'|}drdr' + \int \rho(r)[E_{XC}[\rho(r)] - V_{XC}(\rho(r))]dr \tag{11}$$

II.2.2. The Exchange-Correlation Functional

Theoretically, the *Kohn-Sham* equations yield the exact ground-state energy by using the exact forms of E_{XC} and V_{XC}. However, these two quantities are only approximate challenging the scientists to carefully choose the available functionals for their specific purpose. The diversity of the functional forms to derive the exchange correlation energy determines the difference between various **DFT** methods.

The simplest model is the *Local Density Approximation* (**LDA)**, where the electron density is assumed to be slowly varying, such that the density can be locally treated as a uniform gas: *homogeneous electron gas*, also known as *jellium*, is a quantum mechanical model of interacting electrons within an infinite volume of space and neutralized with a uniformly distributed background positive charge. For a spin-unpolarized system, a *local density approximation* for the exchange-correlation functional is written as:

$$E_{XC}^{LDA}[\rho(r)] = \int \rho(r)\varepsilon_{XC}(\rho(r))dr \qquad (12)$$

where $\rho(r)$ is the electronic density and ε_{xc} is the exchange-correlation energy function of the density alone. The exchange-correlation energy is decomposed into exchange and correlation terms linearly:

$$E_{XC} = E_X + E_C \qquad (13)$$

The exchange term takes on a simple analytic form for the homogeneous electron gas:

$$E_X^{LDA}[\rho(r)] = -\frac{3}{4}\left(\frac{3}{\pi}\right)^{1/3}\int \rho(r)^{4/3}\,dr \tag{14}$$

The correlation energy is calculated by *Quantum Monte Carlo* methods. Although the **LDA** method is based on a very crude model, it provides results which are in general comparable or even better than those calculated by methods based on the Hartree-Fock approximation. Improvements over the **LDA** approach must consider a non-uniform electron gas.

In methods based on the *Generalized Gradient Approximation* (**GGA**), the dependence of exchange-correlation energy on the local density gradient is used along with the local electron density:

$$E_{XC}^{GGA}[\rho(r)] = \int \rho(r)\varepsilon_{XC}(\rho(r),\nabla\rho(r))dr \tag{15}$$

Various **GGA** functionals use different representations of ε_{xc} functions. Although there are cases when **LDA** perform better than **GGA**, the later improve considerable the description of some molecular properties (e.g. the binding energies). One of the earliest and most popular **GGA** exchange functionals was proposed by A. D. Becke[4] (B or B88) as a correction to the **LSDA** exchange energy (**LDA** for spin polarized systems):

$$\begin{aligned}
&\varepsilon_X^{B88} = \varepsilon_X^{LDA} + \Delta\varepsilon_X^{B88} \\
&\Delta\varepsilon_X^{B88} = -\beta\rho^{1/3}\frac{x^2}{1+g\beta x\sinh^{-1}x} \\
&x = \frac{|\nabla\rho|}{\rho^{4/3}}
\end{aligned} \tag{16}$$

The β parameter was determined by fitting to known data for the rare gas atoms using the dimensionless gradient variable *x*. It reduces the error in the exchange energy by almost two orders of magnitude relative to the **LSDA** results and thus represents a substantial improvement for a simple functional form containing only one adjustable parameter. There have similarly been various **GGA** functionals proposed for the correlation energy. One popular functional is due to Lee, Yang and Parr (LYP).[5] The LYP correlation functional is often combined with the B88 exchange functional to produce the BLYP.

The next generation of **GGA** methods is higher order gradient, or ***meta*-GGA**, methods which are characterized by the introduction of higher order derivatives of the electron density in the description of the exchange-correlation function.

Models that include exact **HF** exchange are denoted by *hybrid* methods, the *Becke 3 parameter functional* (B3) methods is example of such hybrid models, with the popular B3LYP method[5,6] defined by:

$$E_{XC}^{B3LYP} = (1-a)E_X^{LSDA} + aE_X^{exact} + bE_X^{B88} + (1-c)E_C^{LSDA} + cE_C^{LYP} \qquad (17)$$

The *a*, *b* and *c* parameters were determined by fitting to experimental data and depend on the chosen forms for E_X^{GGA} and E_C^{GGA}, with typical values being *a* ~ 0.2, *b* ~ 0.7 and *c* ~ 0.8. The usage of **GGA** and *hybrid* functionals yields to major improvement in terms of accuracy for chemical applications. At the moment the B3LYP functional proposed in 1993 is one of the most successful in terms of overall performance. Although the performance might be improved by fitting different combinations of exchange and correlation functionals to experimental data for a given property, such measures often result in the deterioration of the results for other properties.

II.2.3. Basis Set and Effective Core Potential Approximation

The single particle wave functions used to derive the electron density in eq. 8 are expanded into a *linear combination or atomic orbitals* (**LCAO**) χ_m according to:

$$\varphi_i(r) = \sum_m C_m^i \chi_m(r) \tag{18}$$

In principle any type of basis functions χ_m may be used for molecular calculations: exponential, Gaussian, polynomial, cubic functions, wavelets, plane waves, etc. A successful set of basis functions has two main characteristics: (i) the functions should have a physical reasonable behavior, and converge rapidly as more basis functions are added. For atomic and molecular systems, functions should go toward zero as the distance between the nucleus and electron becomes large. (ii) the functions should make it easy to calculate all the required integrals. The exponential functions are known to be the exact solution for the hydrogen atom. They are used to build the *Slater type orbitals* (**STO**s) (eq. 19), which decay exponentially from their origin. Despite the fact that **STO**s describe better the behavior of atomic wave functions, the *Gaussian type orbitals* (**GTO**s) (which have a Gaussian behavior, eq. 20) are much easier to handle numerically and they are preferred in the **DFT** calculations as much as in conventional *ab initio* techniques.

$$\chi^{STO}(r,\theta,\varphi) = Nr^{n-1}e^{-\zeta r}Y_l^m(\theta,\varphi) \tag{19}$$

$$\chi^{GTO}(r,\theta,\varphi) = Nr^{2n-2-l}e^{-\zeta r^2}Y_l^m(\theta,\varphi) \tag{20}$$

Another aspect to take into account, when choosing the computational level to estimate the total energy of a molecular system, is the increase of the number of core electrons, unimportant in the chemical sense, with the rise of atomic number. In such cases the valence orbitals use a large number of basis functions to adequately account for electron-

electron repulsion. Even more troubles arise in the lower half of periodic table where the relativistic effects further complicate the systems. The approach to solve these problems is to model the core electrons by a suitable function and to treat only the valence electrons explicitly. The usage of *Effective Core Potential* (**ECP**) became a common approach that gives good result at a fraction of the cost of a calculation involving all electrons, and part of the relativistic effects may also be accounted, without having to perform the full relativistic calculation. The potential have its parameters fitted such that the solutions of the Schrödinger equation produce pseudo-orbitals matching the all-electron valence orbitals.

II.2.4. DFT Limitations

In the treatment of the following systems the current DFT functionals are known to perform poorly[1b]:

(i) The weak interactions due to dispersion forces, which arise from electron correlation in wave function methods, are poorly described by current **DFT** methods.[7] However, the mainly electrostatic nature makes the hydrogen bonded systems well described by many **DFT** functionals.

(ii) Loosely bound electrons, such as anions arising from systems with relatively low electron affinities, represent a problem for exchange–correlation functionals that do not include self-interaction corrections. Since these electrons have most of the associated density far from the nuclei, this may cause the self-interaction error to be larger than the actual binding energy, and thus lead erroneously to an unbound electron. Nevertheless, even a single set of diffuse functions added to a medium-sized basis set will give a reasonable estimate of the experimental electron affinity.[8] The basis set limits the outer electron to be in the correct physical space, and the exchange–correlation functional gives a reasonable estimate of the energy of this density.

(iii) Chemically bonded systems involving: two-centre two-electrons (e.g. normal covalent bonds), two-centre four-electrons (e.g. steric repulsion between closed shell systems), and three-centre three-electrons (e.g. radical abstraction) are reasonably described by gradient-corrected methods. On the other hand systems involving: two-centre one-electron (e.g. radical cations), two-centre three-electrons (e.g. radical anions), and three-centre four electrons (e.g.

atom transfer transition structures) are predicted to be too stable.[9] The dissociation of charged odd-electron systems is a problem for most **DFT** methods, with the dissociation energy profile displaying an artificial barrier and incorrect dissociation energy. Transition structures are similarly predicted to be too stable (barriers are underestimated) by functionals that do not include exact exchange. Since *Hartree–Fock* overestimates activation barriers, the hybrid methods involving exact exchange, often give reasonable barriers.

(iv) The exchange–correlation functional is local, depending only on the density and possibly its derivatives at a given point, and this causes **DFT** methods to be unsuitable for describing charge transfer systems, where an electron is transferred over a large distance.

(v) In **HF** theory the energy difference between states with different spin multiplicity with the same orbital occupancy is given by an exchange integral. In **DFT**, this must be described by the exchange–correlation functional, which only depends on the electron density. If the two spin states arise from the same electron configuration the two electron densities are very similar, and this makes the results sensitive to the details of the exchange–correlation functional. In transition metal systems, where several low-energy spin states are often possible, **HF** favors high spin states (HS) while **KS** methods favor low spin states (LS). Hybrid methods perform differently depending on the studied system. For example, the authors of ref. 10 found the PBE0[11] functional (which includes *ab initio* estimate of the hybrid mixing of exact and **GGA** exchange) to perform best for computing the HS-LS energy difference in Fe(II) complexes with small ligands ($[Fe(H_2O)_6]^{2+}$ and $[Fe(NH_3)_6]^{2+}$). While the widely employed B3LYP (which uses without reoptimization the three semi-empirical coefficients fitted for experimental data together with PW91[12] correlation) performs only acceptable. The authors in ref. 13 preferred the BP86[4,14] over B3LYP in the computations on zirconium(IV) complexes. The overestimation of the contribution of exchange energy by the B3LYP functional is well documented and the fitting of the mixing coefficients was proposed to overcome the problem.[15]

II.3. Electron Population Analysis

Except the energy, another property derived after determining the electronic wave function is the atomic electron population which is often used for discussing and rationalizing structural and reactivity differences between molecules. There are three commonly used methods for assigning a charge to a given atom.[1b]

II.3.1. Population Analysis Based on Basis Functions

The *Mulliken Population Analysis*[16] is an example of method using basis functions to derive the electron population. The scheme uses *DS* matrix[17] for distributing the electrons into atomic contributions. The diagonal element $D_{mm}S_{mm}$ is the number of electrons in the *m* atomic orbital (AO), and an off-diagonal element $D_{mn}S_{mn}$ is (half) the number of electrons shared by AOs *m* and *n* (there is an equivalent $D_{nm}S_{nm}$ element). The contributions from all AOs located on a given atom *A* may be summed up to give the number of electrons associated with atom *A*. In the *Mulliken* scheme the contribution involving basis functions on different atoms are equally divided between the two atoms:

$$\rho_A = \sum_{m \in A} \sum_{n} D_{mn} S_{mn} \tag{21}$$

With the gross charge in atom *A* being the sum of the nuclear and electronic contributions:

$$Q_A = Z_A - \rho_A \tag{22}$$

II.3.2. Population Analysis Based on the Electrostatic Potential

A significant part of the non-bonded interaction between polar molecules is described in terms of electrostatic interactions between fragments with different electron distribution. The fundamental interaction is between the *Electrostatic Potential*[18] (ESP) generated by one molecule (or fragment) and the charged fragments of another. The ESP at position *r* is given as a sum of contributions from the nuclei and the electronic wave function:

$$\Phi_{ESP}(r) = \sum_{A}^{nuclei} \frac{Z_A}{|r - R_A|} - \int \frac{|\Psi(r_i)|^2}{|r - r_i|} dr_i \qquad (23)$$

The potential is sampled by placing a suitable grid of points around each nucleus (typical sampling have a few hundred points for each atom) with distances from just outside the van der Waals radius to about twice that distance. The atomic charges are determined as those parameters that reproduce the electrostatic potential as closely as possible at these points, subject to the constraint that the sum is equal to the total molecular charge.

II.3.3. Population Analysis Based on the Electron Density

The electron density is the square of the wave function integrated over N_{elec}*-1* coordinates (eq. 5). If the total molecular volume could somehow be divided into subsections, each belonging to one specific nucleus, then the electron density could be integrated to give the number of electrons present in each of these atomic basins Ω, and the (net) atomic charge *Q* is then obtained by adding the nuclear charge *Z*:

$$Q_A = Z_A - \int_{\Omega_A} \rho(r) dr \qquad (24)$$

The division into atomic basins requires a choice to be made as to whether a certain point in space belongs to one nucleus or another, and several different schemes have been proposed.

The *Atoms in Molecules* (AIM)[19] is the most rigorous way of dividing a molecular volume into atomic subspaces. In the large majority of cases it is found that the only maxima in the electron density occur at the nuclei (or very close to them), which is reasonable since they are the only sources of positive charge. The nuclei thus act as attractors of the electron density. At each point in space the gradient of the electron density points in the direction of the strongest (local) attractor. This forms a rigorous way of dividing the physical space into atomic subspaces: starting from a given point in space a series of infinitesimal steps may be taken in the gradient direction until an attractor is encountered. Once the molecular volume has been divided up, the electron density may be integrated within each of the atomic basins to give atomic charges and dipole, quadrupole, etc., moments.

Hirshfeld[20] charges are obtained by using atomic densities for partitioning the molecular electron density:

$$\rho_{At}(r) = \frac{\rho_{At}^{0}(r)}{\sum_{i}^{At} \rho_{i}^{0}(r)} \rho_{Mol}(r) \qquad (25)$$

The initial (promolecular) density ρ_{Mol}^{0} is defined as the sum of atomic densities ρ_{At}^{0} placed at the nuclei in the molecule. The actual molecular electron density at each point in space $\rho_{Mol}(r)$ is then partitioned by weighting factors according to the original contributions.

II.4. Bond Energy Analysis

To characterize the bonding between the entities (fragments) of a molecular system I have analyzed the molecules in terms of interactions between two fragments using an energy decomposition scheme developed by Ziegler and Rauk[21] as implemented in ADF.[22] The overall bonding energy between two fragments, ΔE, is decomposed in:

$$\Delta E = \Delta E_{prep} + \Delta E_{\text{int}} = \Delta E_{prep} + \Delta E_{elst} + \Delta E_{Pauli} + \Delta E_{orb} \qquad (26)$$

where ΔE_{prep} is the preparation energy required to deform the separated fragments from their equilibrium structure to the geometry in the molecule, including the excitation to their valence electronic configuration; ΔE_{int} is the interaction energy, and includes: repulsion between fragments due to Pauli principle ΔE_{Pauli}, electrostatic component ΔE_{elst}, and stabilizing orbital interactions ΔE_{orb}. The orbital interaction energy accounts for electron pair bonding, charge transfer and polarization. This can be further decomposed into the contributions from the irreducible representations Γ of the interacting system.[22a]

II.5. Solvation Models

In the previous parts I presented very briefly the theoretical and computational consideration to evaluate the total energy of a molecular system in gas phase. As the processes which I have been investigated during the thesis preparation take place mostly in solution, the following chapter contains the important aspects of computational environment modeling, in particular the consideration of solvent effects. The effects of solvation can be partitioned into two main groups: (i) non-specific (long-range) solvation and (ii) specific (short-range) solvation. The non-specific effects are mainly solvent polarization and orientation of the solvent electric multipole moments by the solute, where the dipole interaction is usually the most important. The specific (microscopic) interactions are

primarily located in the first solvation shell, at the solute-solvent boundary surface, although the second solvation shell may also be important for highly-charged ions. The microscopic interactions depend on the specific nature of the solvent molecule, such as the shape and the ability to form hydrogen bonds. Other short-range solvation effects to take into account are: van der Waals interactions solute-solvent, the charge transfer effects, hydrophobic or entropic effects, etc. The methods for solvation computation are mostly of two types: those describing explicitly the individual solvent molecules and those that treat the solvent as a continuous medium. A partial mixing of the models is also possible, for example by treating explicitly the first solvation shell and considering the rest of the solvent as a continuum model. The first class of methods involving an explicit use of the solvent molecules requires a sampling of the phase space. Since this is computationally expensive, there is a strong interest in developing methods where the solvent is modeled in a less rigorous fashion.

II.5.1. Continuum Solvation Models

In the continuum or implicit solvation models[23] the solvent is considered as a uniform polarizable medium with a dielectric constant of ε, and the solute is placed in a suitably shaped cavity in the medium. The solvation free energy has three main terms (eq. 27): (i) the cavitation is a destabilization component, since the making of a hole in ordered medium costs energy; (ii) the stabilization component due to the dispersion interactions; and (iii) electrostatic stabilization that appears as consequence of medium polarization induced by the charge distribution in the solute. The dispersion term is sometimes denoted as dispersion/repulsion as the interaction between the solute and solvent might have a repulsive component as well.

$$\Delta G_{solvation} = \Delta G_{cavity} + \Delta G_{dispersion} + \Delta G_{elec} \qquad (27)$$

Beside the differences in the way to define the size and the shape of the cavity, the continuum models also differ in calculation methods of the cavity/dispersion contributions, the approach to describe the solute and its charge distribution, as well as in different description of the dielectric continuum. The solvent medium is normally taken to have a

constant value of ε, but may for some purposes also be taken to depend for example on the distance from solute. It should be noted that in continuum models solvents having the same ε value (such as acetone, ε=20.7, and 1-propanol, ε=20.1, or benzene, ε=2.28, and carbon tetrachloride, ε=2.24) are treated equally. The hydrogen bonding capability of 1-propanol compared with acetone will in reality most likely make a difference, and the solvent dynamics of an almost spherical **CCl_4** will be different from the planar benzene molecule.

II.5.1.1. Cavity and Dispersion/Repulsion Contributions

The big advantage of the simplest spherical or ellipsoidal cavity description is the analytical accessibility of the electrostatic interaction between solute and the dielectric medium. More realistic models employ molecular shaped holes, generated for example by interlocking spheres located on each nucleus. It is generally found that the shape of the hole is important, and that molecular shaped cavities are necessary to be able to obtain good agreement with experimental data. The energy required for cavity creation, and the stabilization due to van der Waals interactions between the solute and solvent is usually assumed to be proportional to the cavity surface area. In this sense the proper description and calculation of the surface boundary between solute and solvent is mandatory. The *van der Waals surface* is generated by multiplying the atomic van der Waals radius by a suitable factor (a typical value is 1.2). The disadvantage of such a surface generated for large molecules (for example proteins) is the presence of small inaccessible regions for solvent molecules. An alternative way to generate the solute-solvent boundary surface is by mapping it by a spherical particle of a given radius (a typical radius of 1.4 A models the water molecule) rolling on the *van der Waals surface*. This is denoted as the *Solvent Accessible Surface* (**SAS**). The corresponding cavity and dispersion energy terms may be taken simply as being proportional to the total **SAS** area (a single proportionality constant):

$$\Delta G_{cavity} + \Delta G_{dispersion} = \gamma SAS + \beta \qquad (28)$$

or parameterized by having a constant ξ specific for each atom type, with the ξ parameters being determined by fitting to experimental solvation data

$$\Delta G_{cavity} + \Delta G_{dispersion} = \sum_i \xi_i S_i \qquad (29)$$

The continuum models where the cavity/dispersion interaction is parameterized by fitting to experimental solvation energies are not recommended to use in combination with first shell explicit treatment of solvent molecules as the parameterization represents a best fit to experimental data without any explicit solvent present.[1b]

II.5.1.2. Electrostatic Solvation Component

The implicit solvation models differ also in the way of treating the electrostatic energy component in the eq. 27.

- *Poisson–Boltzmann method*

The *Poisson* equation describes the connection between the electrostatic potential $\Phi(r)$, the charge distribution $\rho(r)$, and the dielectric constant ε:

$$\nabla\left(\varepsilon(r)\nabla\Phi(r)\right) = -4\pi\rho(r) \qquad (30)$$

when the medium is a continuum dielectric with ε independent of the position, eq. 30 turns into:

$$\nabla^2\Phi(r) = -\frac{4\pi}{\varepsilon}\rho(r) \qquad (31)$$

If the charge distribution is a point charge, the solution of eq. 31 reduces to the *Coulomb* interaction. By taking into account the Boltzmann distribution of ions in the solvent the *Poisson* equation can be modified to the *Poisson–Boltzmann Equation* (PBE).[24]

- *Born/Onsager/Kirkwood methods*

In its simplest approach the reaction field model is a spherical cavity, where only the lowest order electric moment of the molecule is taken into account. The free energy of solvation in this case is equal to the work spent to transfer the net charge q in a cavity of radius a, from vacuum to a medium with a dielectric constant of ε, computed by using *Born* formula:[25]

$$\Delta G_{elec} = -\left(1-\frac{1}{\varepsilon}\right)\frac{q^2}{2a} \tag{32}$$

Although, it is a simple and intuitive model it presents serious disadvantages. Firstly, this model does not distinguish between charge sign, and the solvation energies for positive and negative ions of the same size is the same. This is not the observed behavior in solvents such as water. Furthermore, the reciprocal dependence on the dielectric constant means that the calculated solvent effect is sensitive to the variation of ε in the low dielectric limit, but virtually unaffected by large differences in the high dielectric limit. *Generalized Born model* uses partial charges in eq. 32.

The *Onsager* model[26] refers to the methods that describe the solute as a dipole in a spherical cavity which, for a dipole moment of μ leads to an energy stabilization given by:

$$\Delta G_{elec} = -\frac{\varepsilon-1}{2\varepsilon+1}\frac{\mu^2}{a^3} \tag{33}$$

In contrast, the *Kirkwood* model[27] refers to a general multipole expansion in a spherical cavity, while the *Kirkwood–Westheimer* model[28] arises for an ellipsoidal cavity. Because the spherical or ellipsoidal cavities are realistic only for small and symmetric molecules the use of the *Born/Onsager/Kirkwood* models should therefore only be considered as a rough estimate of the solvent effects, and quantitative results can rarely be obtained.

- Self-consistent reaction field models

When a quantum description of the solute is employed, the calculated electric moments induce charges in the dielectric medium, which in turn acts back on the molecule, causing the wave function to respond and thereby changing the electric moments, etc. The methods that calculate the interaction of the solute with dielectric medium representing the solvent in an iterative procedure are *Self-Consistent Reaction Field* (**SCRF**) models. The interaction of a fixed dipole moment with a polarizable medium given by eq. 33 is not a **SCRF** model, as the dipole moment and stabilization are not calculated in a *self-consistent* way. The dipole moment changes when the back-polarization of the medium is taken into account depending on the molecular polarizability. In the **SCRF** model the full polarization is taking into account, i.e. the initial dipole moment generates a polarization of the medium, which changes the dipole moment, which in turn generates a slightly different polarization, etc. For spherical or ellipsoidal cavities the Poisson equation can be solved analytically, but for molecular shaped surfaces it must be done numerically. This is typically done by reformulating it in terms of a surface integral over surface charges, and solving this numerically by dividing the surface into smaller fractions each having an associated charge $\sigma(r_s)$. The surface charges are related to the electric field $F(r_s)$ (the derivative of the potential Φ) perpendicular to the surface by eq:

$$4\pi\varepsilon\sigma(r_s) = (\varepsilon - 1)F(r_s) \tag{34}$$

Once $\sigma(r_s)$ is determined the associated potential is added as an extra term to the Hamiltonian operator. The potential $\Phi(\sigma(r_s))$ from the surface charge is given by the molecular charge

distribution, but also enters the Hamiltonian and thus influences the molecular wave function, the procedure is therefore iterative.

The *Polarizable Continuum Model* (PCM)[29] employs a van der Waals cavity formed by interlocking atomic van der Waals radii scaled by an empirical factor, the cavity/dispersion contributions are parameterized based on the surface area, and a detailed description of the electrostatic potential is used.

The *Conductor-like Screening Model* (COSMO)[30] also employs molecular shaped cavities, and represents the electrostatic potential by partial atomic charges. In fact it may be considered as a limiting case of the PCM model, where the dielectric constant is set to infinity.

The *Solvation Models*[31] (SM*x*, where $x = 1–5$) are *generalized Born type models* used in connection with the semi-empirical **AM1** and **PM3** methods. The partial atomic charges are calculated from the wavefunction, and the dispersion/cavity terms in eq. 27 are parameterized based on the **SAS**, eq. 29. The different version numbers indicate increasingly sophisticated parameterizations.

The accuracy of the solvation models is difficult to evaluate by default. The fact that all of them were parameterized for specific environmental interactions and specific molecular systems suggests the necessity of their benchmarking before starting a new computational project.

II.6. Optimization Techniques

This last introductory part I dedicate to the technical approaches employed to find the stationary points on the *Potential Energy Surface* (PES). Current progresses in the techniques for exploring PESs are reviewed in ref. 32.

II.6.1. Finding Minima

The simplest approach to reach a minimum of a function is to step one variable at a time until the function has reached a minimum, and then switch to another variable. This requires only the ability to calculate the function value for a given set of variables. The complexity of molecular systems makes this approach impractical. All commonly used methods use the analytical computed gradient of the function with respect to all variables to find a minimum. Some methods went further and use the second derivative matrix, the Hessian, for this purpose. It should be noted that the target function and its derivative(s) are calculated with a finite precision, which depends on the computational implementation. A stationary point can therefore not be located exactly as the gradient can only be reduced to a certain value. In computational chemistry molecular geometry optimization is considered converged when the energy, energy gradient or nuclear displacement between consecutive steps are reduced below the user defined threshold. These criteria may in some cases lead to problems, as a function with a very flat surface in a certain region may satisfy the contiditions without containing a stationary point.

II.6.1.1. Steepest Descent

In the *Steepest Descent* (**SD**) method the first order functional derivative is computed and the function value is lowered by stepping in the opposite direction. A series of such is performed in the negative gradient direction, until the energy starts to increase. Then an

approximate function minimum is determined by interpolation between the calculated points. At this interpolated point, a new gradient is calculated and used for the next search. The disadvantages of this method are: (i) two successive steps are necessarily perpendicular to each other; if there was a gradient component along the previous search direction, the function could be further lowered in this direction, consequently spoiling the previous search; (ii) the **SD** path oscillates around the minimum path, and as the minimum is approached, the rate of convergence slows down; (iii) the *steepest descent* will actually never reach the minimum; it will crawl towards it at an ever decreasing speed. The optimization program should therefore have implemented an algorithm to stop it a point. The advantages are: (i) the algorithm is very simple, and requires only storage of a gradient vector; (ii) the method will always lower the energy value.

II.6.1.2. Conjugate Gradient Methods

The *Conjugate Gradient* (**CG**) methods compensates the lack of information about the previous searches in the **SD** methods by performing each optimization step not only along the current gradient, but along a line that is constructed such that it is "conjugate" to the previous search direction(s). The first step is equivalent to a *steepest descent* step, but subsequent searches are performed along a line formed as a mixture of the current negative gradient and the previous search direction:

$$d_i = -g_i + \beta_i d_{i-1} \tag{35}$$

where d is the direction of search and g is the gradient. Conjugate gradient methods have much better convergence characteristics than the *steepest descent*, but they are again only able to locate minima. They do require slightly more storage than the **SD**, since two (current gradient and previous search direction) vectors must be stored.

II.6.1.3. Newton–Raphson methods

The *Newton–Raphson* (**NR**) algorithm calculates the second order derivative of the function around the current point. The optimization step is produced by moving in the direction of the second order gradient neutralization. Near a minimum, all the Hessian eigenvalues are positive (by definition), and the step direction is opposite to the gradient direction. If, however, one of the Hessian eigenvalues is negative, the step in this direction will be along the gradient component, and thus increase the function value. In this case, the optimization may end up at a stationary point with one negative Hessian eigenvalue, a first-order saddle point. In general, the **NR** method will attempt to converge on the "nearest" stationary point, regardless of whether this is a minimum, saddle point or maximum. The disadvantage of the method is the necessity to calculate the full second derivative matrix, which must be stored and inverted (diagonalized). This is the reason why, when using this method, the initial geometry of computed molecule is very important, and the chemical intuition helps to choose the right geometry, especially in transition structure searches. Since analytic Hessians are rather expensive, especially for larger systems, it is advantageous to avoid computing second derivatives. In the *quasi-Newton* (**QN**) approach, instead of using an analytic Hessian at each step, an approximate Hessian is computed at the start of the calculation (i.e. an empirically estimated Hessian or a Hessian computed at a lower level of theory) and use Hessian updating at the subsequent steps in the optimization. Hessian updating approximates the Hessian using the change in position and gradient from the previous step.

II.6.1.4. GDIIS methods

Newton–Raphson methods can be combined with extrapolation procedures, and the best known of these is the *Geometry Direct Inversion in the Iterative Subspace* (**GDIIS**).[33] In the **GDIIS** method, the **NR** step is not taken from the last geometry but from an interpolated point with a corresponding interpolated gradient based on the previously calculated points on the surface. The method is useful when the geometry is near a sharp minimum, and is

counterproductive in the cases when a flat PES region is scanned, because the **DIIS** procedure will attempt to pull the structure back to the flat energy region, since this is where the gradient is small.

II.6.2. Finding First Order Saddle Points

To locate a minimum on the PES is fairly easy: if everything else fails, the *steepest descent* method is guaranteed to lower the energy value. On the other hand finding the first-order saddle points, transition structures (TS), is much more difficult. The proposed strategies can be divided into two general categories: (i) those based on interpolation between two minima, and (ii) those using only local information. Interpolation methods assume that the reactant and product geometries are known, and that TS is located somewhere in "between". Local methods use only information about the function and its first and possibly also second derivatives at the current point, i.e. they require no knowledge of the reactant and/or product geometries. Local methods require a good starting estimate of the TS in order to converge. Once the TS has been found, the whole reaction path may be located by tracing the *intrinsic reaction coordinate* (**IRC**)[34] which corresponds to a *steepest descent* path from the TS to the reactant and product.

II.6.2.1. Interpolation Methods

The one structure interpolation methods start by selection of one or a few internal "reaction" coordinate that connects reactant and product. The selected coordinate(s) is (are) fixed at certain values, while the remaining variables are optimized, thereby adiabatically mapping the energy as a function of the reaction variable(s). The TS is located as maximum on the obtained energy profile. The success of these methods depends on the ability to choose a good set of reaction variables. The methods work well if only one or two variables change significantly between reactant and product, and the obtained geometry is a good approximation to the TS.

In the *Linear Synchronous Transit* (**LST**) method all coordinates are varied linearly between the reactant and product, and no optimization is performed. The assumption is that all variables change at the same rate along the reaction path, and the TS estimate is simply the highest energy structure along the interpolation line. There are not many cases when LST lead to a reasonable estimate of the TS.

The *Quadratic Synchronous Transit* (**QST**) approximates the reaction path by a parabola instead of a straight line. After the **LST** is performed, the **QST** is generated by minimizing the energy in the directions perpendicular to the **LST** path, and the **QST** path may then be searched for an energy maximum. A more recent variation of **QST**, called *Synchronous Transit-guided Quasi-Newton* (**STQN**), uses a circle arc instead of a parabola for the interpolation, and uses the tangent to the circle for guiding the search towards the TS region. Once the TS region is located, the optimization is switched to a *quasi–Newton*.

Other interpolation techniques use two or more structures to find the TS. The characteristics of interpolation methods are: (i) the methods estimate an intermediate geometry on the reaction path that may or may not be the true transition structure; (ii) the TS found is not necessarily one that connects the two minima used in the interpolation, and an **IRC** calculation must be performed to check the reactants and products connected by the TS found; (iii) the reaction path formed by a sequence of points generated by constrained optimizations may be discontinuous; (iv) the existence of many TSs connecting two minima impose the guidance from the user at the initial search steps (for example by adding various intermediate structures) to find more than one TS and to compare the obtained results; (v) the advantage of the methods is that the constrained optimization can usually be carried out using only the first derivative of the energy, this avoids an explicit, and computationally expensive, calculation of the Hess matrix.

II.6.2.2. Local Methods

In the *Gradient Norm Minimization* methods transition structures are located as zero gradient points on the PES, by minimizing the gradient norm. The obvious disadvantages are:

(i) there are typically many points where the gradient norm has a minimum without being zero; and (ii) any stationary point has a gradient norm of zero, thus all types of saddle points and minima/maxima may be found, not just TSs.

At a point sufficiently close to the TS, the standard *Newton-Raphson* formula will locate the TS rapidly. The Hessian at this point should have exactly one negative eigenvalue, and the eigenvector should be in the correct direction, along the "reaction coordinate". Near such a point the **NR** step maximizes the energy in one direction (along the Hessian TS eigenvector) and minimizes the energy along all other directions. Based on this scheme were developed algorithms to help the program to find the true first order saddle points (e.g. *Partitioned Rational Function Optimization (***P-RFO**),[35] *Quadratic Approximation* (**QA***)*[36] *Trust Radius Image Minimization* (**TRIM**)[37]). All **NR** methods assume that a reasonable guess of the TS geometry is available. Except chemical intuition the interpolation schemes may be useful to find an initial geometry for the TS search, as well.

The local methods are characterized by: (i) the necessity of good initial geometry guess; (ii) the methods use the Hessian, which is quite expensive in terms of computer time for electronic structure methods; (iii) systems with many soft vibrational modes are often problematic, as the resulting low Hessian eigenvalues interfere with the negative curvature along the reaction vector; (iv) the availability of a good starting geometry and Hessian assure a rapid convergence, that often requires only a few tens of gradient calculations.

II.7. References

(1) (a) Koch, W.; Holthausen, M. C. *A Chemists Guide to Density Functional Theory* Wiley, Weinheim, 2001. (b) Jensen, F. *Introduction to Computational Chemistry* Sec. Ed. John Wiley & Sons, 2007.

(2) Hohenberg, P.; Kohn, W. *Phys. Rev.* **1964**, *136*, B864.

(3) Kohn, W.; Sham, L. J. *Phys. Rev.* **1965**, *140*, A1133.

(4) Becke, A. D. *Phys. Rev. A.* **1988**, *38*, 3098.

(5) Lee, C.; Yang, W.; Parr, R. G. *Phys. Rev. B* **1988**, *37*, 785.

(6) Becke, A. D. *J. Chem. Phys.* **1993**, *98*, 5648.

(7) Meijer, E. J.; Sprik, M. *J. Chem. Phys.* **1996**, *105*, 8684.

(8) Rienstra-Kiracofe, J. C.; Tschumper, T. S.; Schaefer III, H. F.; Nandi, S.; Ellison, G. B. *Chem. Rev*. **2002**, *102*, 231.

(9) Gritsenko, O. V.; Ensing, B.; Schipper, P. R. T.; Baerends, E. J. *J. Phys. Chem.* **2000**, *104*, 8558.

(10) Fouqueau, A.; Casida, M. E.; Daku, L. M. L.; Hauser, A.; Neese, F. *J. Chem. Phys.* **2005**, *122*, 044110.

(11) (a) Perdew, J. P.; Ernzerhof, M.; Burke, K. *J. Chem. Phys.* **1996**, *105*, 9982. (b) Adamo, C.; Barone, V. *J. Chem. Phys.* **1999**, *110*, 6158.

(12) Perdew, J. P.; Burke, K.; Wang, Y. *Phys. Rev.* B **1996**, *54*, 16533.

(13) Ketterer, N. A.; Fan, H.; Blackmore K. J.; Yang, X.; Ziller, J. W.; Baik, M.-H.; Heyduk, A. F. *J. Am. Chem. Soc.* **2008**, *130*, 4364.

(14) Perdew, J. P. *Phys. Rev. B* **1986**, *33*, 8822.

(15) Reiher, M.; Salomon, O.; Hess, B. A. *Theor. Chem. Acc.* **2001**, *107*, 48.

(16) Mulliken, R. S. *J. Chem. Phys.* **1955**, *23*, 1833–1840.

(17) *D* is the density matrix; *S* is the overlap matrix.

(18) Chirlian, L. E.; Miller, M. *J. Comput. Chem.* **1987**, *8*, 894.

(19) Bader, R. F. W. *Chem. Rev*. **1991**, *91*, 893.

(20) Hirshfeld, F. L. *Theor. Chim. Acta* **1977**, *44*, 129.

(21) (a) Morokuma, K. *J. Chem. Phys.* **1971**, *55*, 1236. (b) Ziegler, T.; Rauk, A. *Theor. Chim. Acta* **1977**, *46*, 1.

(22) (a) te Velde, G.; Bickelhaupt, F.M.; van Gisbergen S. J. A.; Fonseca Guerra, C.; Baerends, E.J.; Snijders, J.G.; Ziegler, T. *J. Comput. Chem.* **2001,** *22*, 931. (b) ADF2007.01, SCM, Theoretical Chemistry, Vrije Universiteit, Amsterdam, The Netherlands. http://www.scm.com.

(23) (a) Cramer, C. J.; Truhlar, D. G. *Chem. Rev.* **1999**, *99*, 2161. (b) Tomasi, J.; Menucci, B.; Cammi, R. *Chem. Rev.* **2005**, *105*, 2999.

(24) (a) Tannor, D. J.; Marten, B.; Murphy, R. B.; Friesner, R. A.; Sitkoff, D.; Nicholls, A.; Ringnalda, M. N.; Goddard, W. A., III; Honig, B. *J. Am. Chem. Soc.* **1994**, *116*, 11875. (b) Marten, B.; Kim, K.; Cortis, C.; Friesner, R. A.; Murphy, R. B.; Ringnalda, M. N.; Sitkoff, D.; Honig, B. *J. Phys. Chem.* **1996**, *100*, 11775. (c) Edinger, S. R.; Cortis, C.; Shenkin, P. S.; Friesner, R. A. *J. Phys. Chem.* **1997**, *101*, 1190. (d) Friedrichs, M.; Zhou, R. H.; Edinger, S. R.; Friesner, R. A. *J. Phys. Chem. B* **1999**, *103*, 3057.

(25) Born, M. *Z. Physik* **1920**, *1*, 45.

(26) Onsager, L. *J. Am. Chem. Soc.* **1936**, *58*, 1486.

(27) Kirkwood, J. G. *J. Chem. Phys.* **1934**, *2*, 351.

(28) Kirkwood, J. G.; Westheimer, F. H. *J. Chem. Phys.* **1938**, *6*, 506.

(29) (a) Miertus, S.; Scrocco, E.; Tomasi, J. *Chem. Phys.* **1981**, *55*, 117. (b) Tomasi, J.; Persico, M. *Chem. Rev.* **1994**, *94*, 2027.

(30) Klamt, A.; Schuurmann, G. *J. Chem. Soc.; Perkin Trans. 2* **1993**, 799.

(31) (a) Cramer, C. J.; Truhlar, D. G. *J. Am. Chem. Soc.* **1991**, *113*, 8305. (b) Cramer, C. J.; Truhlar, D. G. *Science* **1992**, *256*, 213. (c) Cramer, C. J.; Truhlar, D. G. *J. Comput. Chem.* **1992**, *13*, 1089. (d) Cramer, C. J.; Truhlar, D. G. *J. Comput.-Aid. Mol. Des.* **1992**, *6*, 629.

(32) Hratchian, H. P.; Schliegel, H.B in *Theory and Applications of Computational Chemistry. The first forty years* Ed. Dykstra, C. E.; Frenking, G.; Kim, K. S.; Scuseria, G. E.; ELSEVIER, 2005, p. 195.

(33) Czaszar, P.; Pulay, P *J. Mol. Struct.* **1984**, *114*, 31.

(34) Fukui, K. *Acc. Chem. Res.* **1981**, *14***,** 363.

(35) Banerjee, A.; Adams, N.; Simons, J.; Shepard, R. *J. Phys. Chem.* **1985**, *89***,** 52.

(36) Culot, P.; Dive, G.; Nguyen, V. H.; Ghuysen, J. M. *Theor. Chim. Acta.* **1992,** *82***,** 189.

(37) Helgaker, T. *Chem. Phys. Lett.* **1991**, *182*, 503.

III. Computational Electrochemistry of Ruthenium Anticancer Agents. Unprecedented Benchmarking of Implicit Solvation Methods

III.1. Abstract

Two ruthenium(III) complexes, (HIm)[trans-$RuCl_4$(DMSO)(Im)] (NAMI-A) and (HInd)[trans-$RuCl_4(Ind)_2$] (KP1019); DMSO = dimethyl sulfoxide, Im = imidazole, Ind = indazole, have been tested in phase I clinical trials as potential anticancer drugs. Ru(III) anticancer agents are likely activated in vivo upon reduction to their Ru(II) analogs. Aiming at benchmarking implicit solvation methods in DFT studies of ruthenium pharmaceuticals at the B3LYP level, we have calculated the standard redox potentials (SRPs) of Ru(III/II) pairs that were electrochemically characterized in the literature. 80 SRP values in four solvents were calculated using three implicit solvation methods and five solute cavities of molecular shape. Comparison with experimental data revealed substantial errors in some of the combinations of solvation method and solute cavity. For example, the overall mean unsigned error (MUE) with the PCM/UA0 combination, which is the popular default in Gaussian 03, amounts to 0.23 V (5.4 kcal/mol). The MUE with the CPCM/UAKS combination, which was employed by others for recent computational studies on the hydrolysis of NAMI-A and trans-[$RuCl_4(Im)_2$]–, amounts to 0.30 V (7.0 kcal/mol) for all compounds and to 0.60 V (13.9 kcal/mol) for a subset of compounds of the medicinally relevant type, trans-[$RuCl_4$(L)(L')]–. The SRPs calculated with the PCM or CPCM methods in Gaussian 03 can be significantly improved by a more compact solute cavity constructed with Bondi's set of atomic radii. Earlier findings that CPCM performs better than PCM cannot be confirmed, as the overall MUE amounts to 0.19 V (4.3–4.4 kcal/mol) for both methods in combination with Bondi's set of radii. The Poisson-Boltzmann finite element method (PBF) implemented in Jaguar 7 together with the default cavity performs slightly better, with the overall MUE being 0.16 V (3.7 kcal/mol). Because the redox pairs considered in this study bear molecular charges from +3/+2 to –1/–2 and the prediction of solvation free energies is most challenging for highly

charged species, the present work can serve as a general benchmarking of the implicit solvation methods.

III.2. Objective

Due to the success of cisplatin as an anticancer drug,[1] the search for new metallopharmaceuticals has continued and extended to non-platinum complexes,[2] most notably ruthenium[3] and rhodium.[4] Two Ru(III) complexes, NAMI-A[5] and KP1019,[6] with the common lead structure, trans-$[RuCl_4(L)(L')]^-$ (Figure 1), successfully completed phase I clinical trials.[7] Recent developments of organometallic Ru(II) anticancer complexes are promising as well.[8,9] Ru(III) complexes are believed to be activated in vivo upon reduction to their Ru(II) analogs.[10] A selective reduction in cancer cells occurs likely due to the reducing environment caused by deficiency of molecular oxygen in tumors (hypoxia),[11] as the blood flow to the rapidly growing tumor is insufficient. The standard redox potential (SRP) of a Ru(III) complex is believed to be crucial to its anticancer activity.[12] If it is too low, the complex is not reduced and remains inactive. If it is too high, the complex is reduced too easily and the selectivity to cancer cells is lost.

Figure 1. NAMI-A and KP1019, two Ru(III) anticancer complexes in clinical trials.

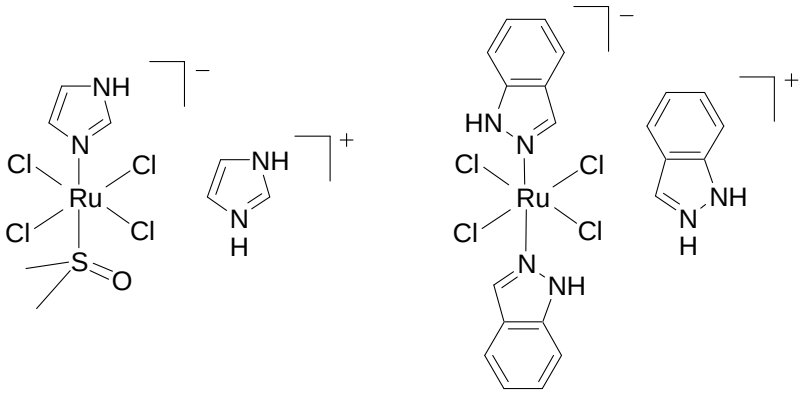

NAMI-A KP1019

The prediction of SRPs can rationalize and accelerate the search for new drugs, because an in silico screening can be performed before relevant compounds are selected, synthesized, and tested in vitro and in vivo. So far, SRPs were often predicted using an empirical increment system[13] derived from experimentally measured SRPs. This empirical approach is successful if strongly related compounds are compared to each other; for example, it does not distinguish between geometric isomers. A more general approach for the prediction of SRPs is based on modern quantum chemical calculations.[14] The objective of the present work is benchmarking various implicit solvation methods[15] and molecule-shaped solute cavities employed for DFT studies at the B3LYP[16,17] level.

Recent computational studies of other groups are highly complementary to the present work. First, benchmarking studies were carried out to assess the performance of different implicit solvation protocols for organic and main group element compounds.[18,19] Second, computation of SRPs of group 8 metal complexes mostly in organic solvents demonstrated that the approach is valid for a wide range of SRPs.[20] Third, the SRP of the aqueous Ru^{3+}aq/Ru^{2+}aq pair was calculated using a variety of quantum chemical methods, ECP's, and basis sets, implicit solvent models, and cavities. The influence of the first and second solvation shells on the SRP of the Ru^{3+}aq/Ru^{2+}aq pair was investigated as well.[21] DFT studies on Ru(III) anticancer agents were recently reported, but validation of the method by predicting their SRPs was not taken into account.[22,23] In the present work, we consider 80 SRPs of 61 ruthenium complexes in four solvents.[24,25] While various types of ruthenium complexes are included, an emphasis is placed on anticancer complexes in aqueous solution, the SRPs of which were measured recently[25,26,27] and fall into a fine biologically relevant window (from −0.4 to +0.8 V vs NHE).[28] We believe that the results of this work provide a general benchmarking of the implicit solvation approaches and will improve the accuracy and credibility of future computational studies of ruthenium pharmaceuticals and other metal complexes.

III.3. Methods

The geometries of the molecules were optimized at the gradient-corrected DFT level using the 3-parameter fit of exchange and correlation functionals of Becke16 (B3LYP), which includes the correlation functional of Lee, Yang, and Parr (LYP),[17] as implemented in Gaussian 03.[29] The Stutgart-Dresden scalar-relativistic energy-consistent small-core effective core potential (ECP) and the corresponding valence-basis sets were used for the Ru (MWB28)[30] and I atoms (MWB46),[31] and the 6-31G(d,p) basis sets were used for the other atoms.[32] This basis-set combination is denoted M. Vibrational frequencies were also calculated at B3LYP/M; all structures reported herein are minima on the potential energy surfaces. Improved total energies were calculated at the B3LYP level using the same ECP and valence-basis set at Ru and I, but totally uncontracted and augmented with two sets of f functions and one set of g functions,[33] together with the 6-311+G(d,p) basis sets at the other atoms, and the 6-311+G(3d) on S, Cl and Br atoms. This basis-set combination is denoted XL. Free energies in vacuo (G^1) were calculated by adding corrections from unscaled zero-point energy (ZPE), thermal energy, work, and entropy evaluated at the B3LYP/M level at 298.15 K, 1 atm to the energies calculated at the B3LYP/XL//M level.

Solvation free energies (ΔG_{solv}) of the structures optimized in vacuo at the B3LYP/M level were calculated using three implicit solvation methods:[15] The Polarizable Continuum model (PCM)[34] in its integral equation formalism (IEF)[35] as implemented in Gaussian 03 and the Conductor-like[36] Polarizable Continuum Model (CPCM)[37] in Gaussian 03,29 and the Poisson-Boltzmann finite element method (PBF)[38] in Jaguar 7.[39] These methods belong to the class of self-consistent reaction field (SCRF) methods. The solute is embedded in a continuum dielectric with a dielectric constant ε representing the solvent.[40] The solute charge distribution polarizes the continuum dielectric, and the potential arising from the solvent polarization in turn modifies the solute Hamiltonian. The calculation of the solute wave function is carried out iteratively until self-consistency. The PCM method describes the solvent reaction potential in terms of apparent surface charges localized on tesserae at the continuum boundary. The CPCM method uses apparent surface charges as well, but describes

the solvent first as a conductor ($\varepsilon = \infty$) and then rescales the charges for a finite value of the dielectric constant. The PBF method uses finite elements for numerical solution of the Poisson-Boltzmann differential equation. The PCM and CPCM calculations were done at the B3LYP/M level, while the PBF calculations were done at the B3LYP/LACVP** level, which includes a scalar-relativistic energy-consistent small-core ECP[41] and basis set at the metal and the 6-31G(d,p) basis sets at the other atoms.

The three solvation methods were used together with solute cavities of molecular shape; the PCM and CPCM methods together with the cavities based on the UA0, UAHF, UAKS, and Bondi radii and the PBF method in Jaguar 7 together with the default set of radii. In the United Atom (UA) topological models,[42] the cavity is obtained from spheres centered on non-hydrogen atoms. The radius of each sphere depends on the atom type, its connectivity and the number of hydrogen atoms attached; typical values are listed in Table 1. The UA0 radii are based on the Universal Force Field (UFF).[43] Variants of these radii were optimized at the Hartree-Fock level (UAHF)[44] and Perdew-Burke-Ernzerhof (PBE)[45] Kohn-Sham DFT level (UAKS).[29] In contrast, Bondi's[46] set of radii consider hydrogen atoms explicitly, and the values depend on atom identity rather than on its connectivities or hybridization. The radii are used in several ways for the construction of cavity in the calculations of the solvation free energies ΔG_{solv}, which is decomposed into solute-cavity-formation[47] (ΔG_{cav}), electrostatic (ΔG_{elst}), and dispersion and repulsion ($\Delta G_{dis\text{-}rep}$) contributions ($\Delta G_{solv} = \Delta G_{elst} + \Delta G_{dis\text{-}rep} + \Delta G_{cav}$). In the PCM and CPCM implementations, the non-electrostatic contributions $\Delta G_{dis\text{-}rep}$ and ΔG_{cav} are calculated using a solvent accessible surface (SAS),[48] whereas ΔG_{elst} is calculated using a similar surface constructed by the radii scaled by a factor[49] and additional spheres to smoothen the surface. In the PBF method, ΔG_{elst} is calculated using an SAS constructed by a set of standard radii including explicit hydrogen atoms (Table 1). An empirical formula depending linearly on the SAS area is employed for the remaining terms, $\Delta G_{dis\text{-}rep} + \Delta G_{cav}$. Our attempts to further refine this set of radii or change the basis sets indicated that the PBF protocol had been reasonably optimized.

Table 1. Radii (Å) used for constructing the solute cavities considered in this work.

	UA0	UAHF	UAKS	Bondi	PBF
H				1.200	1.150
C				1.700	1.900
C[e]	1.925	1.725	1.725		
CH[e]	2.125	1.905	1.905		
CH_2[e]	2.325	2.193	2.193		
CH_3[e]	2.525	1.950	1.950		
N				1.550	1.600
N[a]	1.830	1.551	1.461		
NH[a]	1.930	1.641	1.551		
NH_2[c]	2.030	1.680	1.680		
NH_3[b]	2.130	1.770	1.770		
O				1.520	1.600
O[a]	1.750	1.569	1.479		
OH[d]	1.780	1.590	1.590		
OH_2[b]	1.950	1.569	1.569		
S	2.017[a]	1.959[a]	1.959[a]	1.800	1.900
Cl	1.973[a]	1.959[a]	1.959[a]	1.750	1.974
Br	2.094[c]	2.080[c]	2.080[c]	1.850	2.095
Ru	1.482	1.482	1.482	1.482	1.481
I	2.250[f]	2.350[f]	2.350[f]	1.980	2.250

a In *trans*-$[RuCl_4(DMSO)(Im)]^-$. b In *cis*-$[Ru(NH_3)_4(OH_2)_2]^{3+}$. c In *trans*-$[Ru(NH_3)_4Br(isn)]^{2}$+ d In $[Ru(NH_3)_5(OH)]^{2+}$ e In *mer,trans*-$[RuCl_3(Et_2S)(Ind)_2]$. f In *cis*-$[Ru(NH_3)_4I(py)]^{2+}$.

Standard redox potentials (SRPs) were calculated on the basis of the thermodynamic cycle shown in Figure 2,[14,50] which is similar to that proposed for the prediction of acidity constants.51 The SRP is related to the reaction free energy in solution (ΔG^{ε}):

$$SRP = (\Delta G^{\varepsilon}/zF) - \Delta SRP_{NHE}$$

$$\text{with } \Delta G^{\varepsilon} = - \Delta G_{solv}(Ox) + \Delta G^{1} + \Delta G_{solv}(Red)$$

according to Figure 2. ΔG^1 is the reaction free energy in vacuo, $\Delta G_{solv}(Ox)$ and $\Delta G_{solv}(Red)$ are the solvation free energies in of the oxidized and reduced form, F = 96,485 C/mol = 23.061 kcal/(Vmol) is the Faraday constant, and z = 1 for one-electron reductions. The SRPs are shifted by ΔSRP_{NHE} = 4.28 V to align the results to the scale of the Normal Hydrogen Electrode (NHE).[52]

Figure 2. Thermodynamic cycle for calculating redox potentials.

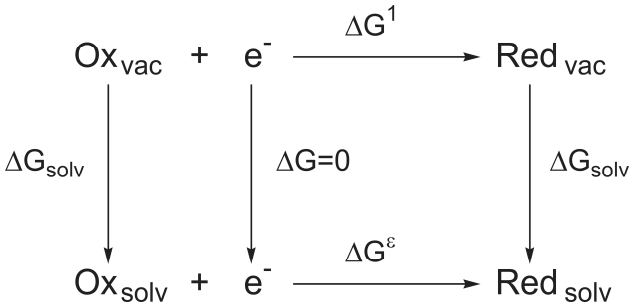

III.4. Results and Discussion

We start with the default solvation protocol in Gaussian 03, which consists of the Polarizable Continuum Model (PCM)[34] together with the default definition of the solute cavity on the basis of the united atom topological model UA0.[42] This approach is denoted as Protocol I. Figure 3a shows the calculated (PCM/UA0) vs experimental SRPs. The results are displayed as follows: (i) The solvent (ACN, DMF, DMSO, water) is indicated by the color of symbol. (ii) The molecular charge of the redox pairs ranging from +3/+2 to –1/–2 is indicated by the shape of symbol. (iii) The medicinal relevance is indicated by the filling of symbol, as the aqueous SRPs for the complexes of the type *trans*-$[RuCl_4(L)(L')]^-$ are displayed as filled symbols. The two drug candidates in the clinics, KP1019 and NAMI-A, belong to this category (Figure 1). To analyze the results in a quantitative manner, mean unsigned errors (MUE) are listed in Table 2, sorted by solvent, molecular charge, and medicinal relevance. The overall MUE of Protocol I for the complete set of data (all compounds in all solvents) is 0.23 V (5.4 kcal/mol). Similar MUE values are obtained for subsets of complexes in water and medicinally relevant complexes, 0.26 V (6.0 kcal/mol) and 0.29 V (6.8 kcal/mol), respectively.

Figure 3. Calculated vs experimental SRPs. (a) Protocol I, PCM/UA0, (b) Protocol II, PCM/UAHF, (c) Protocol IV, PCM/Bondi, (d) Protocol VII, PB. The data are sorted by solvent (color of symbol) and charge (shape of symbol). Aqueous SRPs of the medicinally relevant complexes with the lead structure, *trans*-$[RuCl_4(L)(L')]^-$, are displayed as filled symbols.

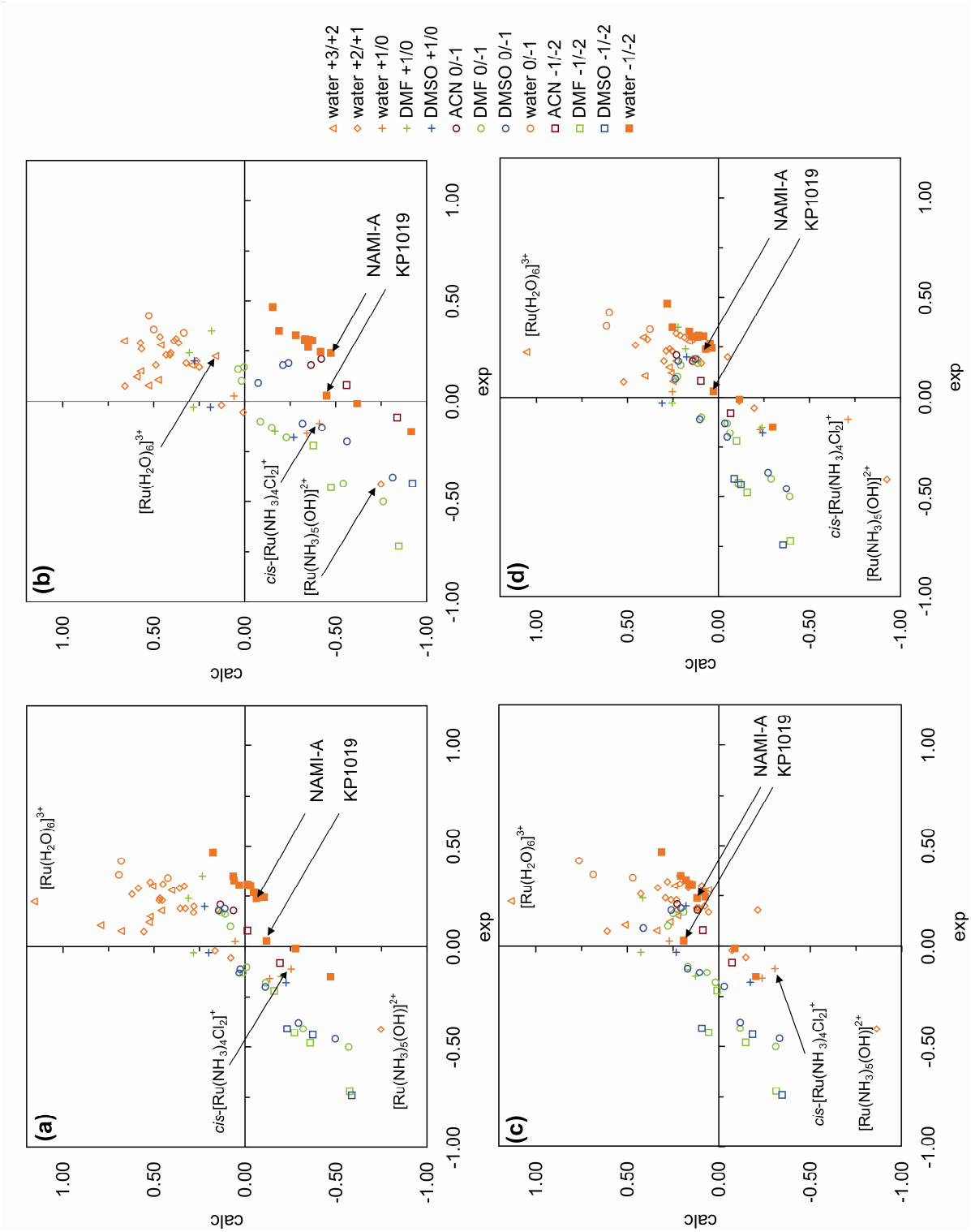

Protocol II combines the PCM method with the UAHF cavity, as implemented in Gaussian 03. This approach has been frequently used, as it is recommended for the prediction of solvation free energies by comparing solution and gas phase free energies.29 Figure 3b displays the calc. vs exp. SRPs and Table 2 includes the MUEs. The calculations reveal that this protocol performs worse than protocol I: The MUE for the complete set of data (all compounds in all four solvents) is 0.32 V (7.4 kcal/mol). Considering the molecular charges of the redox couples, the most unsatisfactory results are obtained for the highly charged complexes, as the +3/+2 pairs and −1/−2 redox pairs have MUEs of 0.30 V (7.0 kcal/mol) and 0.59 V (13.5 kcal/mol), respectively. A rather high MUE of 0.63 V (14.6 kcal/mol) is obtained for the medicinally relevant subset. Protocol III uses the same PCM method together with the UAKS radii, as implemented in Gaussian 03; this definition of the solute cavity is recommended for DFT calculations.[29] The calculations show only a very minor improvement in comparison with the UAHF approach, as the MUEs are similar to those of Protocol II (Table 2).

Table 2. Mean unsigned errors (MUE) in the calculation of SRPs using Protocols I-VII. All values in Volt (V).

		I	II	III	IV	V	VI	VII
		PCM	PCM	PCM	PCM	CPCM	CPCM	PBF
compounds	number	UA0	UAHF	UAKS	Bondi	UAKS	Bondi	
all	80	0.23	0.32	0.31	0.19	0.30	0.19	0.16
solvent								
ACN	4	0.10	0.64	0.65	0.02	0.64	0.03	0.02
DMF	16	0.10	0.16	0.16	0.25	0.15	0.26	0.16
DMSO	14	0.34	0.38	0.36	0.21	0.35	0.22	0.17
water	46	0.26	0.33	0.31	0.18	0.31	0.17	0.17
charge								
+3/+2	8	0.45	0.30	0.27	0.27	0.27	0.27	0.23
+2/+1	18	0.19	0.18	0.16	0.15	0.16	0.15	0.13
+1/0	10	0.10	0.15	0.13	0.19	0.13	0.19	0.19
0/-1	21	0.26	0.24	0.24	0.18	0.23	0.19	0.11
-1/-2	23	0.23	0.59	0.57	0.20	0.57	0.20	0.19
Lead[a]	14	0.29	0.63	0.61	0.14	0.60	0.14	0.16

a Aqueous SRPs of the compounds with the lead structure *trans*-$[RuCl_4(L)(L')]^-$

To analyze the performance of the methods further and to identify systematic errors, we have also calculated the mean signed errors (MSE, see Table 3). For protocols I-III, the MSEs are positive for cationic redox pairs charge (+3/+2), but they are negative for anionic redox pairs (−1/−2). The relatively large errors for these highly charged complexes remained undiscovered in the past, because typical benchmarking studies uses pKa values and SRPs involving only species that have a molecular charge between +1 and −1. Because SRPs are derived from the differential free energies of the reduced forms (Figure 2), the MSEs translate to an underestimation of solvation free energies that is strongest for the species bearing the highest (positive or negative) molecular charge q. Bearing the simple Born model[53] for ions in spherical cavities (ΔGsolv proportional $-q^2r^{-1}$) in mind, one would expect that a more compact molecular cavity improves the results, because of the reciprocal dependence of the solvation free energy ΔG_{solv} on the sphere radius r. While our attempts to manually adjust the cavity within the united atom approach did not improve the results, we have also considered the PCM model combined with a more compact cavity based on Bondi radii (Table 1); this combination is denoted as Protocol IV. SRPs are plotted in Figure 3c and the MUE and MSE are listed in Table 2 and 3. The calculations reveal that Protocol IV significantly improves the agreement with the experimental values. The overall MUE for the complete set of data (all compounds in all solvents) is 0.19 V (4.3 kcal/mol). Remarkably, the MUEs are now relatively similar for all charges of redox pairs from +3/+2 to −1/−2 (Table 2). The MSEs indicate that the systematic errors have been largely eliminated (Table 3). The performance of this protocol is convincing, as is indicated by MUEs of 0.18 V (4.0 kcal/mol) for the complexes in aqueous solution and 0.14 V (3.3 kcal/mol) for the medicinally relevant set (Table 2).

Table 3. Mean signed errors (MSE) in the calculation of SRPs using protocols I-VII. All values in Volt (V).

compounds	number	I PCM UA0	II PCM UAHF	III PCM UAKS	IV PCM Bondi	V CPCM UAKS	VI CPCM Bondi	VII PBF
all	80	0.01	-0.17	-0.17	0.08	-0.17	0.08	0.03
solvent								
ACN	4	-0.10	-0.64	-0.65	-0.01	-0.64	0.00	0.00
DMF	16	0.06	-0.11	-0.11	0.23	-0.10	0.24	0.11
DMSO	14	-0.18	-0.33	-0.33	0.21	-0.33	0.22	0.15
water	46	0.06	-0.09	-0.10	-0.01	-0.10	-0.01	-0.03
charge								
+3/+2	8	0.45	0.29	0.25	0.20	0.25	0.20	0.20
+2/+1	18	0.14	0.14	0.12	-0.07	0.11	-0.07	-0.05
+1/0	10	0.03	-0.01	-0.02	0.10	-0.02	0.10	-0.02
0/-1	21	-0.11	-0.22	-0.20	0.18	-0.19	0.19	0.09
-1/-2	23	-0.15	-0.59	-0.57	0.04	-0.57	0.05	-0.01
Lead[a]	14	-0.29	-0.63	-0.61	-0.12	-0.60	-0.11	-0.16

a Aqueous SRPs of the compounds with the lead structure *trans*-$[RuCl_4(L)(L')]^-$

On the basis of pKa predictions for neutral and monocationic organic molecules, it was convincingly shown18 that the conductor-like screening approach (CPCM) performs better than the polarizable continuum model (PCM). Without further benchmarking calculations for metal complexes, the CPCM method together with the UAKS cavity was recently employed for a computational studies on the hydrolysis of NAMI-A and *trans*-$[RuCl_4(Im)_2]^-$.[23] Hence, we have included the CPCM/UAKS approach in our benchmarking (Protocol V). The calculations reveal that Protocol V performs as disappointingly as does Protocol II (PCM/UAKS). For example, the MUE for the set of medicinally relevant compounds of the *trans*-$[RuCl_4(L)(L')]^-$ type amounts to 0.60 V (13.9 kcal/mol). To compare the PCM and CPCM performance further, we have also considered the CPCM method and the Bondi radii (Protocol VI); these results are very similar to those of Protocol III (PCM/Bondi). In summary, there is a striking agreement between the PCM and CPCM approaches, which is consistent with a benchmarking study of the SRPs of nitrogen oxides.19 An appropriate definition of the solute cavity appears to be at least as important as the choice of the solvent model.

Finally, we have employed a finite element method for the numerical solution of the Poisson-Boltzmann equation (PBF) as implemented in Jaguar 7, together with the default set of radii for setting up the solute cavity (Protocol VII). This approach has been used in our series Quantum chemical studies of metals in medicine[54] and in other studies[55] of medicinally relevant metal complexes. Figure 3d visualizes the SRPs and Table 2 and 3 list the errors. The overall MUE for the complete set of data (all compounds in all solvents) is 0.16 V (3.7 kcal/mol), which is the best value among all solvation protocols considered in this work. The approach performs well for all four solvents and all molecular charges of redox pairs from +3/+2 to −1/−2. The MUE is 0.17 V (4.0 kcal/mol) for the complexes in water and 0.16 V (3.7 kcal/mol) for the medicinally relevant set. The performance of Protocol VII (PB) is very similar to the PCM and CPCM methods with the Bondi radii.

Despite the overall success of the PBF method, we have identified a few cases where this approach predicts unsatisfactory results, as compared to the experimental values. The aqueous SRP of the hydrated Ru ion redox couple, $[Ru(OH_2)_6]^{3+/2+}$ is computationally overestimated by +0.83 V (Figure 3d).[56] In contrast, the SRP of $[Ru(NH_3)_5(OH)]^{2+/+}$ and *cis*-$[Ru(NH_3)_4Cl_2]^{+/0}$ are computationally underestimated by -0.52 V and -0.60 V, respectively (Figure 3d). The other protocols perform better for the latter compound (see Figure 3 and Table S3), but all protocols using the Bondi and UA0 cavities overestimate the SRP of $[Ru(OH_2)_6]^{3+/2+}$ by +0.91-0.93 V. The fact that the aqueous Ru(III/II) redox couple poses a challenge to computational chemistry was also pointed out in a recent article that focuses entirely on this redox pair.[21] These authors make extensive use of their computationally efficient solvation model termed SM6[57] and predict at B3LYP a SRP that is +0.77 V higher than the experimental value. As the $[Ru(OH_2)_6]^{3+}$ is highly charged and contains six aqua ligands, the predicted SRP depends strongly on the radius employed for the oxygen and hydrogen atoms. We find that shrinking the H atom radius or H and O atom radii in the PBF method to 1.02 Å or 1.02 and 1.52 Å, respectively, reduces the error in the calculated SRP to +0.46 V or +0.39 V, but increases the errors for the other two problem cases. The surface charge density of $[Ru(OH_2)_6]^{3+}$ can be lowered by the second hydration shell, which was represented in the recent study[21] by a symmetric arrangement of 12 additional water molecules. Remarkably, this approach led at B3LYP to a SRP that is –0.23 V lower than the experimental value.

Finally, we would like to emphasize that there is some arbitrariness in the prediction of absolute SRPs because of the choice of ΔSRP_{NHE}. ΔSRP_{NHE} may be calculated using a thermodynamic cycle for the reaction, $1/2\ H_2 \rightarrow H^+ + e^-$, analogue to that in Figure 2. ΔSRP_{NHE} is the sum of the gas phase free energy ΔG^1_{NHE} of this reaction and the solvation free energy of H^+. The authors of ref. 52 chose ΔG^1_{NHE} = 362.59 kcal/mol[58] obtained from thermochemical data and $\Delta G_{solv}(H^+)$ = –263.98 kcal/mol[59] obtained from extrapolating thermochemical data for ion-pair clusters with up to 6 water molecules to bulk solvent to arrive at ΔSRP_{NHE} = 4.28 V,[52] which is the same value employed for the present work. Considering ΔG^1_{NHE} = 362.59 kcal/mol[58] together with $\Delta G_{solv}(H^+)$ = –264.61 kcal/mol[60] obtained from a thermodynamic cycle of acetic acid dissociation results in the alternative value of ΔSRP_{NHE} = 4.25 V, thus shifting the predicted SRPs of our Ru(III/II) redox couples by +0.03 V. Considering ΔG^1_{NHE} = 362.5 kcal/mol[61] together with $\Delta G_{solv}(H^+)$ = –259.5 kcal/mol[62] obtained from electrochemical data leads to the popular value of ΔSRP_{NHE} = 4.44 V.[63] Considering ΔG^1_{NHE} = 364.27 kcal/mol, calculated at the B3LYP/XL//M level, and the same $\Delta G_{solv}(H^+)$ = –263.98 kcal/mol[59] results in ΔSRP_{NHE} = 4.35 V. By estimating the absolute half cell potential using the method[64] which shifts the surface dipole layer problem away from the electrolyte-air interface and focuses it on the solid the widely used value of 4.43 V was obtained. Because of this arbitrariness in the choice of ΔG^1_{NHE} and $\Delta G_{solv}(H^+)$, one may simply treat ΔSRP_{NHE} as a free parameter to be obtained in a fitting procedure. Given that the mean signed error (MSE) of the PBF method (Protocol VII) amounts to only 0.03 V (Table 3), however, we believe that ΔSRP_{NHE} = 4.28 V suggested in ref. 52 is an excellent choice.

In conclusion, we recommend the Poisson-Boltzmann finite element solver (PBF) implemented in Jaguar (Protocol VII) and the PCM or CPCM method together with the Bondi radii implemented in Gaussian (Protocols IV and VI) for future DFT/CDM studies. However, caution is advised if the solute is highly charged and contains many hydrogen bond donors in the first shell. Our recommendation is not limited to ruthenium complexes, as the metal center in the compounds considered in this work is surrounded by an octahedral ligand environment and not directly exposed to solvent. In addition, the wide range of the molecular charges of the redox pairs from +3/+2 to −1/−2 has made the calculation of solvation free energies very challenging. Consideration of highly charged species has led to the

identification of systematic errors in the solvation free energies that were difficult to find in previous benchmarking studies involving compounds with molecular charges from +1 to –1. Hence, the results of the present work may serve as an unprecedented benchmarking of implicit solvation methods for density functional studies of the reactions of metal complexes involved in catalysis, biology, and medicine.

III.5. Acknowledgment

We thank the Gaussian and Jaguar developers for helpful discussions, the Austrian Science Foundation (FWF) and the Swiss National Science Foundation (SNF) for financial support, and the Swiss National Computing Center and the Schroedinger Computing Center at the University of Vienna for computing time.

III.6. Supporting Information

Table S1. Mean unsigned errors (MUE) in the calculation of SRPs using protocols I-VII. All values in kcal/mol.

compounds	number	I PCM UA0	II PCM UAHF	III PCM UAKS	IV PCM Bondi	V CPCM UAKS	VI CPCM Bondi	VII PBF
all	80	5.4	7.4	7.1	4.3	7.0	4.4	3.7
solvent								
ACN	4	2.3	14.8	14.9	0.6	14.8	0.7	0.5
DMF	16	2.3	3.7	3.6	5.7	3.5	6.0	3.6
DMSO	14	7.8	8.7	8.2	4.8	8.1	5.0	3.9
water	46	6.0	7.6	7.2	4.0	7.1	4.0	4.0
charge								
+3/+2	8	10.4	7.0	6.2	6.2	6.1	6.1	5.3
+2/+1	18	4.3	4.0	3.7	3.4	3.6	3.4	3.1
+1/0	10	2.4	3.4	3.0	4.3	3.0	4.3	4.3
0/-1	21	6.0	5.6	5.4	4.2	5.3	4.4	2.5
-1/-2	23	5.2	13.5	13.2	4.6	13.0	4.6	4.4
Lead[a]	14	6.8	14.6	14.0	3.3	13.9	3.1	3.7

[a] Aqueous SRPs of the compounds with the lead structure trans-$[RuCl_4(L)(L')]^-$

Table S2. Mean signed errors (MSE) in the calculation of SRPs using protocols I-VII. All values in kcal/mol.

compounds	number	I PCM UA0	II PCM UAHF	III PCM UAKS	IV PCM Bondi	V CPCM UAKS	VI CPCM Bondi	VII PBF
all	80	0.2	-3.8	-3.9	1.7	-3.8	1.9	0.7
solvent								
ACN	4	-2.3	-14.8	-14.9	-0.2	-14.8	0.1	0.1
DMF	16	1.3	-2.6	-2.5	5.3	-2.4	5.6	2.6
DMSO	14	-4.1	-7.7	-7.7	4.8	-7.5	5.0	3.4
water	46	1.3	-2.2	-2.2	-0.3	-2.2	-0.2	-0.8
charge								
+3/+2	8	10.4	6.7	5.8	4.6	5.7	4.5	4.7
+2/+1	18	3.2	3.2	2.7	-1.6	2.6	-1.6	-1.1
+1/0	10	0.8	-0.1	-0.5	2.3	-0.5	2.4	-0.4
0/-1	21	-2.7	-5.1	-4.6	4.0	-4.5	4.3	2.2
-1/-2	23	-3.5	-13.5	-13.2	1.0	-13.0	1.2	-0.1
Lead[a]	14	-6.8	-14.6	-14.0	-2.7	-13.9	-2.6	-3.7

[a] Aqueous SRPs of the compounds with the lead structure trans-$[RuCl_4(L)(L')]^-$

Table S3. Calculated vs experimental SRPs. Protocol I: PCM/UA0; II: PCM/UAHF; III: PCM/UAKS; IV: PCM/Bondi; V: CPCM/UAKS; VI: CPCM/Bondi; VII: PBF. The results are sorted by molecular charge, solvent, and chemical similarity.

Complex[a] (oxidized form)	solvent	I PCM UA0	II PCM UAHF	III PCM UAKS	IV PCM Bondi	V CPCM UAKS	VI CPCM Bondi	VII PBF	exp	Ref
$[Ru(Im)_6]^{3+}$	*water*	0.51	0.66	0.56	0.24	0.56	0.24	0.42	0.30	24g
$[Ru(MeIm)_6]^{3+}$	*water*	0.40	0.46	0.36	0.06	0.36	0.06	0.16	0.28	24g
$[Ru(en)_3]^{3+}$	*water*	0.46	0.29	0.27	0.23	0.27	0.23	0.23	0.18	24b
$[Ru(OH_2)_6]^{3+}$	*water*	1.16	0.16	0.16	1.14	0.15	1.14	1.06	0.23	56
$[Ru(NH_3)_5(OH_2)]^{3+}$	*water*	0.68	0.53	0.53	0.34	0.53	0.34	0.25	0.08	24b
cis-$[Ru(NH_3)_4(Im)_2]^{3+}$	*water*	0.52	0.57	0.56	0.23	0.56	0.22	0.27	0.15	24g
trans-$[Ru(NH_3)_4(Im)_2]^{3+}$	*water*	0.53	0.59	0.54	0.27	0.54	0.27	0.26	0.12	24g
cis-$[Ru(NH_3)_4(OH_2)_2]^{3+}$	*water*	0.79	0.48	0.47	0.51	0.46	0.51	0.40	0.11	24b
$[RuCl(OH_2)_5]^{2+}$	*water*	0.56	0.66	0.62	0.61	0.62	0.61	0.52	0.08	24b
$[Ru(NH_3)_5Br]^{2+}$	*water*	0.16	0.13	0.13	-0.07	0.13	-0.07	-0.11	-0.02	24a
$[Ru(NH_3)_5Cl]^{2+}$	*water*	0.08	0.01	0.01	-0.15	0.01	-0.15	-0.20	-0.06	24b
$[Ru(NH_3)_5(OH)]^{2+}$	*water*	-0.75	-0.75	-0.75	-0.86	-0.75	-0.86	-0.93	-0.41	24b
cis-$[Ru(NH_3)_4Cl(py)]^{2+}$	*water*	0.28	0.25	0.25	0.06	0.25	0.06	0.09	0.17	24a
trans-$[Ru(NH_3)_4Cl(py)]^{2+}$	*water*	0.28	0.26	0.26	0.08	0.26	0.08	-0.05	0.20	24a
cis-$[Ru(NH_3)_4Cl(isn)]^{2+}$	*water*	0.47	0.41	0.45	0.26	0.42	0.26	0.25	0.23	24a
trans-$[Ru(NH_3)_4Cl(isn)]^{2+}$	*water*	0.36	0.36	0.34	0.17	0.34	0.17	0.14	0.29	24a
cis-$[Ru(NH_3)_4(CH_3CN)Cl]^{2+}$	*water*	0.45	0.38	0.36	0.21	0.36	0.21	0.21	0.31	24a
trans-$[Ru(NH_3)_4(CH_3CN)Cl]^{2+}$	*water*	0.52	0.47	0.47	0.28	0.46	0.28	0.23	0.32	24a
cis-$[Ru(NH_3)_4Br(py)]^{2+}$	*water*	0.36	0.32	0.32	0.11	0.32	0.11	0.14	0.19	24a
trans-$[Ru(NH_3)_4Br(py)]^{2+}$	*water*	0.33	0.32	0.32	0.12	0.32	0.12	0.11	0.19	24a
cis-$[Ru(NH_3)_4Br(isn)]^{2+}$	*water*	0.47	0.41	0.46	0.29	0.46	0.29	0.27	0.24	24a
trans-$[Ru(NH_3)_4Br(isn)]^{2+}$	*water*	0.33	0.39	0.32	0.09	0.32	0.09	0.19	0.30	24a
cis-$[Ru(NH_3)_4I(py)]^{2+}$	*water*	0.41	0.39	0.40	0.19	0.39	0.19	0.25	0.23	24a
trans-$[Ru(NH_3)_4I(py)]^{2+}$	*water*	0.10	0.45	0.13	-0.25	0.13	-0.26	0.26	0.18	24a
cis-$[Ru(NH_3)_4I(isn)]^{2+}$	*water*	0.53	0.48	0.49	0.34	0.49	0.34	0.37	0.26	24a
trans-$[Ru(NH_3)_4I(isn)]^{2+}$	*water*	0.55	0.54	0.53	0.30	0.52	0.30	0.35	0.29	24a
cis-$[Ru(NH_3)_4Cl_2]^{+}$	*water*	-0.25	-0.41	-0.41	-0.31	-0.41	-0.30	-0.71	-0.11	24b
trans-$[Ru(NH_3)_4Cl_2]^{+}$	*water*	-0.14	-0.34	-0.34	-0.24	-0.34	-0.23	-0.23	-0.16	24a
cis-$[RuCl_2(OH_2)_4]^{+}$	*water*	0.05	0.06	0.06	0.27	0.06	0.27	0.25	0.03	24b
trans-$[RuCl_2(Im)_4]^{+}$	*DMF*	-0.20	-0.17	-0.19	0.13	-0.19	0.14	-0.24	-0.15	25c
trans-$[Ru(bim)_4Cl_2]^{+}$	*DMF*	0.28	0.28	0.24	0.43	0.25	0.44	0.25	-0.03	25c
trans-$[RuCl_2(trz)_4]^{+}$	*DMF*	0.31	0.30	0.31	0.42	0.31	0.42	0.18	0.24	25c
trans-$[RuCl_2(pz)_4]^{+}$	*DMF*	0.23	0.18	0.21	0.22	0.21	0.22	0.22	0.35	25c
trans-$[RuCl_2(Im)_4]^{+}$	*DMSO*	-0.23	-0.27	-0.29	-0.17	-0.29	-0.17	-0.24	-0.18	25c
trans-$[Ru(bim)_4Cl_2]^{+}$	*DMSO*	0.20	0.19	0.10	0.23	0.10	0.24	0.31	-0.03	25c
trans-$[RuCl_2(trz)_4]^{+}$	*DMSO*	0.22	0.28	0.23	0.18	0.23	0.18	0.17	0.20	25c
Ru (bpy)(4,4'-bpy)Cl_3	*ACN*	0.06	-0.36	-0.33	0.12	-0.32	0.13	0.14	0.18	24i
Ru (bpy)$(CH_3CN)Cl_3$	*ACN*	0.14	-0.42	-0.42	0.23	-0.41	0.24	0.23	0.21	24i
mer,trans-$RuCl_3(Me_2S)(Ind)_2$	*DMF*	0.11	0.04	0.11	0.25	0.06	0.24	0.21	0.16	25b

mer,*trans*-$RuCl_3(Et_2S)(Ind)_2$	*DMF*	0.13	0.00	0.02	0.19	0.08	0.23	0.11	0.17	25b
mer-Ru $(buim)_3Cl_3$	*DMF*	-0.57	-0.76	-0.80	-0.31	-0.79	-0.29	-0.39	-0.50	25c
mer -$Ru(bim)_3Cl_3$	*DMF*	-0.32	-0.54	-0.50	-0.12	-0.49	-0.09	-0.29	-0.41	25c
mer -$RuCl_3(Metrz)_3$	*DMF*	-0.11	-0.23	-0.22	0.02	-0.22	0.03	-0.06	-0.18	25c
mer-$RuCl_3(Mepz)_3$	*DMF*	0.01	-0.15	-0.13	0.06	-0.13	0.08	-0.05	-0.13	25c
mer-$RuCl_3(pz)_3$	*DMF*	-0.01	-0.09	-0.06	0.17	-0.06	0.18	0.09	-0.10	25c
mer-$RuCl_3(Ind)_3$	*DMF*	0.08	0.02	0.03	0.28	0.03	0.29	0.22	0.10	25c
mer,*trans*-$RuCl_3(Me_2S)(Ind)_2$	*DMSO*	0.15	-0.21	-0.20	0.26	-0.20	0.27	0.22	0.18	25b
mer,*trans*-$RuCl_3(Et_2S)(Ind)_2$	*DMSO*	0.11	-0.24	-0.24	0.21	-0.23	0.22	0.13	0.19	25b
mer-Ru $(buim)_3Cl_3$	*DMSO*	-0.50	-1.03	-1.04	-0.33	-1.03	-0.32	-0.37	-0.46	25c
mer-$Ru(bim)_3Cl_3$	*DMSO*	-0.29	-0.81	-0.76	-0.12	-0.75	-0.10	-0.27	-0.38	25c
mer-$RuCl_3(Metrz)_3$	*DMSO*	-0.11	-0.56	-0.55	-0.03	-0.55	-0.02	-0.05	-0.20	25c
mer-$RuCl_3(Mepz)_3$	*DMSO*	0.03	-0.42	-0.39	0.10	-0.39	0.11	-0.03	-0.13	25c
mer-$RuCl_3(pz)_3$	*DMSO*	0.03	-0.32	-0.30	0.17	-0.29	0.18	0.10	-0.11	25c
mer-$RuCl_3(Ind)_3$	*DMSO*	-3.33	-0.07	-0.08	0.41	-0.07	0.42	0.24	0.09	25c
mer-$RuCl_3(DMSO)_2(OH_2)$	*water*	0.68	0.53	0.56	0.76	0.56	0.77	0.60	0.43	24d
mer-$Ru(NH_3)Cl_3(DMSO)_2$	*water*	0.69	0.50	0.52	0.69	0.52	0.69	0.62	0.36	24d
mer -$RuCl_3(DMSO)_2(Im)$	*water*	0.42	0.33	0.36	0.47	0.37	0.48	0.38	0.34	24d
$[Ru(bpy)Cl_4]^-$	*ACN*	-0.19	-0.84	-0.90	-0.07	-0.89	-0.06	-0.07	-0.08	24i
$[Ru(dcbpy)Cl_4]^-$	*ACN*	-0.01	-0.56	-0.55	0.09	-0.54	0.09	0.10	0.08	24i
trans-$[RuCl_4(DMSO)(Im)]^-$	*DMF*	-0.16	-0.38	-0.38	0.01	-0.37	0.03	-0.10	-0.22	25a
trans-$[RuCl_4(Im)_2]^-$	*DMF*	-0.58	-0.85	-0.90	-0.31	-0.88	-0.29	-0.40	-0.72	25c
trans-$[RuCl_4(trz)_2]^-$	*DMF*	-0.36	-1.33	-1.34	-0.15	-1.33	-0.13	-0.16	-0.48	25c
trans-$[RuCl_4(Ind)_2]^-$	*DMF*	-0.27	-0.48	-0.47	0.06	-0.46	0.07	-0.11	-0.43	25c
trans-$[RuCl_4(Im)_2]^-$	*DMSO*	-0.59	-1.46	-1.46	-0.35	-1.45	-0.33	-0.35	-0.74	25c
trans-$[RuCl_4(trz)_2]^-$	*DMSO*	-0.37	-1.22	-1.20	-0.18	-1.20	-0.18	-0.12	-0.44	25c
trans-$[RuCl_4(Ind)_2]^-$	*DMSO*	-0.23	-0.92	-0.90	0.09	-0.90	0.10	-0.09	-0.41	25c
trans-$[RuCl_4(Im)_2]^-$	*water*	-0.47	-0.92	-0.83	-0.20	-0.83	-0.19	-0.30	-0.15	24f
trans-$[RuCl_4(tz)_2]^-$	*water*	-0.28	-0.62	-0.63	-0.09	-0.63	-0.08	-0.12	-0.01	24h
trans-$[RuCl_4(Ind)_2]^-$	*water*	-0.12	-0.45	-0.45	0.19	-0.44	0.20	0.03	0.03	25a
trans-$[RuCl_4(DMSO)_2]^-$	*water*	0.18	-0.15	-0.11	0.31	-0.11	0.32	0.28	0.47	24c
trans-$[RuCl_4(DMSO)(OH_2)]^-$	*water*	0.06	-0.19	-0.17	0.21	-0.17	0.21	0.25	0.35	24c
trans-$[Ru(NH_3)Cl_4(DMSO)]^-$	*water*	-0.05	-0.35	-0.33	0.08	-0.33	0.09	0.05	0.27	24d
trans-$[RuCl_4(DMSO)(Im)]^-$	*water*	-0.06	-0.47	-0.38	0.12	-0.37	0.13	0.07	0.24	24d
trans-$[RuCl_4(DMSO)(MeIm)]^-$	*water*	-0.11	-0.42	-0.40	0.07	-0.39	0.08	0.04	0.25	24d
trans-$[RuCl_4(DMSO)(pz)]^-$	*water*	0.03	-0.33	-0.31	0.16	-0.31	0.17	0.11	0.31	24d
trans-$[RuCl_4(DMSO)(Ind)]^-$	*water*	0.06	-0.28	-0.27	0.18	-0.27	0.19	0.16	0.33	24d
trans-$[RuCl_4(DMSO)(py)]^-$	*water*	-0.01	-0.33	-0.31	0.15	-0.31	0.16	0.15	0.31	24d
trans-$[RuCl_4(py)(TMSO)]^-$	*water*	-0.03	-0.37	-0.37	0.15	-0.36	0.16	0.12	0.30	24d

[a] bim: benzimidazole, bpy: 2,2'-bipyridine, 4,4'-bpy: 4,4´-bipyridine, buim: 1-butylimidazole, dcbpy: 4,4'-dicarboxylic acid-2,2'-bipyridine, Et_2S: diethyl sulfide, Me_2S: dimethyl sulfide, DMSO: dimethyl sulfoxide, en: ethylenediamine, Im: imidazole, Ind: indazole, isn: isonicotinamid, Meim: 4-methylimidazole, Mepz: 4-methylpyrazole, Metrz: 1-methyl-1,2,4-triazole, py: pyridine, pz: pyrazole, trz: 1,2,4-triazole, Metrz: 1-methyl-1,2,4-triazole, TMSO: tetramethylene sulfoxide, tz: thiazole.

Figure S1. Calculated vs experimental SRPs. (a) Protocol III, PCM/UAKS, (b) Protocol V, CPCM/UAKS, (c) Protocol VI, CPCM/Bondi. The data are sorted by solvent (color of symbol) and charge (shape of symbol). Aqueous SRPs of the medicinally relevant complexes with the lead structure, trans-$[RuCl_4(L)(L')]^-$, are displayed as filled symbols.

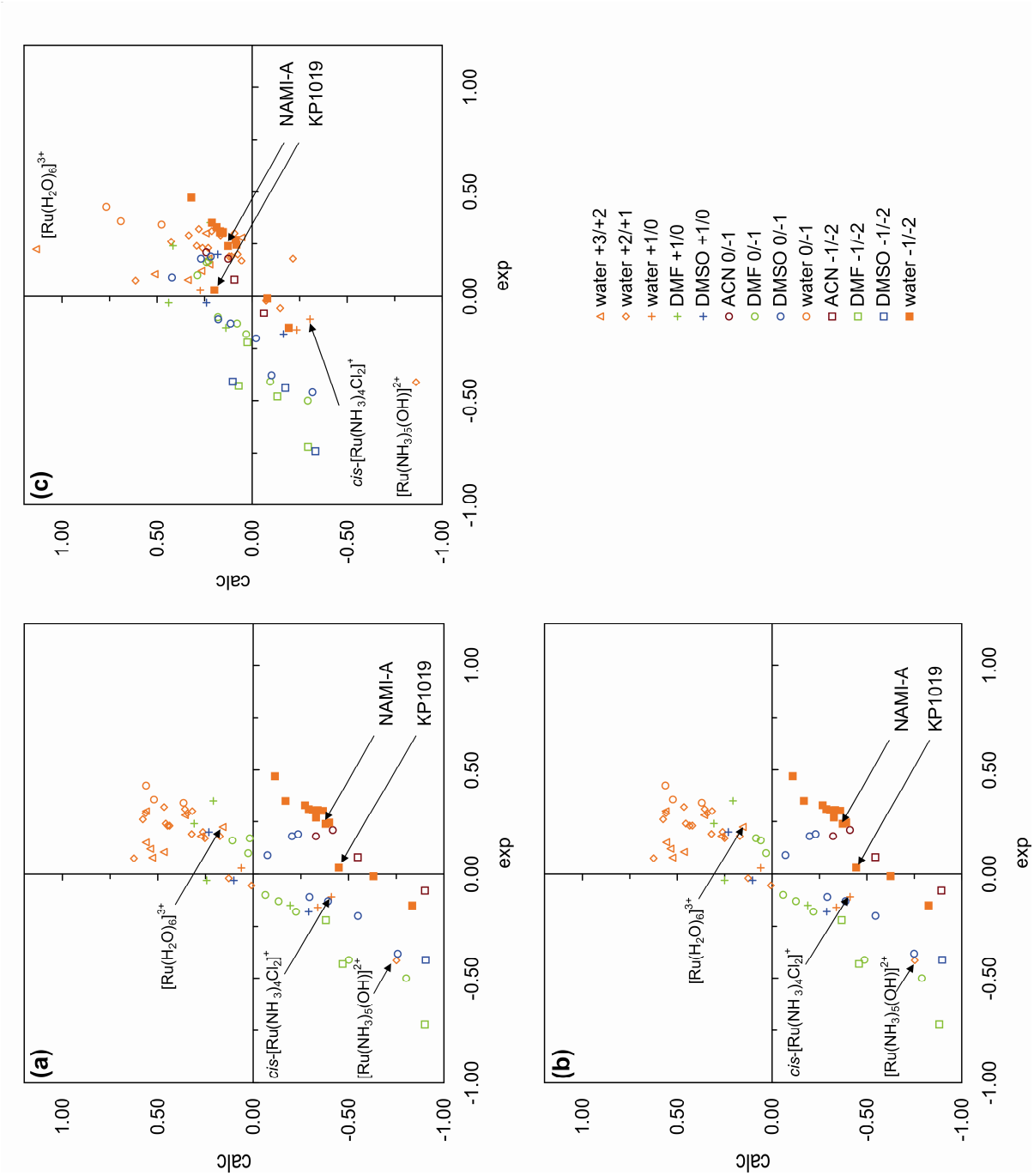

III.7. References

(1) Jung, Y.; Lippard, S. J. *Chem. Rev.* **2007**, *107*, 1387.

(2) Clarke, M. J.; Zhu, F.; Frasca, D. *Chem. Rev.* **1999**, *99*, 2511.

(3) Clarke, M. J. *Coord. Chem. Rev.* **2003**, *236*, 209.

(4) Chifotides, H. T.; Dunbar, K. R. *Acc. Chem. Res.* **2005**, *38*, 146.

(5) (a) Sava, G.; Capozzi, I.; Clerici, K.; Gagliardi, R.; Alessio, E.; Mestroni, G. *Clin. Exp. Metastasis* **1998**, 16, 371. (b) Mestroni, G.; Alessio, E.; Sava, G.; Pacor, S.; Coluccia, M. In *Metal Complexes in Cancer Chemotherapy*. Keppler, B. K., Ed.; VCH: Weinheim, Germany, 1993, p. 157. (c) Sava, G.; Alessio, E.; Bergamo, A.; Mestroni, G. *Top. Biol. Inorg. Chem.* **1999**, *1*, 143. (d) Alessio, E.; Mestroni, G.; Bergamo, A.; Sava, G. In *Metal Ions in Biological Systems*. Sigel, A.; Sigel, H., Ed.; Marcel Dekker: New York, 2004, Vol. 42, p 323.

(6) (a) Keppler, B. K.; Rupp, W.; Juh, U. M.; Enders, H.; Niebl, R.; Balzer, W. *Inorg. Chem.* **1987**, *26*, 4366. (b) Keppler, B. K.; Berger, M. R.; Heim, M. H. *Cancer Treatments Rev.* **1990**, *17*, 261.

(7) (a) Galanski, M.; Arion, V. B.; Jakupec, M. A.; Keppler, B. K. *Curr. Pharm. Des.* **2003**, *9*, 2078. (b) Rademaker-Lakhai, J. M.; van den Bongard, D.; Pluim, D.; Beijnen, J. H.; Schellens, J. H. M. *Clin. Cancer Res.* **2004**, *10*, 3717. (c) Hartinger, C. G.; Zorbas-Seifried, S.; Jakupec, M. A.; Kynast, B.; Zorbas, H.; Keppler, B. K. *J. Inorg. Biochem.* **2006**, *100*, 891.

(8) Yan, Y. K.; Melchart, M.; Habtemariam, A.; Sadler, P. J. *Chem. Comm.* **2005**, *38*, 4764.

(9) Ang, W. H.; Dyson, P. J. *Eur. J. Inorg. Chem.* **2006**, *20*, 4003.

(10) (a) Kelman, A. D.; Clarke, M. J.; Edmonds, S. D.; Peresie, H. J. *J. Clin. Hematol. Oncol.* **1977**, *7*, 274. (b) Clarke, M. J. In *Metal Complexes in Cancer Chemotherapy* Keppler, B. K. Ed.; VCH, Weinheim, 1993, p. 129.

(11) Brown, J. M.; Giaccia, A. J. *Cancer Res.* **1998**, *58*, 1408.

(12) Reisner, E.; Arion, V. B.; Keppler, B. K.; Pombeiro, A. J. L. *Inorg. Chim. Acta* **2007**, doi:10.1016/j.ica.2006/12/005.

(13) Lever, A. B. P. *Inorg. Chem.* **1990**, *29*, 1271.

(14) Wheeler, R. A. *J. Am. Chem. Soc.* **1994**, *116*, 11048.

(15) (a) Cramer, C. J.; Truhlar, D. G. *Chem. Rev.* **1999**, *99*, 2161. (b) Tomasi, J.; Menucci, B.; Cammi, R. *Chem. Rev.* **2005**, *105*, 2999.

(16) Becke, A. D. *J. Chem. Phys.* **1993**, *98*, 5648.

(17) Lee, C.; Yang, W.; Parr, R. G. *Phys. Rev. B* **1988**, *37*, 785.

(18) Takano, Y.; Houk, K. N. *J. Chem. Theory Comput.* **2005**, *1*, 70.

(19) Dutton, A. S.; Fukuto, J. M.; Houk, K. N. *Inorg. Chem.* **2005**, *44*, 4024.

(20) Baik, M.-H.; Friesner, R. A. *J. Phys. Chem. A* .**2002**, *106*, 7407.

(21) Jaque, P.; Marenich, A. V.; Cramer, C. J.; Truhlar, D. G. *J. Phys. Chem. C* **2007**, *111*, 5783.

(22) Besker, N.; Coletti, C.; Marrone, A.; Re, N. *J. Phys. Chem. B.* **2007**, *111*, 9955.

(23) (a) Chen, J.; Chen, L.; Liao, S.; Zheng, K.; Ji, L. *J. Phys. Chem. B* **2007**, *111*, 7862. (b) Chen, J.; Chen, L.; Liao, S.; Zheng, K.; Ji, L. *Dalton Trans*, **2007**, *32*, 3507.

(24) (a) Marchant, J. A.; Matsubara, T.; Ford, P. C. *Inorg. Chem.* **1977**, *16*, 2160. (b) Yee, E. L.; Cave, R. J.; Guyer, K. L.; Tyma, P. D.; Weaver, M. J. *J. Am. Chem. Soc.* **1979**, *101*, 1131. (c) Costa, G.; Balducci, G.; Alessio, E.; Tavagnacco, C.; Mestroni, G. *J. Electroanal. Chem.* **1990**, *296*, 57. (d) Alessio, E.; Balducci, G.; Lutman, A.; Mestroni, G.; Calligaris, M.; Attia, W. M. *Inorg. Chim. Acta* **1993**, *203*, 205. (e) Mestroni, G.; Alessio, E.; Sava, G.; Pacor, S.; Coluccia, M.; Boccarelli, A. *Metal Based Drugs* **1993**, *1*, 41. (f) Dhubhghaill, N.; Orla M.; Hagen, W. R.; Keppler, B. K.; Lipponer, K.-G.; Sadler, P. J. *J. Chem. Soc., Dalton Trans.* **1994**, 3305. (g) Clarke, M. J.; Bailey, V. M; Doan, P. E; Hiller, C. D.; LaChance-Galang, K. J.; Daghlian, H.; Mandal, S.; Bastos, C. M.; Lang, D. *Inorg. Chem.* **1996**, *35*, 4896. (h) Mura, P.; Camalli, M.; Messori, L.; Piccioli, F.; Zanello, P.; Corsini, M. *Inorg. Chem.* **2004**, *43*, 3863. (i) Eskelinen, E.; Da Costa, P.; Haukka, M. *J. Electroanal. Chem.* **2005**, *579*, 257.

(25) (a) Reisner, E.; Arion, V. B.; Guedes da Silva, M. F. C.; Lichtenecker, R.; Eichinger, A.; Keppler, B. K.; Kukushkin, V. Yu.; Pombeiro, A. J. L. *Inorg. Chem.* **2004**, *43*, 7083. (b) Egger, A.; Arion, V. B.; Reisner, E.; Cebrian-Losantos, B.; Shova, S.; Trettenhahn, G.; Keppler, B. K. *Inorg. Chem.* **2005**, *44*, 122. (c) Reisner, E.; Arion, V. B.; Eichinger, A.; Kandler, N.; Giester, G.; Pombeiro, A. J. L.; Keppler, B. K. *Inorg. Chem.* **2005**, *44*, 6704.

(26) Ravera, M.; Baracco, S.; Cassino, C.; Zanello, P.; Osella, D. *Dalton. Trans.* **2004**, 2347.

(27) Note that there is a relatively small but noticeable dependence of the experimental SRPs on ionic strength and pH, with typical changes amounting to ~0.02 V.[24b,26] Most complexes in aqueous solution were measured at pH ~ 7, but some of them had to be measured at low pH (e.g., $[Ru(NH_3)_5(OH_2)]^{3+}$) or high pH (e.g., $[Ru(NH_3)_5(OH)]^{2+}$),[24b] due to likely changes in the protonation state of the ligands upon reduction at neutral pH. A change in the protonation state upon reduction certainly alters the measured SRP, as was described, e.g., for *trans*-$[RuCl_2(trz)_4]Cl$, in ref. 25c.

(28) Kirlin, W. G.; Cai, J.; Thompson, S. A.; Diaz, D.; Kavanagh, T. J.; Jones, D. P. *Free Rad. Biol. Med.* **1999**, *27*, 1208.

(29) Gaussian 03, Revision D.01, Frisch, M. J. et al., Gaussian, Inc., Wallingford CT, **2004**. www.gaussian.com

(30) Andrae, D.; Haeussermann, U.; Dolg, M.; Stoll, H.; Preuss, H. *Theor. Chim. Acta* **1990**, *77*, 123.

(31) Bergner, A.; Dolg, M.; Kuechle, W.; Stoll, H.; Preuss, H. *Mol. Phys.* **1993**, *80*, 1431.

(32) (a) Hehre, W. J.; Ditchfield, R.; Pople, J. A. *J. Chem. Phys.* **1972**, *56*, 2257. (b) Binkley, J. S.; Pople, J. A.; Hehre, W. J. *J. Am. Chem. Soc.* **1980**, *102*, 939.

(33) Martin, J. M. L.; Sundermann, A. *J. Chem. Phys.* **2001**, *114*, 3408.

(34) (a) Miertus, S.; Scrocco, E.; Tomasi, J. *Chem. Phys.* **1981**, *55*, 117. (b) Tomasi, J.; Persico, M. *Chem. Rev.* **1994**, *94*, 2027.

(35) Cances, M. T.; Mennucci, B.; Tomasi, J. *J. Chem. Phys.* **1997**, *107*, 3032. (b) Cossi, M.; Scalmani, G.; Rega, N.; Barone, V. *J. Chem. Phys.* **2002**, *117*, 43.

(36) Klamt, A.; Schuurmann, G. *J. Chem. Soc.; Perkin Trans. 2* **1993**, 799.

(37) Barone, V.; Cossi, M. *J. Phys. Chem. A* **1998**, *102*, 1995.

(38) (a) Tannor, D. J.; Marten, B.; Murphy, R. B.; Friesner, R. A.; Sitkoff, D.; Nicholls, A.; Ringnalda, M. N.; Goddard, W. A., III; Honig, B. *J. Am. Chem. Soc.* **1994**, *116*, 11875. (b) Marten, B.; Kim, K.; Cortis, C.; Friesner, R. A.; Murphy, R. B.; Ringnalda, M. N.; Sitkoff, D.; Honig, B. *J. Phys. Chem.* **1996**, *100*, 11775. (c) Edinger, S. R.; Cortis, C.; Shenkin, P. S.; Friesner, R. A. *J. Phys. Chem.* **1997**, *101*, 1190. (d) Friedrichs, M.; Zhou, R. H.; Edinger, S. R.; Friesner, R. A. *J. Phys. Chem. B* **1999**, *103*, 3057.

(39) Jaguar, version 7.0, Schrödinger, LCC, New York, NY, 2007. www.schrodinger.com

(40) Dielectric constants ε of solvents in Gaussian 03: acetonitrile (ACN) 36.64, dimethyl formamide (DMF) 36.7, dimethyl sulfoxide (DMSO) 46.7, water 78.39. In Jaguar 7: ACN 37.5, DMF 36.7, DMSO 47.24, water 80.37.

(41) Hay, P. J.; Wadt, W. R. *J. Chem. Phys.* **1985,** *82*, 299.

(42) Ben-Naim, A.; Marcus, Y. *J. Chem. Phys.* **1984**, *81*, 2016.

(43) Rappe, A. K.; Casewit, C. J.; Colwell, K. S.; Goddart, W. A., III; Skiff, W. M. *J. Am. Chem. Soc.* **1992**, *114*, 10024.

(44) Barone, V.; Cossi, M.; Tomasi, J. *J. Chem. Phys.* **1997**, *107*, 3210.

(45) Perdew, J. P.; Burke, K.; Ernzerhof, M. *Phys. Rev. Lett.* **1996**, *77*, 3865.

(46) Bondi, A. *J. Phys. Chem.* **1964**, *68*, 441.

(47) Pierotti, R. A. *Chem. Rev.* **1976**, *76*, 717.

(48) Lee, B.; Richards F. M. *J. Mol. Biol.* **1971**, *55*, 379.

(49) 1.2 for *water* and *DMF*; 1.4 for *ACN* and *DMSO*

(50) For an alternative approach, see: (a) Tavernelli, I.; Vuilleumier, R.; Sprik, M. *Phys. Rev. Lett.* **2002**, *88*, 213002-1. (b) Blumberger, J.; Sprik, M. *J. Phys. Chem. B* **2005**, *109*, 6793. (c) Blumberger, J.; Sprik, M. *Theor. Chem. Acc.* **2006**, *115*, 113.

(51) Jorgensen, W. L.; Briggs, J. M.; Gao, J. *J. Am. Chem. Soc.* **1987**, *109*, 6857.

(52) Lewis, A.; Bumpus, J. A.; Truhlar, D. G.; Cramer, C. J. *J. Chem. Ed.* **2004**, *81*, 596 incl. Addition/Correction.

(53) Born, M. *Z. Physik* **1920**, *1*, 45.

(54) (a) Deubel, D. V. *J. Am. Chem. Soc.* **2004**, *126*, 5999. (b) Lau, J. K.-C.; Deubel, D. V. *Chem. Eur. J.* **2005**, *11*, 2849. (c) Lau, J. K.-C.; Deubel, D. V. *J. Chem. Theory Comput.* **2006**, *2*, 103. (d) Deubel, D. V. *J. Am. Chem. Soc.* **2006**, *128*, 1654. (e) Deubel, D. V.; Chifotides, H. T. *Chem. Comm.* **2007**, 3438.

(55) (a) Baik, M.-H.; Friesner, R. A.; Lippard, S. J. *J. Am. Chem. Soc.* **2002**, *124*, 4495. (b) Baik, M.-H.; Friesner, R. A.; Lippard, S. J. *J. Am. Chem. Soc.* **2003**, *125*, 14082. (c) Mantri, Y.; Lippard, S. J.; Baik, M.-H. *J. Am. Chem. Soc.* **2007**, *129*, 5023.

(56) The experimental SRP is 0.23 V; we report in the text the calculated deviations from this value. Vanýsek, P. In *CRC Handbook of Chemistry and Physics*, 87th ed.; Lide, D. R., Ed.; CRC Taylor and Francis: Boca Raton, FL, 2006; p. 8-24 and 8-26.

(57) Kelly, C. P.; Cramer, C. J.; Truhlar, D. G. *J. Chem. Theory Comput.* **2005**, *1*, 1133.

(58) NIST Chemistry Webbook, http://webbook.nist.gov/

(59) Tissandier, M. D.; Cowen, K. A.; Fendg, W. Y.; Gundlach, E.; Cohen, M. H.; Earhart, A. D.; Coe, J. V,; Tuttle, T. R. *J. Phys. Chem. A* **1998,** *102*, 7787.

(60) Liptak, M. D.; Shields, G. C. *J. Am. Chem. Soc.* **2001**, *123*, 7314.

(61) Trasatti, S. *J. Electroanal. Chem.* **1974,** *52*, 313.

(62) Farrell, J. R.; NcTigue, P. *J. Electroanal. Chem.* **1982**, *37*, 139

(63) Trasatti, S. *Pure & Appl. Chem.* **1986,** *58*, 955.

(64) Reiss, H; Heller, A. *J. Phys. Chem.* **1985**, *89*, 4207.

IV. Density Functional Study of Ruthenium(III) Anticancer Complexes

IV.1. Abstract

The chemical behavior of four potential anticancer ruthenium(III) species: *trans*-tetrachloridobis(1H-imidazole)ruthenate(III) (ICR), *trans*-tetrachloridobis(1H-pyrazole)ruthenate(III), *trans*-tetrachlorido(dimethylsulfoxide)imidazoleruthenate(III) (NAMI-A) and *trans*-tetrachloridobis(1H-indazole)ruthenate(III) (KP1019) and their reduced analogs has been explored by high level quantum calculation. The electronic aspects governing their electrochemistry have been investigated by using the bond energy decomposition analysis revealing the role of π-electron acceptor character of DMSO and indazole ligands in stabilization of Ru(II) species. Influence of the electron donor properties of the protein and DNA models directly bound to the metal, the medium pH and dielectric constant on the standard redox potentials have been examined. Furthermore, the mechanistic aspects of the aquation process have been studied in detail. In agreement with experimental data available and contrary to part of the previous computational works we have found the preference for the interchange mechanism of dissociative character (**Id**) for aquation of Ru(III) species. Moreover, for the first time we have studied the limiting dissociative mechanism (**D**) of the aquation of Ru(II) analogs and have found it to be prefered over the interchange mechanism. The importance of aquation products, mono- and *cis*-di-aqua complexes, as precursors for the biological actions is analyzed. The kinetics and thermodynamics of reactions towards biomodels have been computed and no clear preference for either nitrogen or sulfur protein binding sites was found. In the binding to isolated purinic nucleobases, to model the reaction with DNA, the kinetic preference for binding guanine over adenine is found for the reduced *cis*-di-aqua complexes; the characteristic transition structures being stabilized by a hydrogen bonding pattern similar to cisplatin reactions. The hydrogen bond between guanine O6 and *cis*-aqua ligand stabilizes the reaction products in both oxidation states. The possible involvement of Ru(III) complexes in the redox cycling inside the cancer cell that can catalyze generation of reactive hydroxyl radicals is discussed as well.

IV.2. Introduction

Globally one half of all tumor therapies are based on three platinum complexes: cisplatin, carboplatin, and oxaliplatin.[1] Since the discovery of the antineoplastic properties of cisplatin[2] a continuous search for platinum and other transition metal complexes with similar properties has been pursued. High toxicity of cisplatin along with wide range of side effects, and its inactivity against a number of carcinomas are the reasons of increasing interests in other metallopharmaceuticalls. Studies on the promising complexes of gallium,[3] rhodium[4] and ruthenium[5] which show a remarkable anticancer potential are ongoing and attract more and more scientists worldwide. Two Ru(III) complexes NAMI-A[6] (imidazolium [*trans*-tetrachlorido(dimethylsulfoxide)imidazoleruthenate(III)]) and KP1019[7] (indazolium [*trans*-tetrachloridobis(1H-indazole)ruthenate(III)]) (Chart 1) successfully completed phase I clinical trials[8] and have started (NAMI-A) a phase II study.[9] Recent developments of organometalic Ru(II) anticancer complexes are promising as well.[10]

The cisplatin mode of action[1] is well established and described by the binding of the products of cisplatin aquation at two adjacent guanine DNA sites, and subsequent cell apoptosis after the recognition of structurally modified DNA. Relatively little is known about the mode of action of other transition metal potential anticancer drugs, but their different coordination chemistry, reactivity, the capacity of replacement of essential metals, and the redox behavior most likely induce a biologically different mode of action. Due to their reduced general toxicity, as compared to platinum compounds, and their high activity against platinum-based drugs resistant tumors, Ru(III) complexes appear to be the most promising alternatives as anticancer metallopharmaceuticals.[5] Due to the similarity of their coordination chemistry, ruthenium resembles iron in the binding to albumin and transferrin.[11] This could partially explain the lower toxicity of the ruthenium compounds in comparison to platinum-based drugs. The delivery of the octahedral ruthenium compounds to the cell is mediated by transferrin receptor endocytosis which is less likely to operate in the case of square planar platinum(II) compounds. Although they are capable of binding to these proteins as well, contrary to the ruthenium complexes, this process is supposed to contribute to the drug administration side effects.[12]

Ru(III) complexes are believed to be activated *in vivo* upon reduction to their more reactive Ru(II) analogs.[13] A selective reduction in cancer cells occurs likely due to the reducing environment caused by deficiency of molecular oxygen in tumors (*hypoxia*),[14] as the blood flow to the rapidly growing tumor is insufficient. However, the prodrugs could be reduced prior reaching the reducing milieu in tumors, e.g. as a result of aquation, the resulting products of which have different redox properties than the initial prodrug. In particular, the first step aquation product of KP1019 ($[Ru^{III}Cl_3(H_2O)(Hind)_2]$; Hind = 1H-indazole) ($E_{1/2}$ = –0.16 V *vs.* NHE in DMF) is significantly easier to reduce than the administered non-aquated prodrug ($E_{p/2}$ = –0.43 V *vs.* NHE in DMF).[15]

A major contribution to the understanding of the mode of action of metallo-drugs is attained by modern quantum chemistry. The transition structures and reaction intermediates, which are difficult to detect experimentally, are accessible *in silico*, and the elementary reaction steps can be precisely explored. Experimentally proposed and theoretically possible competing mechanisms can be rigorously investigated by computation chemists shedding light into the biological mystery of the metal complexes anticancer potency. Many quantum chemical studies focused on the cisplatin aquation[16] and the subsequent binding of the aquation products to DNA bases.[17] On the other hand, considerably less computational work was dedicated to other anticancer metal complexes. In particular, for the promising anticancer Ru(III) compounds, at the moment of writing, only aquation mechanisms of NAMI-A,[18] ICR[18b,19] (imidazolium [*trans*-tetrachloridobis(imidazole)ruthenate(III)]), TzICR (thiazolium [*trans*-tetrachloridobis(thiazole)ruthenate(III)]) and (2-NH_2)TzICR ((2-aminothiazolium [*trans*-tetrachloridobis(2-amminothiazole)ruthenate(III)])[18d] were investigated. The thermodynamics of the binding of Ru(II) and Ru(III) complexes to DNA by investigating monofunctional ruthenium complexes of the formula $[Ru(NH_3)_5B]^{Z+}$ (Z = 2,3), where B is a nucleobase or a protein model was studied as well,[20] revealing the preference for guanine over adenine binding for both Ru(II) and Ru(III) complexes.

Chart 1. NAMI-A and KP1019, successful Ru(III) anticancer complexes in clinical trials

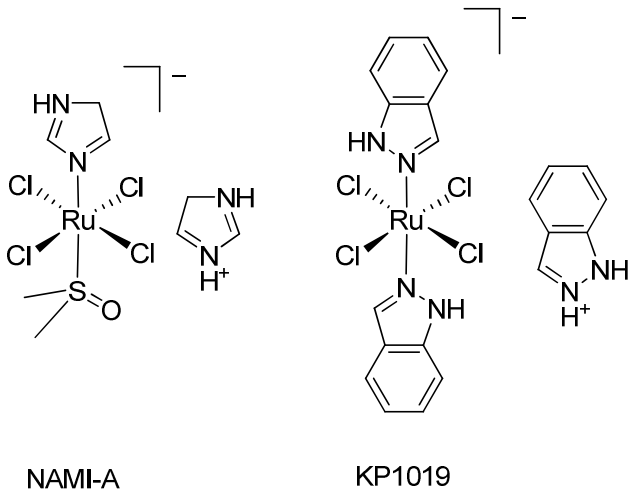

NAMI-A KP1019

In order to understand the mechanism of action of octahedral Ru(III) anticancer agents we have systematically investigated: (i) the aquation of the Ru(III) compounds; (ii) the effect of the axial ligands, pH, environment and the protein binding on their redox behavior; and (iii) the kinetic and thermodynamic aspects of the binding towards proteins and DNA models. For this purpose an *in silico* four-species-evolution approach (Chart 2, **1–4**) (similar to the one used previously[21]) which includes *trans*-tetrachloridobis(1H-imidazole)ruthenate(III) (ICR, **2–Cl**) and *trans*-tetrachloridobis(1H-pyrazole)ruthenate(III) (**3–Cl**) to rationally connect two successful Ru(III) anticancer drugs NAMI-A (**1–Cl**) and KP1019 (**4–Cl**) were investigated. (For the sake of clarity from this point down we will refer to the tetrachlorido complexes without specifying explicitly the functional group in the designator, i.e. by **1** we refer to NAMI-A and by **5** to its reduced form, respectively, instead of using **1–Cl** and **5–Cl**). Experimental observation that only aged aqueous solution of ICR (**2**) reacts with DNA,[22] supports the assumption that, similarly to cisplatin, the aquation products of Ru(III) complexes being more reactive than their parent chlorido complexes once formed are the subject of substitution. The reactivity of aquated species towards relevant nitrogen and sulfur nucleophiles has been studied by using a collection of functional groups employed in similar computations on cisplatin[16e,23] and organometalic Ru(II) complexes.[16e] The library (Chart 2) contains small nitrogen $\mathbf{NH_3}$ and sulfur $\mathbf{H_2S}$ nucleophiles and protein models: methylamine representing terminal amino group; imidazole representing histidine; dimethylsulfide representing methionine; methylthiolate and methylthiol representing glutathione and cysteine in their deprotonated and protonated forms respectively. Guanine and adenine were used as DNA models. The standard redox potentials (SRPs) of chlorido

complexes and their monosubstituted derivatives have been computed and the factors influencing the SRPs rationalized. Because the "activation-by-reduction" hypothesis suggests that Ru(II) species are responsible for anticancer activity of ruthenium drugs, the aquation of reduced species and their binding to biological models have been investigated as well.

Chart 2. Metal complexes and biological relevant substituent models

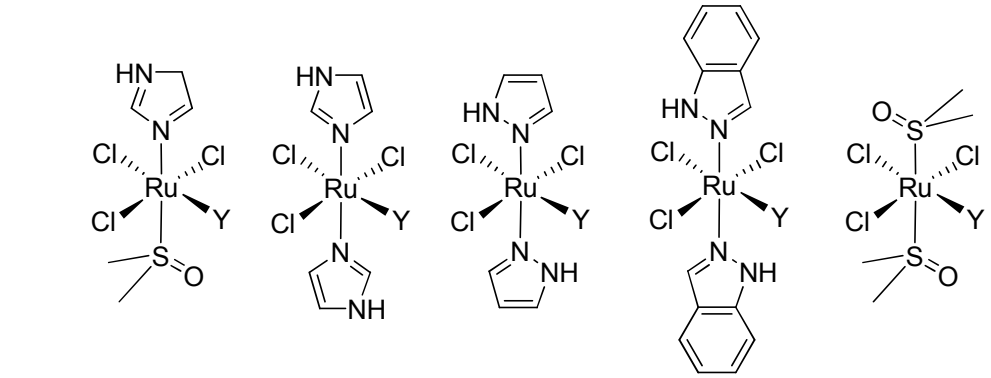

Ru(III) = **1** **2** **3** **4** **9**

Ru(II) = **5** **6** **7** **8** **10**

Y=

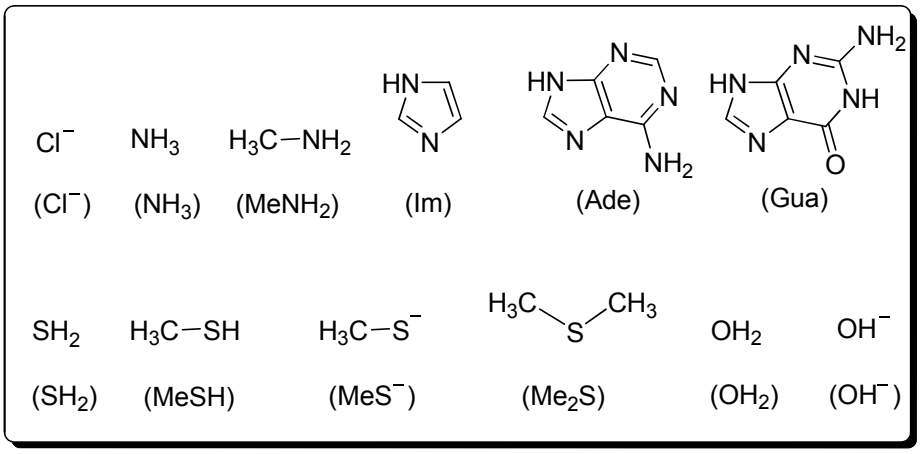

IV.3. Aquation mechanism of ruthenium anticancer agents

The aquation is the replacement process of a ligand in an inorganic complex by a water molecule. The abundance of water molecules at physiological conditions makes metallo-drugs susceptible to aquation. The process, being the crucial step of the *in vivo* transformations of cisplatin, determines its ultimate success as anticancer drug. Experimental evidence that only aged aqueous solution of ICR reacts with DNA,[22] suggests that similarly to cisplatin, the aquation products of ruthenium drugs, being more reactive than their parent

chlorido complexes are the active forms of the drug. Moreover, the high lability of the aqua ligand in mono-aqua derivative of KP1019 suggests that this complex is the potential active species responsible for the antitumor activity of KP1019.[24] The common "activation by reduction" hypothesis[13] does not exclude the aquation as being an important step in the ruthenium anticancer activity. Therefore, it is not surprising that the aquation has been the subject of many experimental and, since recently, of computational studies.[18,19]

Although the importance of detailed understanding of aquation process is essential, the lack of experimentally relevant data and the variety of possible pathways make the assessment of the aquation mechanism of Ru(III) compounds a real challenge for chemists. Figure 1 represents the mechanism types in a water exchange process. The associative (**A**) and dissociative (**D**) substitution reaction mechanisms proceed in two steps and involve intermediates with an increased or a decreased coordination number, respectively. The experimental evidences for these limiting mechanisms are restricted by the fact that the intermediates are not always detectable, because of their short lifetime. If the experimental detection of intermediates is not possible, by default, an interchange mechanism is assumed, in which formation of the metal bond with the entering ligand is concerted with weakening of the metal bond with the leaving group. The transition state is characterized by weak bonding of both the leaving, and the entering ligands. If bond formation is more pronounced than the bond breaking, the mechanism is called associative interchange (**Ia**); otherwise (if bond breaking dominates) the dissociative interchange (**Id**) mechanism operates. For the interchange (**I**) mechanism the same extent of the bond formation and breaking is characteristic. In addition to the investigation of the presence or absence of reaction intermediates, the information about the intrinsic mechanism of the substitution process is obtained by experimentally measuring the activation parameters entropy ($\Delta S^{\#}$) and volume ($\Delta V^{\#}$), as well. A positive value of the activation volume or activation entropy is characteristic for **Id** or **D** mechanisms. In contrast, the negative sign of the activation volume and activation entropy is characteristic for **Ia** or **A** mechanisms. One should note that the activation entropy alone is not a measure of the experimental assessment of the reaction mechanism, as it depends not only on the bond strength at the transition states, but also on other factors[25] described for the phosphate monoester hydrolysis (e.g.: steric factors that determine the configurational volumes available to the reactants during the reaction, solvation and desolvation effects that may be associated with charge redistribution upon approaching the transition state, entropy changes associated with intramolecular degrees of freedom as the

transition state is approached, etc). To assess theoretically the reaction mechanism, the investigation of all the species involved (reactants, transition states, intermediates and products) is mandatory. The subsequent investigation of the computed reaction profiles determines the most plausible reaction pathway and implicitly mechanism for the given process. The decisive assignment of the mechanism is done by combining both experimental and theoretical studies.[26]

Figure 1. Schematic representation of the substitution mechanism types in a water exchange process. The colored circles define the positions of entering and leaving ligands relative to the central metal atom in transition structures. Heptacoordinate and pentacoordinate intermediates are generated during the substitution reactions proceeding via limiting **A** or **D** mechanisms respectively.

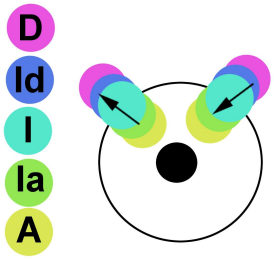

Theoretical studies available in the literature on platinum anticancer complexes suggest the aquation process to follow an interchange mechanism of associative character (Table 1). Recently, the influence of the electronic interaction of the metal orbitals with the ligands in *trans* position to aqua on the water exchange mechanism was systematically investigated for the square-planar Pt(II) compounds,[27] and the correlation between the electron donor abilities of the *trans* ligand on the substitution mechanism was revealed. Supported by the decomposition and natural orbital analyses, two cases where the most favorable mechanism was found to be different form the commonly accepted **Ia** for the water exchange process at Pt(II) centers were found. The substitution proceeds via an **Id** mechanism if the *trans* ligand is a strong σ donor (e.g. CH_3^-), and via a limiting **A** mechanism in the case of compounds bearing ligands such as C_2H_4 and CO in *trans* position which can lower considerably the electron density at the metal, due to π-back donation. Because there is a smaller number of the computation studies on ruthenium compounds, discrepant in some cases (Table 1) the dispute on their aquation mechanism is still not

finished. By performing calculations at carefully tested theoretical level[28] the most viable mechanism can be found.

Table 1. Aquation mechanisms of different anticancer metallo-drugs. $\Sigma_{TS}-\Sigma_{RA}$: difference between the lengths sum of the bonds formed and broken during the aquation in TS and reactants adduct (RA).

compound				Exp. activation parameters			
	$\Sigma_{TS}-\Sigma_{RA}$	Mec[a]	ref	ΔH	ΔS	Mec	ref
	Å			kJ/mol	J/mol×K		
Cisplatin	–0.85	**Ia**	16a	19.7	–15	**Ia**	29
	–0.83	**Ia**[b]	16a				
	–0.42	**Ia**	30				
	–0.96	**Ia**[b]	16d				
trans-$[Pt(NH_3)_2L^T(H_2O)]^{n+}$			27				
$L^T = H_2O$		**Ia**[c]	-				
$L^T = Cl^-$		**Ia**[c]	-				
$L^T = CH_3^-$		**Id**[c]	-				
$L^T = C_2H_4$		**A**[c]	-				
Carboplatin				88.4	–15	**Ia**	31
Oxaliplatin	–0.68	**Ia**	32				
	–0.54	**Ia**[b]	32				
Rhodium tetracarboxylate				49.0 ± 1.0	–60	**Ia**	33
$[(\eta^6\text{-benzene})Ru^{II}(en)Cl]^+$		**Ia**	21	79.5 ± 3.4	–30.8 ± 11.5	**Ia**	34
	–0.88	**Ia**	35				
	–0.58	**Ia**[b]	35				
NAMI-A	–0.49	**Ia**	18c				
	0.26	**Id**[b,c]	18c				
	–1.20	**Ia**	18a				
		Id[c]	18b				
	1.58	**Id**	this work				
Ru^{II} analog of NAMI-A		**Id**[c]	18b				
		D	this work				
ICR	–0.69	**Ia**	19	117.0 ± 7.0	55.0 ± 23.0	**Id**	36
		Id[c]	18b				
	1.33	**Id**	this work				
Ru^{II} analog of ICR		**Id**[c]	18b				
		D	this work				
TzICR	0.01	**I**	18d				
$(2\text{-}NH_2)$TzICR	–0.09	**Ia**	18d				
KP1019		**Id**	this work				
Ru^{II} analog of KP1019		**D**	this work				
trans-$[Ru^{III}Cl_4(Hpz)_2]^-$		**Id**	this work				
trans-$[Ru^{II}Cl_4(Hpz)_2]^{2-}$		**D**	this work				

[a] mechanism

[b] optimizations in solution.

[c] mechanism assignment is made by the authors. All other mechanism types are our estimations either from $\Sigma_{TS}-\Sigma_{RA}$ parameter value or from the activation entropy.

Similarly to the $\Delta\Sigma d(M–O)$ criterion[37] used to ascribe the mechanism of water exchange reaction of transition metal complexes, we use the sum of the lengths change of the two bonds involved in the aquation (metal–entering (*E*) and metal–leaving (*L*) ligands) to evaluate the mechanism of the potent anticancer agents, available in the literature (Table S1 in *Supporting Info*). The only usage of the bonds directly involved in the substitution reaction is imposed by the fact that they are generally provided in the literature, at the same time the spectator metal–ligand bonds (which do not participate in the aquation) do not change dramatically, and consequently do not influence the activation volume at the same extent as the bonds broken and formed during the process. For this purpose, in contrast to the rest of the work, we considered the optimization of the reactant complexes involved in the aquation process as well. A good correlation between the mechanisms predicted by the $\Sigma_{TS}–\Sigma_{RA}$[38] parameter and the experimental mechanisms (deduced from the activation entropy value) is found for aquation of platinum, rhodium and piano-stool type Ru(II) arene complexes. This is not true for NAMI-A, aquation mechanism of which is described by two different mechanisms in the literature. While the authors of the references 18c and 18a were able to reproduce quantitatively the experimentally measured aquation rate constants, their predicted activation mechanisms are different. By optimizing all the species involved in the chlorido aquation, up to the second step (molecules, intermediates and transition states), and by drawing the free energy profiles, we aim to reveal the aquation mechanism, as well as to reproduce experimentally available kinetic and thermodynamic data. However, one should note that partial substitution of DMSO ligand in NAMI-A by water molecule was observed experimentally at physiological pH as well.[39]

IV.3.1. Aquation of Ru(III) complexes

Figure 2 displays the energy profile corresponding to the interchange aquation mechanism (Scheme 1) of Ru(III) complexes **1–4** up to the second aquation step. The activation free energies of the first aquation step are comparable (ΔG_a = 24.9–28.6 kcal/mol, Table 2), with the lowest activation barrier computed for **3**. This may be due to strong hydrogen bonding stabilization of the transition structure, that has, additionally to the hydrogen bonding between water's hydrogen and leaving Cl ($d_{H\cdots Cl}$ = 2.07–3.17 Å) found in all **TS**, strong hydrogen bonding interactions (Figure 3) between the entering water molecule

and the N–H site of the axial pyrazole ($d_{O\cdots H}$ = 1.62 Å) and between leaving Cl ligand and the N–H of the second pyrazole ($d_{Cl\cdots H}$ = 2.01 Å). The indazole ligand, which like pyrazole has the N–H site available for hydrogen bonding in transition states, stabilizes only the leaving Cl ligand ($d_{Cl\cdots H}$ = 1.96 Å). The corresponding stabilization of water molecule by hydrogen bonding to N–H of the second indazole ligand was not possible to reproduce. The reactions are endergonic (Table 2), the exception is ΔG_r = –0.8 kcal/mol of the first aquation step of NAMI-A. The computed rate constants are in good agreement with experimental data (Table 2). The formation of the *cis* di-aqua isomers in the second aquation step is both kinetically and thermodynamically preferred over the *trans* isomers (Table 2, Figure 2) in agreement with previously computed data.[18b] At physiological conditions, the deprotonation of aqua ligand of the mono-aqua complexes readily occurs (computed pK_a values are quoted in Table 3 and Table S4) and the most abundant aquation products are mono-hydroxido derivatives of the initial complexes.

Figure 2. Free energy profile of the aquation of Ru(III) complexes up to the second step. Free energies (kcal/mol) are calculated with respect to the separated reactants.

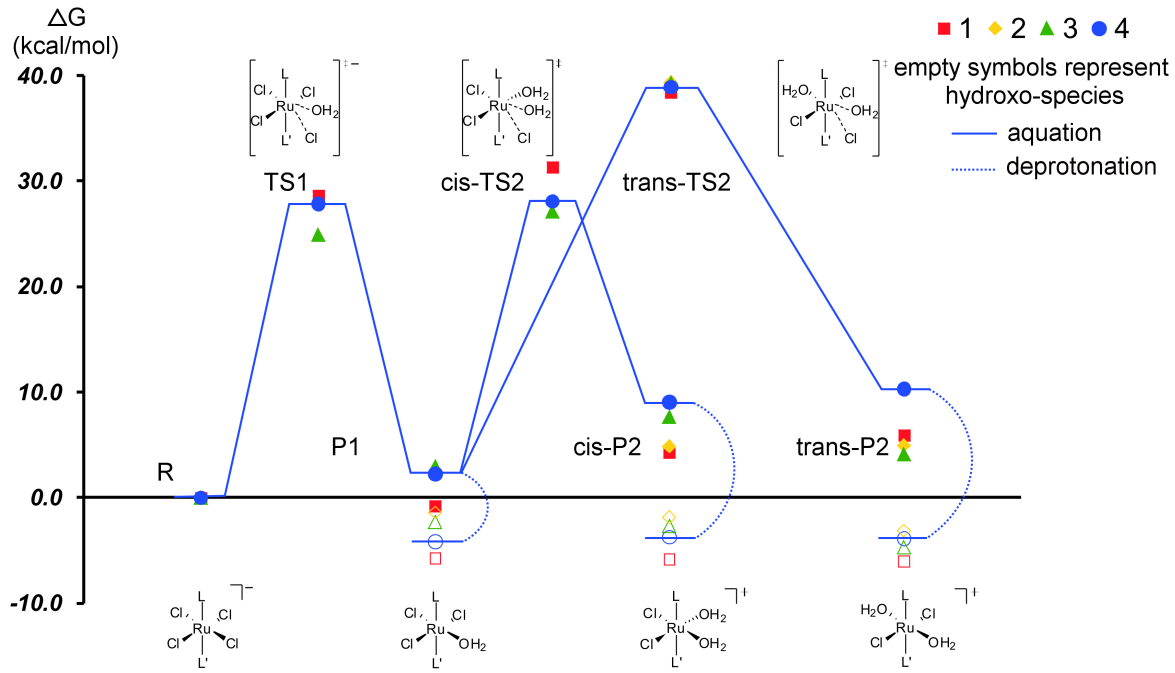

Scheme 1. Interchange mechanism of the first aquation step of Ru(III) complexes

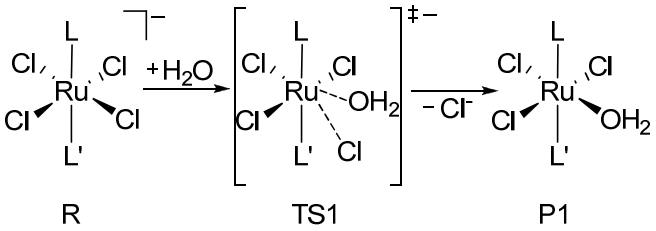

1: L = Im, L' = DMSO; **2**: L = L' = Im; **3**: L = L'= pz; **4**: L = L' = Ind

Table 2. Free energies relative to separated reactants of the species involved in the aquation process of **1–4** up to the second step (kcal/mol). Reaction rates for the first aquation step (s^{-1})

	R	TS1[a]	P1	*cis*-TS2	*cis*-P2	*trans*-TS2	*trans*-P2	k (calc)	k (exp)[40]
1	0	28.6	–0.8	31.3	4.3	38.4	5.9	3.6×10^{-7}	1.4×10^{-7}–3.1×10^{-6}
2	0	27.8	2.3	28.1	4.8	39.3	4.9	1.4×10^{-6}	1.1×10^{-5}
3	0	24.9	3.0	27.1	7.6	39.3	7.8	1.9×10^{-4}	
4	0	27.8	2.3	28.0	9.0	38.9	10.3	1.4×10^{-6}	0.4×10^{-5}

[a] the digits represents the aquation step; R, TS and P stand for reactants, transition states and products respectively

Figure 3. Hydrogen bonding pattern in computed transition state of the first aquation step of **3**

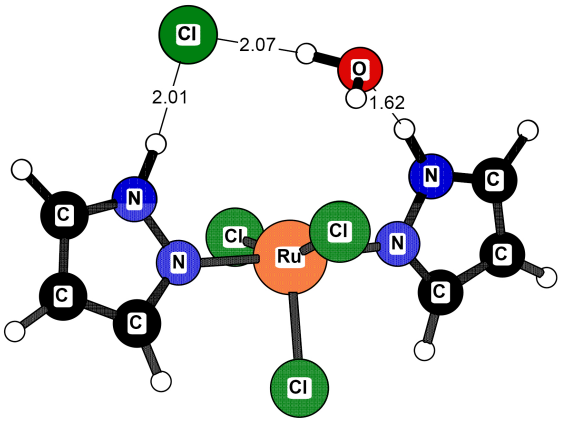

Table 3. Absolute pK_a values of aqua and thiol complexes

	OH_2	**MeSH**
1–Y	3.4	–0.9
2–Y	4.3	–1.4
3–Y	3.1	–2.6
4–Y	2.3	–3.1
5–Y	18.6	10.9
6–Y	16.4	11.3
7–Y	16.0	11.3
8–Y	12.7	10.5

By taking into account the solvent effects by means of implicit solvation models during optimizations, the authors in ref. 18c found the transition structure characteristic for an interchange mechanism with dissociative character (**Id**) of aquation of **1** (positive (Σ_{TS}–Σ_{RA}) parameter in Table 1) contrary to the associative character (**Ia**) found when the optimization is carried out *in vacuo*.[18c] One should note that in these calculations additional three explicit water molecules were employed to simulate the first shell solvation interactions. Our model predicts even stronger dissociative character of the interchange mechanism:[41] (Σ_{TS}–Σ_{RA}) = 1.58 *vs* 0.26 (Table 1). Moreover, we found geometrical differences in the transition structures optimized by us, as compared to the TSs described in the ref. 19, mostly related to the length of the metal-ligand bonds involved in aquation. For ICR (**2**) aquation, our model predicts a strong dissociative character of the interchange mechanism in contrast to the **Ia** mechanism described previously[19] (Σ_{TS}–Σ_{RA} = 1.33 vs –0.69), but in agreement with more recent computations.[18b] The experimental positive value of the activation entropy supports our findings that the aquation of ICR occurs via an **Id** mechanism and the reliability of our model. Moreover, we tried to investigate the **Ia** mechanism, by optimizing a more compact transition state (similar to the one obtained by the authors of the ref 19) and obtained a higher kinetic preference for the **Id** mechanistic path characterized by an activation barrier of aquation lower by 6 kcal/mol.

IV.3.2. Aquation of Ru(II) complexes

In transition metals series the mechanism of water exchange at the metal center changes as function of occupancy of d orbitals, the coordination number and the ionic radius

of the central metal. In extreme case of Ga(III) complexes with electronic configuration d^{10} substitution proceeds via a limiting **D** mechanism.[26] In contrast, the water exchange at Sc(III) center, with electronic configuration d^0, proceeds via limiting **A** mechanism which is clearly more favorable than the **D** mechanism, for which characteristic transititon structures were optimized as well.[37b] Square-planar Pt(II) and Pd(II) complexes, (electronic configuration d^8) are more likely to react via associative pathways because of coordination sphere is less congested to start with. The reactions with these complexes proceed via an **Ia** mechanism. The dissociative character of the water exchange mechanism for such complexes was assigned only in the cases when a strong σ-donor is present in *trans* position (CH_3^-).[27] The differences between the substitution mechanisms at Ru(II) as compared to Ru(III) are mainly due to the change of the occupancy of d orbitals, from d^5 to d^6. The gradual filling of the non-bonding t_{2g} orbitals, spread out between ligands disfavors electrostatically the approach of a seventh molecule towards a face of the octahedron emphasizing the dissociative character of the mechanism. The increase of the ionic radius enhances the dissociative character, as the leaving ligands are less strongly attached to the metal center, therefore easier dissociate.

Because the aquation of Ru(III) complexes proceeds only via an interchange mechanism with strong dissociative character, in the case of Ru(II) complexes a limiting **D** mechanism should be expected. Although the experiments do not exclude the possibility of an interchange mechanism, the computational attempts to find typical transition states for water exchange at Ru(II) in hexaaqua complexes failed in the previous studies.[42] In our attempts to find TS characteristic for an interchange mechanism only strongly stabilized by hydrogen bonding TSs involved in **7** and **8** aquation were optimized. The H(N1(1'):Hpz,Hind)–Cl contacts are 2.02 Å. Even in these cases the dissociative mechanism is preferred path of aquation showing a ΔG^a lower by ~4 kcal/mol (Table S5, Table S6 and Figure 4). This is the reason why we investigated only the **D** mechanism (Scheme 2) of the substitution at the metal center in Ru(II) complexes for all subsequent reactions. Figure 4 shows the energy profiles of Ru(II) aquation. The loss of chlorido ligand proceeds fast, the first step has low activation barriers of 9.5–12.9 kcal/mol. The resulting intermediates bind one water molecule in the second step of **D** mechanism, which is not the rate determining, the reactions being exergonic. Because aqua ligand has a week *trans* effect, higher activation barriers are expected for the first step of dissociative mechanism, therefore the formation of the *trans*-di-aqua isomer is kinetically less feasible. In contrast to Ru(III) species the

deprotonation of the aqua ligand is a thermodynamically less favorable process (Table S6, Figure 4).

Scheme 2. The dissociative (**D**) mechanism of Ru(II) aquation

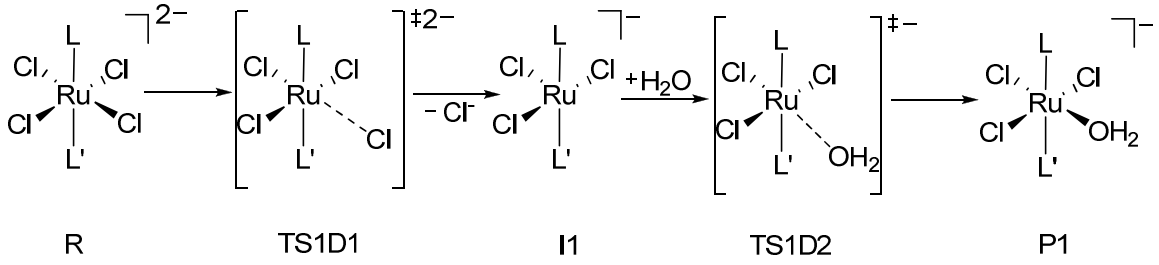

5: L = Im, L' = DMSO; **6**: L = L' = Im; **7**: L = L' = pz; **8**: L = L' = Ind

Figure 4. Free energy profile of the aquation of Ru(II) complexes. The solid lines represent **D** mechanism, while dotted lines are used for less favorable interchange mechanism of associative character. Free energies (kcal/mol) are calculated with respect to separated reactants. The digit following the transition states designator (TS) denotes the aquation step. The first and second steps of **D** mechanism are symbolized by **D1** and **D2** respectively.

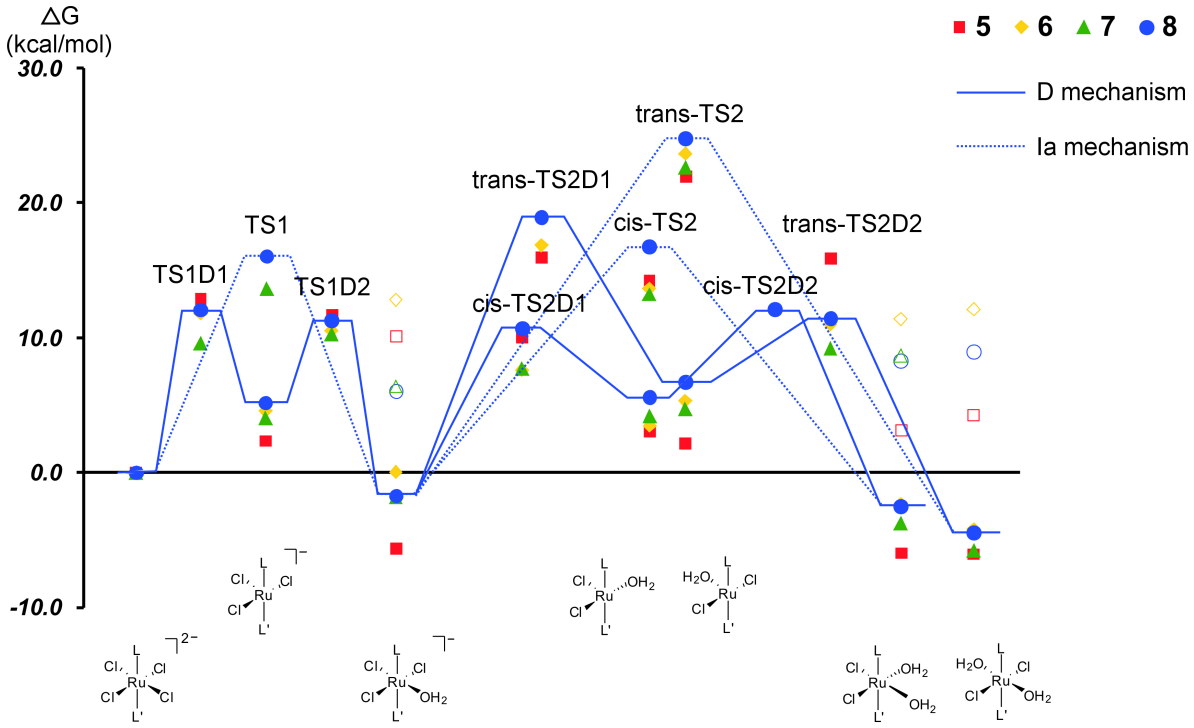

IV.4. Factors controlling the SRPs

The "activation by reduction" hypothesis ascribes to the reduction potential of the Ru(III) anticancer drugs a central role in their pharmacological activity. The SRPs of the chlorido prodrugs fall into the biological accessible range of –0.4 to 0.8 V.[43] The aquation and subsequent binding to a protein residue or a purine base change the redox potential, and implicitly influence the activity. The ultimate success of the Ru(III) anticancer drugs implies the possibility to rationalize the control of the redox potentials. So far, SRPs of the metal complexes were predicted using an empirical increment system[44] derived from experimentally measured SRPs. In this study we use a computational approach which was recently checked and validated[28] by predicting the SRPs of 61 ruthenium complexes. By performing computational prediction of the redox potentials we are interested in revealing the effect of the axial ligands, pH; substituted ligands, and environment on the redox behavior of Ru(III) compounds.

IV.4.1. Effect of axial ligands

To characterize the metal-axial ligands interaction in **1–8**, we have analyzed the molecules in terms of interactions between the two fragments: (i) the common for all four low spin $d^5(d^6)$ complexes fragment $[RuCl_4]^{-/2-}$, **f1**, and (ii) the fragment containing axial ligands, **f2**, using an energy decomposition scheme developed by Ziegler and Rauk[45] at the B3LYP level as implemented in ADF. The metal orbital interactions with axial ligands in *trans*-$[RuCl_4(Hpz)_2]^{-/2-}$ are displayed in Figure 5 and their energy contributions are collected in Table S7 in *Supporting Info*. The low symmetries of studied compounds (C_{2h} for bis-azole compounds (**2–4**) and C_s symmetry of NAMI-A (**1**)) do not allow the full analysis of metal orbital interaction with the axial ligands orbitals. To overcome this problem we studied the rotamers of the **2–4** compounds in the C_{2v} symmetry as well. To reveal the interaction of the metal with DMSO ligand we adopted a different approach: we have studied *trans*-$[RuCl_4(DMSO)_2]^{-/2-}$ complexes which have higher symmetry (**9** and **10** in Chart 2). The replacement of imidazole by DMSO increases the symmetry of the system, and the rotamers

of C_{2h} and C_{2v} symmetry become accessible. Either C_{2h} or C_{2v} symmetry itself is not enough to fully characterize the metal-ligand interactions, but their combination enables full description of the interaction systems with following approximations: there are negligible interactions between symmetry adapted axial ligands orbitals with $4d_{(x2-y2)}$ and $5p_x$ metal orbitals. Figure 6 displays an example of how to use the rotamers' approach to compute the stabilizing orbital energy component due to back-donation from the $4d_{xz}$ orbital to DMSO ligand. Table S7 in *Supporting Info* includes the formula used to calculate and the values of the interaction energies of the metal orbitals with the axial ligands. The results of the bonding analysis for **4**, **9** and their reduced species **8** and **10** are presented in Table 4 (Table S8 for **2,3** and **6,7**), which reports all contributions to the **f1–f2** interaction energy, and includes: repulsion between fragments due to Pauli principle ΔE_{Pauli}, electrostatics ΔE_{elst}, and stabilizing orbital interactions ΔE_{orb} ($\Delta E_{int} = \Delta E_{elst} + \Delta E_{Pauli} + \Delta E_{orb}$). The orbital energy component is further decomposed in contributions from irreducible representations of particular point group. Figure 7 displays the contribution from metal orbitals to the stabilizing orbital interactions in compounds **6–8**, and **10**. The orbital interaction is governed by a strong σ-donation from the ligands to the empty d_{z2} or 5s orbitals[46] of the ruthenium and π-back donation from d_{yz} (including d_{xz} in the case of DMSO) to the axial ligands. The interactions of metal $4d_{xy}$, $5p_z$, $5p_y$ and $5d_{xz}$ (in the case of bis-azole complexes) orbitals with the axial ligands are not accompanied by a charge transfer and have only a polarization character. Interestingly, the involvement of the empty metal p orbitals in the bonding at the transition metals, being controversially disputed in the literature,[47] is found to be strongly basis set dependent. Despite the quantitative improvements, in the terms of energy components, arisen by improving the quality of basis set from triple to quadruple zeta are negligible, the orbital interactions description is altered. The usage of triple zeta quality basis set predicts the participation to bonding of the metal p_z orbital by computing significant charge transfers to this orbital. However these interactions have only a polarization character when the enhanced basis of quadruple zeta quality is used (Table S9 and Table S10).

The large energy value of π-back donation from the d_{yz} in the case of **8** as compared to **7** is induced by the large negative charge of the complexes which is compensated by solvation (Figure 8). Computations on the neutral model complexes show similar stabilization due to π-back donation from d_{yz} (Table S11). Figure 8 displays the gas-phase change in the interaction energy between **f1** $[RuCl_4]^{-/2-}$ and axial ligands in **1–4** and **5–8**, together with their

difference in the gas-phase and in solution. The gas-phase differences predict a larger stabilization of **4** upon reduction in comparison to **1**. The measured SRPs sequence in solution is reproduced after the inclusion of solvation, which seems to be an important factor in stabilization of the reduced forms.

Figure 5. Interactions of metal orbitals with axial ligands in $[RuCl_4(Hpz)_2]^{-/2-}$

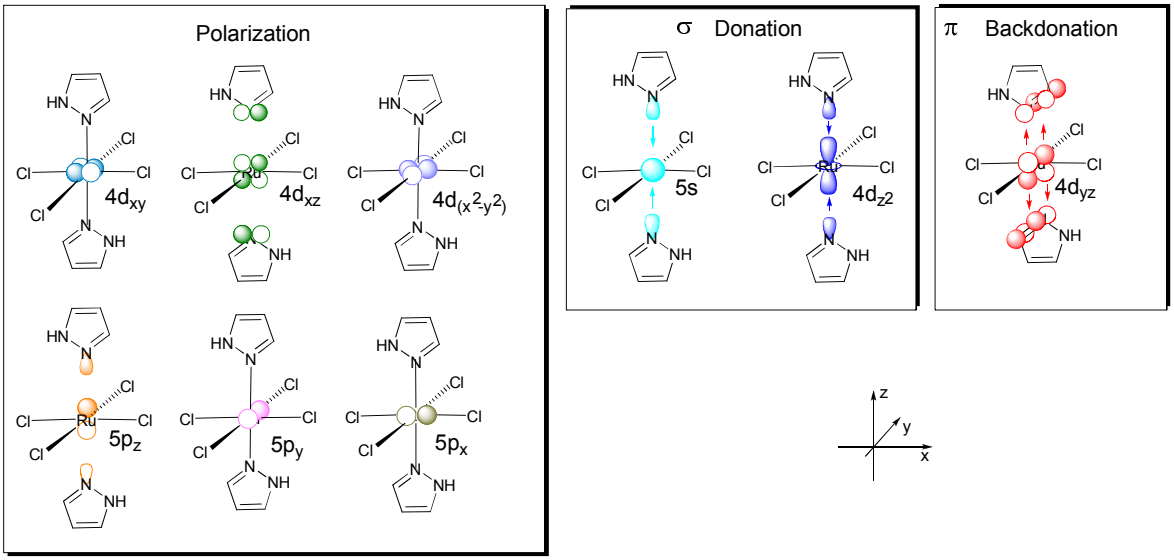

Figure 6. Usage of the rotamer's approach to evaluate the $4d_{xz}$ contribution to orbital interaction energy

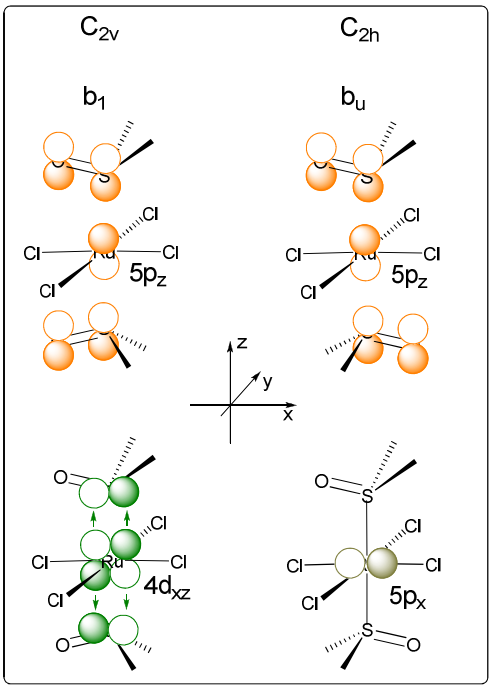

Formula

$5p_z = b_u$

$5p_x = 0$

$4d_{xz} = b_1 - b_u$

Table 4. Decomposition of the interaction energy between $[RuCl_4]^{-/2-}$ and the axial ligands in **9**, **4** and in their reduced forms **10** and **8** (kcal/mol)

	C_{2h}				C_{2v}			
	9	**10**	**4**	**8**	**9**	**10**	**4**	**8**
E_{int}	–70.7	–75.8	–89.3	–91.6	–70.8	–75.2	–88.7	–90.5
E_{solv}	–61.5	–185.1	–59.5	–178.1	–62.3	–186.5	–60.0	–179.2
$E_{int+solv}$	–132.2	–260.8	–148.8	–269.7	–133.1	–261.7	–148.7	–269.7
ΔE_{Pauli}	182.5	213.4	183.0	214.2	182.5	213.2	182.9	214.0
ΔE_{elst}	–148.0	–175.9	–172.9	–188.7	–147.7	–175.4	–173.0	–188.6
ΔE_{orb}	–105.2	–113.3	–99.4	–117.1	–105.5	–112.9	–98.6	–115.9
$\Delta E_{\Gamma i}$ C_{2h} (C_{2v})								
a_g (a_1)	–90.2	–93.2	–78.1	–76.0	–69.8	–61.4	–64.5	–58.2
b_g (a_2)	–27.0	–38.2	–26.1	–55.3	–23.1	–35.5	–20.9	–54.0
a_u (b_1)	–3.3	–5.1	–3.2	–5.8	–36.5	–48.6	–32.9	–37.1
b_u (b_2)	–16.5	–17.4	–20.1	–20.4	–7.8	–8.1	–8.5	–7.3

Figure 7. Contribution from metal orbitals to the stabilizing orbital interactions in compounds **6–8** and **10**

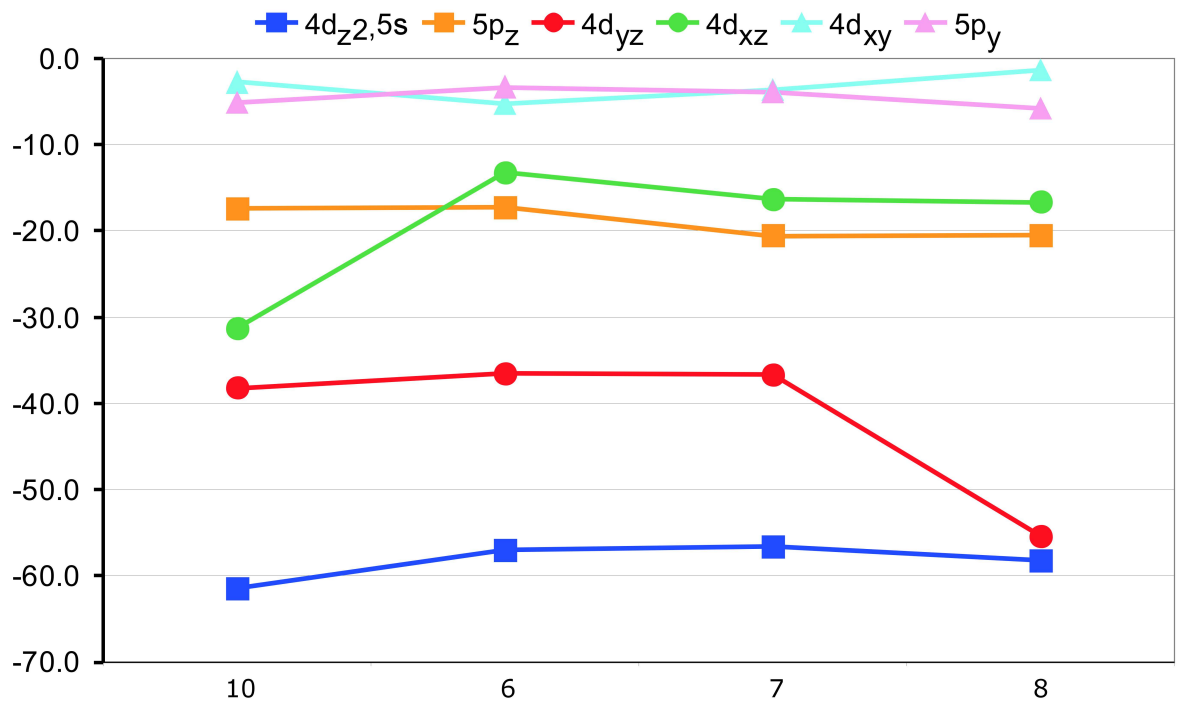

Figure 8. Total interaction energies ΔE_{int} between $RuCl_4^{2-/-}$ and the axial ligands in **1–4** and **5–8**, along with their interaction energy differences which determines the SRPs; in vacuo and in aqueous solution.

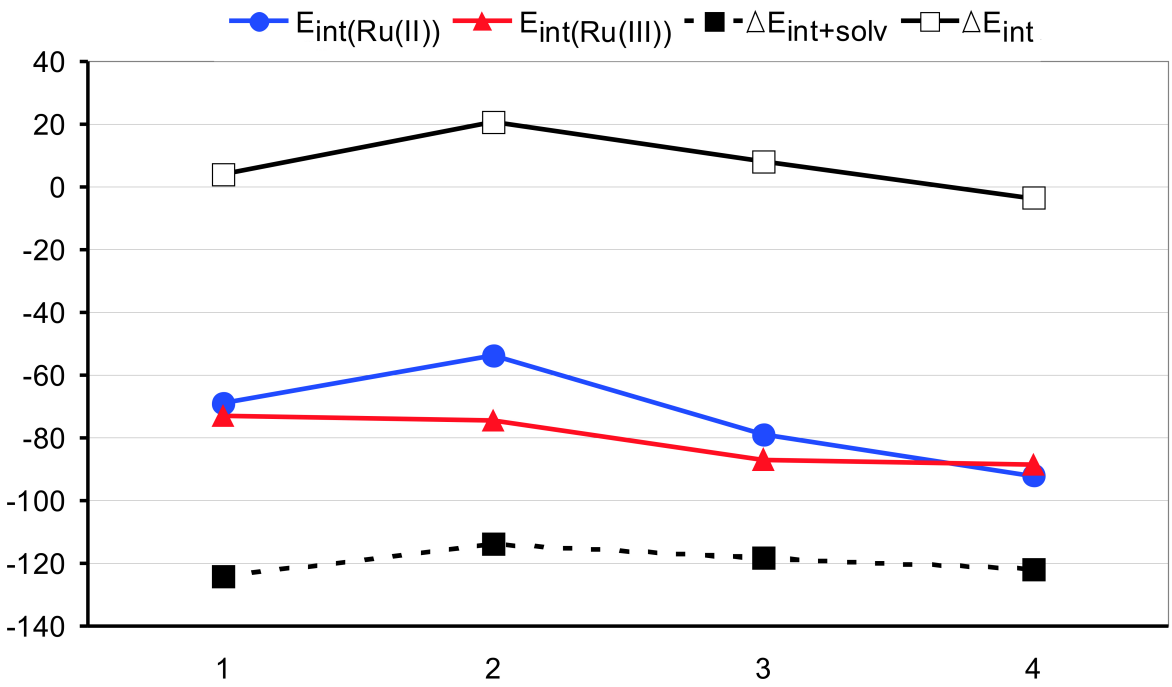

Figure 9 displays the change of the calculated SRPs as function of the substituted ligand at the metal center in the substituted complexes (**1–4)** (Chart 2). The first "evolution" step involves the exchange of the DMSO ligand in NAMI-A type compounds by an imidazole. The replacement is accompanied by a drastic decrease of the SRPs in the studied series by 355 mV in average. Strong π-backdonation found by the decomposition analysis from ruthenium $4d_{xz}$ and $4d_{yz}$ to DMSO ligand reveals its good π-electron acceptor character (Table 4) which stabilizes the reduced forms. The replacement of the axial imidazoles by pyrazoles increases the SRPs by 190 mV in average. The subsequent expanding of electron delocalization at axial ligands by fussion of benzo ring to each pyrazole is accompanied by a 137 mV average increase of the redox potentials of the KP1019 derivatives. This last step partially compensates the effect of DMSO removal, as the SRPs grow to be comparable to the SRPs of NAMI-A derivatives (Figure 9, Table S12). These changes are consistent with the variation of the donating properties of the free ligand series: imidazole (pK_a = 7.11) > pyrazole (pK_a = 2.64) > indazole (pK_a = 1.25),[48] i.e. the weaker donor character of the axial ligands is (lower pK_a value), the reduction is easier, stronger stabilization of the reduced forms is observed, and higher SRPs are expected (Figure 10).

Figure 9. Redox potential change upon substitution in **1–Y**:**4–Y** series. The red scale represents the biologically inaccessible redox-potentials

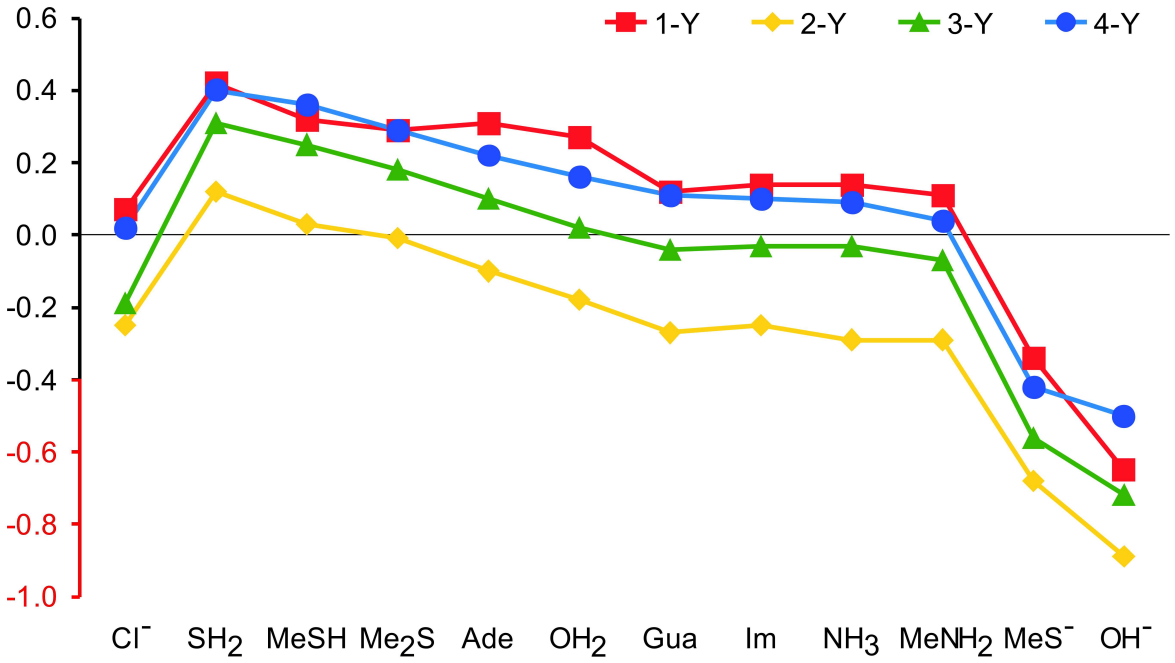

Figure 10.The easier reduction occurs at an electronically less crowded metal center

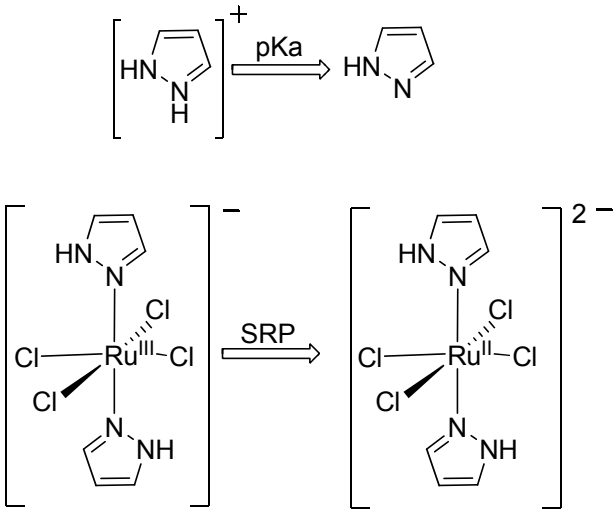

IV.4.2. Ligand effect

To investigate the effect of biologically relevant substituents at the metal center on the redox behavior of **1–4** in aqueous solution, we have calculated the SRPs at B3LYP level by including the effects of solvation by employing a continuous dielectric model with a dielectric constant ε = 80 for water (Figure 9). The derivatives of **1–4** are ordered by the experimental pK_a values of the substituted ligands in their free forms. A large change, 330 mV in average, of the reduction potential of the lead structures is observed when one chlorido is substituted by sulfur ligands. The binding to nitrogen sites of proteins and purine bases increases the SRPs by 180 and 140 mV in average. The largest positive effect on the SRPs in the nitrogen series is found for the adenine substituted complexes consistently with its lowest pK_a value in the nitrogen series: $AdeH^+$ ($pK_a < -2$) < $GuaH^+$ ($pK_a = 3.3$)[49] < ImH^+ ($pK_a = 7.1$) < NH_4^+ ($pK_a = 9.25$) < $MeNH_3^+$ ($pK_a = 10.6$). The coordination of anionic hydroxido (**OH^-**) and thiolato (**MeS^-**) ligands is accompanied by a SRP drop of 330 mV in average. Remarkably, the most successful drugs KP1019 (**4**, blue values) and NAMI-A (**1**, red values) are predicted to show generally the same redox behavior upon substitution (Figure 9). The donating properties of the free ligands influence the redox potentials of metal complexes. As mentioned in the previous section, the pK_a value is a good measure of these properties. The oxidized Ru(III) species are more strongly stabilized by the ligands whose conjugate acids have higher pK_a values making reduction more difficult to occur.

IV.4.3. pH effect

In vivo the control of the protonation state of a molecule is realized by medium acidity and the environment (dielectric constant of microenvironment, hydrophobicity, hydrophilicity, hydrogen bonding, etc.). Depending on the acidity constant of acidic sites of the molecule, the medium pH directly controls its protonation state and implicitly its SRP. We were interested at which extent an eventual deprotonation of the ligands influences the

SRPs of the studied compounds. For this reason one should evaluate the imminent shift of the pK_as of the free ligands upon coordination to the metal. The coordination to a positively charged metal ion results in an acidification of the acidic sites of the molecule. The extent of acidification depends on (i) the electronic effects exerted by the metal ion, which occur through bonds, as well as (ii) the long-range electrostatic repulsion between the proton under consideration and the positively charged metal ion.[49] The effect is strongest on the directly coordinated atoms and diminishes with distance increasing between acidic site and the metal. We calculated the pK_a values of the aquation products and thiol substitution products. The pK_a calculation method involves a thermodynamic cycle (see *Computational details*) which presents a maximum error of ~0.7 pK_a units when applied to free azoles (Table S13) and was found to be very accurate in the prediction of relative pK_a trend[16e] of metal complexes, with the absolute error of up to 4 kcal/mol. Table 3 summarizes calculated pK_a values of Ru(III/II) aqua and thiol complexes. Once coordinated, the pK_a of water molecule drops dramatically from 15.75 in its free state to 2–4 pK_a units in mono-aqua Ru(III) compounds. The formation of hydroxido complexes was observed experimentally by measuring the pH drop during aquation studies.[50] The coordination of methylthiol (pK_a = 10.4) to Ru(III) is accompanied by strong acidification of sulfhydryl group (–SH) reflected by negative computed pK_a values (Table 3).[51] The aquation promotes reduction as the aqua complexes slightly increase the redox potentials of the parent chlorido prodrugs making the reduction easier, on the other hand the formation of hydroxido species impedes the reduction, as the redox potentials of all 4 hydroxido-complexes fall outside the biological relevant window (Figure 9, Table S12). The same is true for the coordinated thiols whose SRPs drop significantly upon deprotonation by 740 mV in average. The pK_a values of water and thiols coordinated to Ru(II) species are all calculated to be > 10 suggesting a strong stabilization of protonated species upon reduction.

IV.4.4. Environmental effect

To consider the effect of the environment on the redox properties of the studied compounds, we have computed SRP values at a lower dielectric constant characteristic for protein environment. Depending on whether the site of interest is located on the protein surface, solvent-exposed, or deeply buried into protein, medium ε might be as low as 3, and

typically lower than 10,[52] while ε of DNA in aqueous solution was estimated to be 24.[53] We have chosen the value of ε = 10, to reveal the influence of low dielectric constant on the redox potential. The computed SRPs of complexes **1–4** and their monosubstituted derivatives drop significantly with 270 mV in average. The most affected are highly charged compounds (the prodrugs (tetrachlorido complexes), thiolato and hydroxido complexes), the SRPs of which fall by 550 mV in average (Table S14 in *Supporting Info*). The same behavior was observed experimentally by measuring the SRP of ruthenium anticancer agents in different solvents.[54] The influence of dielectric constant on the solvation energy is explained by considering a simple Born model[55] of solvation, that states that the free energy of solvation is equal to the work spent to transfer the ion in a spherical cavity from vacuum (ε = 1) to a medium with a dielectric constant of ε (ΔG_{solv} proportional to $-(1 - \varepsilon^{-1})q^2r^{-1}$). The decrease of ε from 80 to 10 is accompanied by decrease of solvation energy. The strongest effect being supported by highly charged species, i.e. by Ru(II) species, that results in lower SRP values.

IV.5. Reactivity towards biomolecules

The binding towards relevant biomolecules in aqueous solution was investigated by computing characteristic activation and reaction free energies of the reactions of mono-aqua ruthenium species with a choice of nucleophiles (Chart 2). In this sense the optimization of all involved species, i.e. transition states and reaction products, was performed. Similarly to the computations on cisplatin, the reactivity of Ru(III) complexes was investigated in terms of the exchange of the aqua ligand with all model ligands (**Y**) presented in Chart 2, by exploring the free energy profiles of the substitution mechanism of interchange character:

$$RuCl_3LL'(H_2O) + Y \rightarrow [H_2O\cdots RuCl_3LL'\cdots Y]^{\ddagger} \rightarrow RuCl_3LL'(Y) + H_2O$$

Figure 11 displays at a glance the predicted activation and free energies of these reactions.The mechanism of binding to Ru(II) analogs of anticancer complexes was investigated in the terms of **D** mechanism as was found that Cl dissociation proceeds very fast after reduction, and is the rate limiting step for the aquation. The available *in vivo* biological targets compete with water molecule to bind the intermediate formed after the first step of the **D** mechanism. Therefore only the free energy profiles of the second step of **D** mechanism were computed:

$$[RuCl_3LL']^- + Y \rightarrow [RuCl_3LL'\cdots Y]^{\ddagger -} \rightarrow [RuCl_3LL'(Y)]^-$$

Figure 12 displays the activation and reaction free energies of substitution process of protein and DNA models at Ru(II) centers. The transition states correspond to the second step of the dissociative mechanism with reference to mono-aqua species of **5–8**.

Figure 11. Predicted activation ΔG_a (top) and reaction free energies ΔG_r (bottom) of the aqua substitution in **1–OH$_2$**:**4–OH$_2$** by **Y** (Chart 2). **Gua*** - guanine substitution at *cis*-di-aqua complexes of **1–4**.

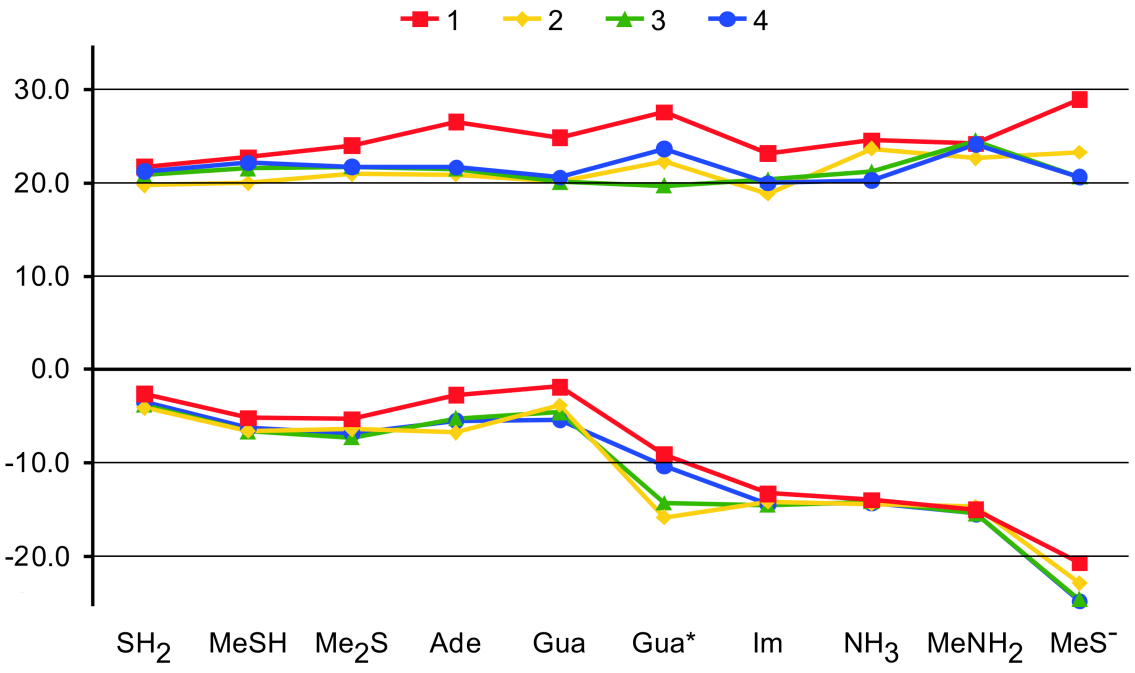

Figure 12. Predicted activation ΔG_a (top) and reaction free energies ΔG_r (bottom) of the binding of Ru(II) (**5–OH_2**:**8–OH_2**) complexes to biological models **Y** (Chart 2). **Gua*** - guanine substitution in *cis* position of di-aqua complexes.

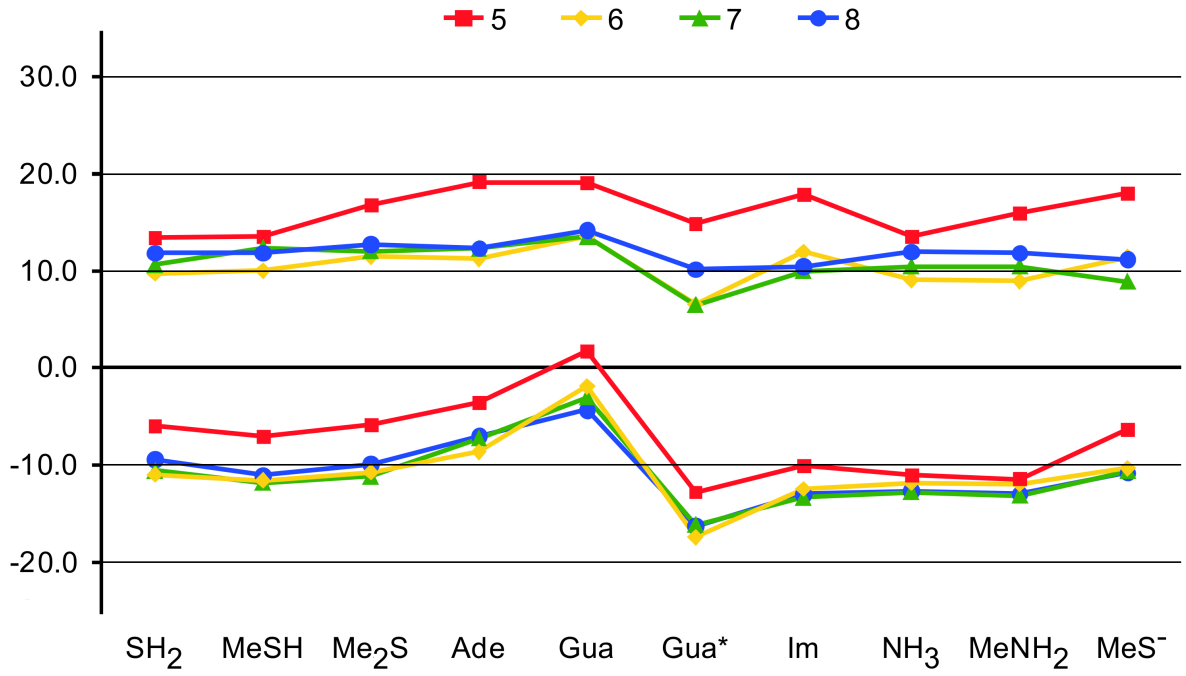

IV.5.1. Reactions with proteins

Kinetically the Ru(III) species do not have a clear kinetic preference for either nitrogen or sulfur ligands (Figure 11, Table S15). Although the reaction with imidazole (**Im**), representing histidine, is slightly preferred (ΔGa is lower by 1–2 kcal/mol than corresponding ΔGa of the reactions with **MeSH** and **Me_2S**) the activation energy of the Ru(III) complexes binding to **$MeNH_2$** is higher by 3–4 kcal/mol than the activation energies of the reaction with all sulfur containing models. The highest activation energies were found for the aqua ligand substitution at **1–OH_2**. This may be due to steric repulsions between bulky DMSO moiety and the entering ligands. The substitution proceeds via an interchange mechanism with strong dissociative character (Table S17). The Ru(II) species do not show either a clear preference for sulfur or nitrogen containing protein models. (Figure 12, Table S16). Generally, the loss of Cl ligand in the first step of the **D** mechanism is the rate determinant for the aquation; further binding to proteins or water molecules having similar activation energies. Thermodynamically the nitrogen containing protein sites are more favorable for the

substitution at ruthenium center in both oxidation states. The exception is the enhanced preference of Ru(III) centers for the deprotonated thiol ligand (**MeS**$^{-}$) reflected in the largest negative reaction free energies with thiolates. In the case of reduced species a clear stabilization of substitution products of protein binding as compared to the aquation products is observed.

IV.5.2. Reactions with DNA

The interaction with DNA was modeled as binding of the metal to free N7 sites of purine bases: adenine (**Ade**) and guanine (**Gua**). While Ru(III) compounds kinetically slightly prefer the guanine over adenine for binding (ΔG_a is up to 2.9 kcal/mol lower in the case of **1** (Table S15)), their reduced forms prefer adenine (ΔG_a is up to 2.2 kcal/mol lower in the case of reduced ICR (**6**)); the exception is the similar activation energies of **5** binding to both purine bases. Thermodynamically the interaction with **Ade** and **Gua** is less favorable than interaction with proteins.

The intriguing finding is that, contrary to cisplatin, the ruthenium anticancer drugs virtually do not have any clear preference for either purine bases. The presence of a hydrogen bond between the O6 of **Gua** and the aqua or ammine ligand determines mainly the preference for **Gua** binding of cisplatin.[17] In the case of ruthenium anticancer compounds such stabilization can occur only if the active species is considered to be the *cis* product of second aquation step. To verify the influence of the hydrogen bonding on the energy profile we optimized the TSs and the products for the reaction of investigated *cis*-di-aqua ruthenium compounds with **Gua** paying particular attention to the presence of the hydrogen bonding between O6 of **Gua** and the aqua ligand bound to the metal. The kinetics of the interaction between Ru(III) complexes with DNA does not change (Figure 11); contrary to the substitution kinetics of reduced species (Figure 12). In this case the transition states are stabilized by up to 7 kcal/mol (Table S16). The **Gua** becomes the preferred binding site for Ru(II) species (Figure 12), and more favorable than sulfur protein sites for Ru(III) species, except thiolates. Figure 13 shows characteristic geometries of the transition structures for **Gua** substitution at Ru(II) centers. The presence of hydrogen bonding between guanine N7 and N1 of pyrazole stabilizes the entering ligand in an orientation that is energetically

disfavored for complexation (with the N7 lone pair perpendicular to Ru–N bond in formation). This arrangement requires additional energy to reorient the molecule in a position suitable for binding to the metal. This barrier is canceled in the binding to di-aqua complexes, as the N7 lone pair shows appropriate orientation towards the metal. In addition, the stabilization due to the hydrogen bonding between guanine O6 and the aqua ligand in *cis* position (Figure 13) contributes as well to lowering the activation energies. Although the similar geometric changes in the transition structures are observed in the case of substitution at Ru(III) centers, the activation barriers are predicted to be higher.

Figure 13. Typical hydrogen bonding pattern in Gua substitution at **7** and **7–OH_2** in *cis* position

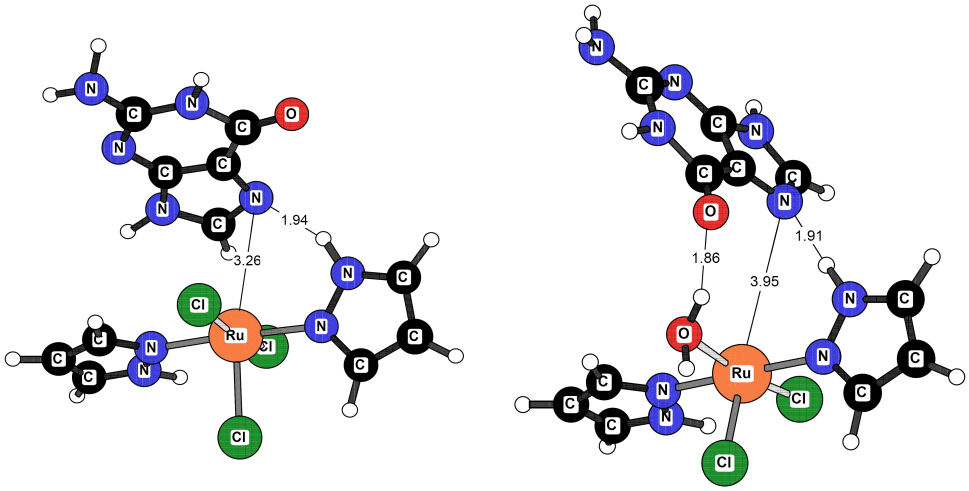

IV.6. Mode of action

Based on our computed data and experimental findings, the mode of action of Ru(III) anticancer drugs may be divided into two steps. The first step describes the chemical behavior of the drugs prior and post administration, before reaching the cancer cells; the second step includes the chemical transformations of the complexes in the tumors. The aquation is an important process in both steps, firstly because it influences directly the pre-administration storage of the chlorido complexes, and secondly because water molecules are most abundant binding partners *in vivo* and are essential for the metallo-drug activity, as aqua species are orders of magnitude more labile than the corresponding chlorido species.

Although the aquation process of ICR and KP1019 is slow at 25° C,[40b] and complexes remain in their inert form, under physiological conditions (37°C, pH 7.4) one chlorido ligand is displaced by a water molecule, as has been confirmed in X-ray diffraction studies of a number of aqua complexes.[24,56] The parent Ru(III) complexes enter the blood stream where they are the subject of aquation. The process is slow characterized by high activation barriers (Table 2); the experimental rate constants are comparable with those of cisplatin.[57] The aquation of the second chlorido ligand is both kinetically and thermodynamically less feasible process and *cis*-di-aquated products can be formed only in trace quantities. The water molecule in mono-aqua species is replaced by available biological partners. Experimentally was found that KP1019 binds to transferrin within minutes,[58] and the highest affinity sites are the iron specific binding sites (His253) in human apo-lactoferrin, which is structurally similar to human transferrin and shares 60–80% of sequence identity.[59] Despite the fact that there is not a clear kinetic preference for the binding to nitrogen or sulfur protein sites (the substitution at histidine protein residues being only slightly favorable) the thermodynamics favors relatively strong binding to the nitrogen protein sites, at the same time the binding to sulfur groups being reversible process. Similarly to cisplatin, the cysteine binding, followed by the deprotonation of –SH group of the substituted complex, contributes to the deactivation pathway, as the thiolates bind irreversibly. Once bound to transferrin the drug is selectively delivered to and accumulated in the tumor cells, which have a large number of transferrin receptors on their surface due to high iron requirement.[60] The release of the bound drug can be achieved due to the lower pH characteristic of endosomes.[12] After the release, the Ru(III) complexes can bind to the cellular proteins and DNA, inducing apoptosis. The second step aquation products are more likely to be formed inside the cells due to low concentration of the Cl^- ions. The rate of binding to cellular components is enhanced by reduction. The calculations show that all parent complexes have biologically accessible reduction potentials; moreover the aquation facilitates the process. Low extracellular pH and large amounts of cellular reducing agents (e.g. glutathione, $E^{0'}$ = –0.25 V;[61] ascorbic acid, $E^{0'}$ = 0.06 V[62]) in cancer cells form the reductive environment in the tumor compared to the normal tissue, thus determining the selective reduction in cancer cells. In contrast to the slow substitutions at Ru(III) centers, the reduced species are characterized by the fast ligand substitution reactions. Significantly lower computed activation barriers for the substitution at Ru(II) mean these compounds are much more reactive, than their oxidized forms, the fact observed experimentally.[5] In parallel to substitution reactions at Ru(II) centers the back auto-oxidation process can occur as well, the phenomenon revealed experimentally during the study of NAMI-A chemical behavior in

aqueous solution,[6b] when in the presence of catalytic amount of reducing agents, the rate of aquation of Ru(III) complex significantly increased. The aquation is fast,[63] and goes up to the second step, the kinetically favorable *cis*-di-aqua products are the most abundant species. The fast release of one ligand, characteristic for **D** mechanism in the first step, offers a free coordination site available for the substitution, and ruthenium compounds bind reversibly to biological targets without clear preference. We computed the reaction energy profiles for the first ligand substitution with the biological models, and believe that the substitution at di-aqua species should present similar barriers. One exception is the binding of guanine model, which may show a distinct hydrogen bonding pattern in both transition state and in products. As a result, the calculations reveal a clear kinetic and thermodynamic preference for guanine over adenine in the binding to DNA. In contrast to cisplatin, the formation of interstrand cross-links was assumed.[64] Although not excluded, the binding to DNA alone as the main reason for the anticancer effect of ruthenium drugs is still widely doubted.[3,8c] Figure 14 shows the energetic profile of the chemical transformations for KP1019.

Figure 14.Free energy profiles for chemical transformations of KP1019 in aqueous solution at physiological conditions

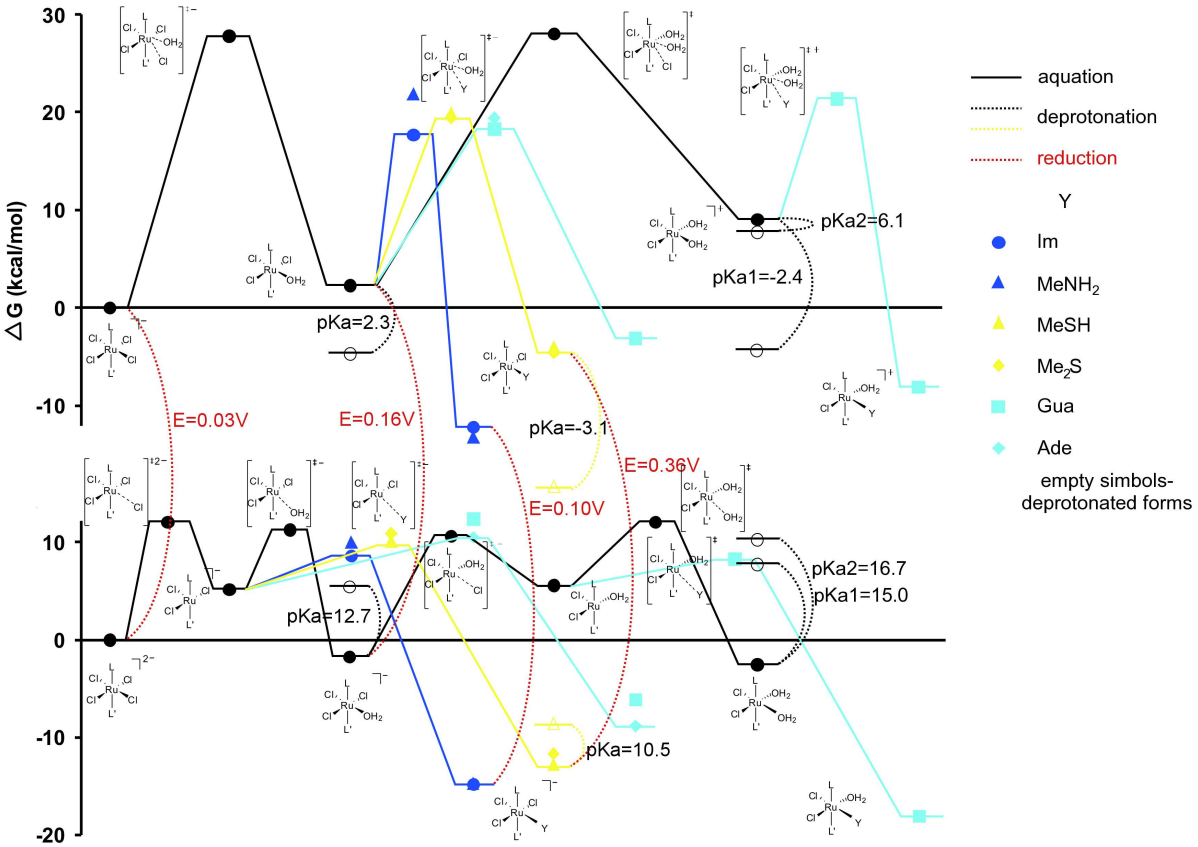

The reduced ruthenium compounds can be oxidized back by cellular oxidants such as superoxide radical (eq. 1, E = 0.94 V)[65] or by hydrogen peroxide (eq. 2, E = 0.38 V),[65] which are normal metabolites in the aerobic cells:

$$O_2^- + 2H^+ + e \rightarrow H_2O_2 \quad (1)$$

$$H_2O_2 + e \rightarrow OH^\bullet + OH^- \quad (2)$$

Superoxide anion is produced *in vivo* as a byproduct of mitochondrial respiration, as well as by several other enzymes, for example xanthine oxidase or NADPH oxidase. Its cell concentration is maintained at 10^{-12} – 10^{-11} M by superoxide dismutase.[66] Mitochondria, microsomes, peroxisomes, and cytosolic enzymes have all been recognized as effective H_2O_2 generators, the level of H_2O_2 inside the cell is up to 3 – 4 orders of magnitude greater than of O_2^-, 10^{-9} – 10^{-7} M. Experimentally findings that *in vitro* overproduction of hydrogen peroxide is a constitutive characteristic of cancer cells (the concentration of H_2O_2 reaches millimolar range)[67] suggest that H_2O_2 might play an important role in the reoxidation of Ru(II) complexes in hypoxic conditions in tumors. High concentration of hydrogen peroxide is cytotoxic. It is therefore widely thought that H_2O_2 is very toxic *in vivo* and must be rapidly eliminated by enzymes such as catalases, peroxidases and thioredoxin-linked systems. However, H_2O_2 is poorly reactive: it can act as a mild oxidizing or as a mild reducing agent, but it does not oxidize most biological molecules readily, including lipids, DNA and proteins.[68] The danger of H_2O_2 largely comes from its ready conversion to the indiscriminately reactive hydroxyl radical, either by exposure to ultraviolet light or by interaction with a range of transition metal ions. Living organisms have evolved mechanisms to sequester transition metal ions into protein-bound forms that cannot catalyze hydroxyl radical formation and other free radical reactions *in vivo*. These mechanisms are especially important in such extracellular fluids as the blood plasma. The hydroxyl radicals formed can damage proteins, cell walls, and DNA, inducing apoptosis.

The transition metal oxidation by hydrogen peroxide is the long time studied process that makes the subject of so called Fenton's chemistry.[69] Two factors should be considered for a metal complex to act as a Fenton reagent:[70] i) the availability of a free coordination site

or the possibility of replacement of one ligand by H_2O_2, through which the peroxide is activated; and ii) the suitable reduction potential for the redox couple. Ru(II) complexes generated inside the cells fulfill these requirements and might operate as catalyst in Fenton type reactions. The intermediates produced during reversible processes of aquation or substitution at the metal center have a free coordination site available for binding of one hydrogen peroxide molecule, in this way generating the activation complex (eq. 3):

$$\left[Ru^{2+}\right] + H_2O_2 \rightarrow \left[Ru^{2+}\right] - H_2O_2 \rightarrow \left[Ru^{3+}\right] + OH^- + OH^{\bullet} \qquad (3)$$

Additionally, the accessible redox potentials of free and bound ruthenium make the redox cycling possible and likely to occur. We believe that the redox cycling of ruthenium species inside the cells, that generates continuously reactive hydroxyl radicals, can contribute to the ruthenium drugs cytotoxic effects. Indeed, the lower cytotoxic effect of ICR as comparing to KP1019 or NAMI-A,[71] can be in part attributed to lower redox potential of ICR that makes the reduction, and implicitly the redox cycling, more difficult to occur.

Recently, the catalytic behavior of organometalic Ru(II) "piano-stool" complexes ([(η^6-arene)Ru(azpy)I]$^+$, arene = *p*-cymene or biphenyl, azpy = *N*,*N*-dimethylphenyl or hydroxyphenyl-azopyridine) in the oxidation of the major intracellular reducing agent glutathione to glutathione disulfide was reported.[72] In this case, a ligand centered redox cycling was assumed to be responsible for the generation and accumulation of reactive oxygen species. Because the free azopyridine ligands are not readily reduced *in vivo*, the complexation is needed to raise the redox potential to become biologically accessible. A similar fine tuning of SRP of redox innocent ligands by metalation is described in chapter V of this thesis.

Figure 15. Mode of action of ruthenium anticancer agents

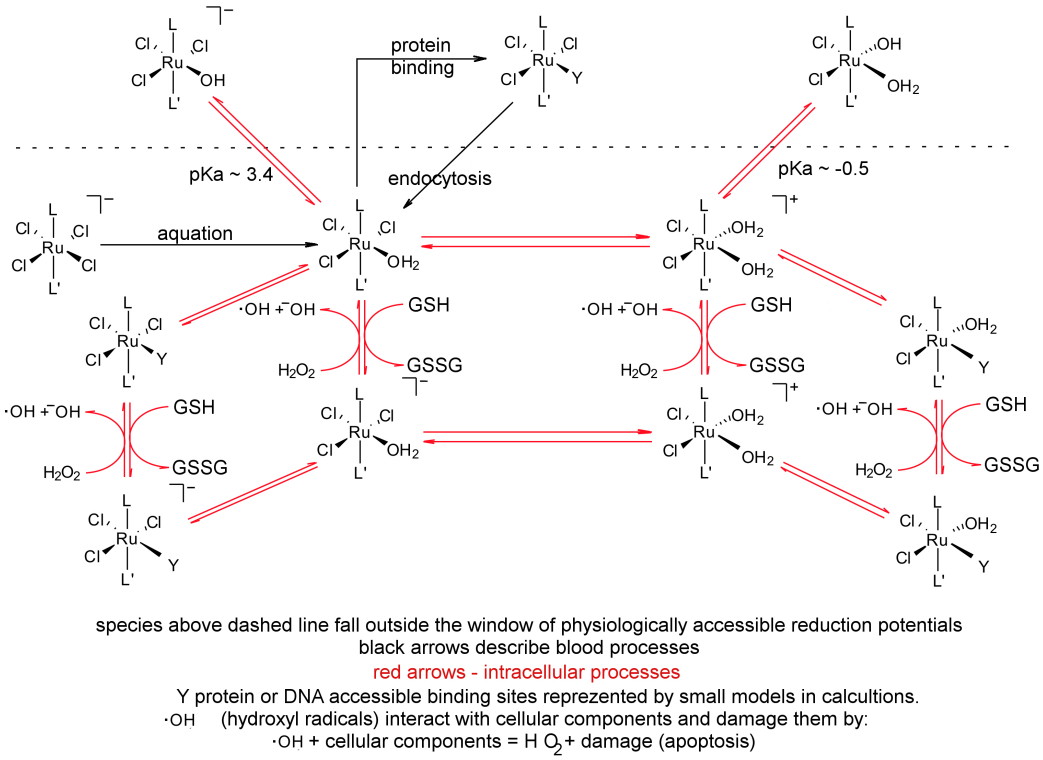

IV.7. Conclusions

In this work, by using high level quantum chemical calculations, we have investigated chemical aspects of the anticancer activity of four potent Ru(III) anticancer complexes: NAMI-A, ICR, *trans*-tetrachloridobis(pyrazole)ruthenate(III) and KP1019 (**1–4**, Chart 2). The computational setup was tested in advance and gives the best performance in computation of reduction potentials of Ru(III) complexes. The experimental aquation rates are predicted within one order of magnitude accuracy. Because of the biologically accessible reduction potential of these complexes, the description of their mode of action is more challenging than the computational investigation of the most known anticancer compound cisplatin. Moreover, since the first time the "activation by reduction" hypothesis was formulated some 30 years ago,[13] the reduction is supposed to be the major factor determining the anticancer behavior of Ru(III) complexes. The reduction, as important aspect of the activity, is taken into account, in addition, the electronic aspects governing the

electrochemical behavior of the Ru(III) complexes were revealed. The analysis of computed data shows interesting features of Ru(III) anticancer activity and can be summarized as follows:

1. Under normal conditions a slow aquation of one chlorido ligand takes place leading to mono-aqua species of Ru(III) complexes. The second step aquation is possible, but the di-aqua complexes are computed to be thermodynamically unstable, combined with high activation barriers of second aquation step, these species are less likely to form. The reduction promotes aquation which, following a dissociative mechanism, proceeds much faster than the aquation at more inert Ru(III) centers, and the process is exergonic except for **6** (reduced ICR). The few orders of magnitude faster kinetics favors the formation of the *cis* over *trans* isomer of di-aqua complexes, therefore the most abundant Ru(II) metabolites are likely to be mono-aqua and the *cis*-di-aqua complexes. At this point, the calculations reveal the relevance of the oxidation state for the aquation, and implicitly for the reactivity of Ru(III) anticancer agents.

2. We have investigated four major factors influencing the redox potential of the Ru(III) complexes: (i) the nature of the axial ligands at octahedral metal centers of initial prodrugs; (ii) the binding to biological targets; (iii) the influence of the medium pH; and (iv) the influence of the environment dielectric constant. The energy decomposition analysis clearly reveals the decisive role of π-electron acceptor character of DMSO land indazole igands in stabilization of Ru(II) species, promoting NAMI-A and KP1019 reduction. The successive change of the electron acceptor character from DMSO to imidazole through indazole and pyrazole correlates well with the reduction potential order of the original Ru(III) compounds. The solvation is an important factor determining the redox potential, as it compensates the effect of large negative charges on the π-back donation from the metal to bulky ligands such as indazole (Figure 8). The change of reduction potential after the binding to biologically relevant targets is directly related to the pK_a values of the free protonated ligands. A higher pK_a correlates with a more difficult reduction. The milieu acidity influences the protonation state of the ligands and consequently the reduction potential. The low dielectric constant of the medium impedes the reduction, as the SRPs fall dramatically with the decrease of ε. A smart tuning of the reduction potential by changing the axial ligands is a necessary condition in the rational design of the future Ru(III) anticancer complexes. The reduced ruthenium complexes may enter the redox cycling being oxidizing back by hydrogen

peroxide. The cycling may act as a continuous generator of reactive hydroxyl radicals, which damage the cells.

3. The interaction with biological targets was investigated by computing the activation barriers and reaction free energies of the aqua ligand substitution with a set of biological models representing N- and S- sites of proteins, along with adenine and guanine as purine DNA bases models. The aquation takes place prior to binding to biomodels and determines the rate of substitution. Similarly to cisplatin the substitution occurs at the more labile aqua ligands of the Ru(III) species. Despite the prediction that there is not a clear kinetic preference for the binding to nitrogen or sulfur protein sites (the substitution at histidine protein residues being only slightly favorable) the thermodynamics favors relatively strong binding to the nitrogen protein sites, which are computed to be ~10 kcal/mol more stable than the sulfur containing ligands. The exception being the thiolates which stabilize the Ru(III) compounds by up to 25 kcal/mol. NAMI-A is found to be overall less disposed to the substitution in both the kinetic and thermodynamic sense. After reduction, the Ru(II) species become much more reactive showing low activation barriers and large reaction free energies characteristic for all binding sites. However, a slight thermodynamic preference for N-containing ligands is revealed. The fact that the ruthenium species are not selective towards the purine bases of DNA suggests the mechanism of action other than that of cisplatin, which binds preferentially to the guanine sites of DNA. The exception is the *cis*-di-aqua species which prefer to bind guanine N7 site. Similarly to cisplatin the hydrogen bond from one aqua ligand in the mono-aqua substituted species to O6 of guanine stabilizes the transition states and the reaction products. This preference could play a significant role for the reactivity of the reduced species.

IV.8. Computational details

The structure optimizations were carried out using the 3-parameter fit of exchange and correlation functionals of Becke[73] (B3LYP), which includes the correlation functional of Lee, Yang, and Parr (LYP),[74] as implemented in Gaussian 03.[75] The Stuttgart-Dresden (MWB28) effective core potentials (ECPs)[76] and the corresponding valence-basis sets were used on ruthenium and the 6–31G(d,p) basis sets on the other atoms.[77] Vibrational frequencies calculated at this level confirm that all structures are either minima (NIMAG = 0)

or first order saddle points (NIMAG = 1) on the potential energy surfaces. Improved energies were calculated at B3LYP level by augmenting the metal basis set with two sets of f and one set of g functions[78] together with the same ECPs, the 6–311+G(3d) basis set on the S and Cl atoms, and the 6–311+G(d,p) basis sets on the other atoms. Free energies *in vacuo* were calculated by adding corrections from unscaled zero-point energy (ZPE), thermal energy, work, and entropy evaluated at the B3LYP level at 298.15 K, 1 atm to the improved energies.

Solvation free energies of the optimized structures were computed by means of Poisson-Boltzmann finite element method[79] as implemented in Jaguar 7[80] with the dielectric constant being 80.37 representing water as the solvent. This solvation model, in combination with above described gas-phase optimization protocol, gives the best performance in the SRPs computations, as shown in our previous benchmarking work.[28] We found an overall error of 0.03 V in the computations of 80 SRPs of 61 ruthenium (III) complexes bearing a wide range of molecular charges (from –1 to +3) in four different solvents. We have shown that the solute cavity choice is crucial in these computations; the performance of the model being strongly related to the solute cavity size in the solvent continuum. Because the metal is well buried into the octahedral surrounding of ligands, its radius does not influence the cavity size and implicitly the solvation energies. On the other hand the metal becomes exposed to the solvent as the nucleophilic substitution advances, and its radius might influence directly the activation free energies. The solvation energies of the penta-coordinated intermediates of the dissociative mechanism suffer mostly from the inaccuracy of the metal radius used. We adjusted the Ru(II) van der Waals radii used to build the solute cavity in Jaguar to fit best the experimentally available activation energies of water exchange in $[Ru(H_2O)_6]^{2+}$ and in $[Ru(NH_3)_5(H_2O)]^{2+}$ by pyridine and acetonitrile (details are available in S*upporting Info* Table S19). For consistency, the fitted value (2.08 Å) for Ru(II) atoms was used in solvation calculations. All free energies in solution were modified by an entropic term that is half of the entropy in vacuo, with the opposite sign, because the continuum dielectric models do not consider properly the changes of solvation entropy in bimolecular reactions. According to Wertz and others,[81] various molecules lose a constant fraction (approximately 0.5) of their entropy, when they are dissolved in water.

Because the aquation reaction is bimolecular the rate constant *k* computed by the use of Eyring equation (eq. 4) employing the predicted activation free energies contains the factor arisen from water concentration in the medium (55.5M).

$$-k = \frac{k_B T}{h} e^{-\frac{\Delta G_a}{RT}} \quad (4)$$

where k_B is the Boltzmann constant, T is the absolute temperature, and h is the Planck constant. ΔG_a is the activation free energy.

pK_a predictions were carried out using the thermodynamic cycle[82] displayed in Figure 16.

Figure 16. Thermodynamic cycle to predict acidity constants

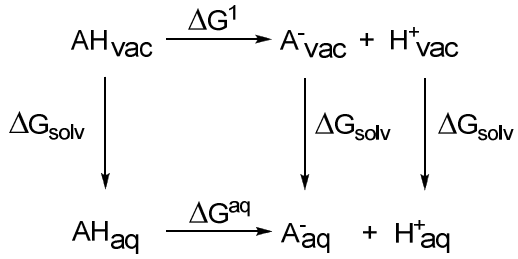

$$pK_a = \Delta G^{aq} / RT \ln 10$$

$$\Delta G^{aq} = \Delta G^1 + \Delta G_{solv}(H^+) + \Delta G_{solv}(A^-) - \Delta G_{solv}(AH)$$

where ΔG^1 is the reaction free energy of AH deprotonation in gas-phase; ΔG^{aq} is the reaction free energy in water; ΔG_{solv} are solvation energies of each species involved in the process. R is the ideal gas constant, and T is the temperature (298.15 K). We have used the values $G_{vac}(H^+)$ = –6.28 kcal/mol[83] and $\Delta G_{solv}(H^+)$ = –263.98 kcal/mol extrapolated from cluster ion solvation data.[84]

Standard redox potentials were calculated on the basis of the thermodynamic cycle similar to the one used for the prediction of acidity constants. The SRP is related to the reaction free energy of electron attachment process: Ox $+e^- \rightarrow$ Red in water (ΔG^{aq}) by:

$$SRP = -(\Delta G^{aq}/zF) - \Delta SRP_{NHE}$$

$$\text{with } \Delta G^{aq} = -\Delta G_{solv}(Ox) + \Delta G^1 + \Delta G_{solv}(Red)$$

ΔG^1 is the reaction free energy in vacuo, ΔG_{solv}(Ox) and ΔG_{solv}(Red) are the solvation free energies of the oxidized and reduced form, F = 96,485 C/mol = 23.061 kcal/(Vmol) is the Faraday constant, and z = 1 for one-electron reductions. The SRPs are shifted by ΔSRP_{NHE} = 4.28 V to align the results to the scale of the Normal Hydrogen Electrode (NHE).[85]

The chemical intuitive energy decomposition analysis as implemented in the Amsterdam Density Functional 2007 programs package (ADF)[86] was successfully applied in the similar computations on the nature of bonding in ruthenium complexes of the formula $[Ru(NH_3)_5B]^{Z+}$ (Z = 2,3), where B is a nucleobase or a protein model.[20] We performed the single point calculations on **1–10** at the B3LYP/ZORA[87] level using the large QZV4P basis set at ruthenium and the other atoms.

IV.9. Supporting Information

Table S1. Geometrical parameters used for the hydrolysis mechanism assessment

	M–Cl(O)						M–OH_2								Experimental activation parameters		
	R	RA (L)	RA (E)	TS	Δ(R)	Σ_{RA}	P	PA(E)	PA(L)	TS	Δ(P)	Σ_{TS}	Σ_{TS}–Σ_{RA}	ref	ΔH	ΔS	ref
	Å	Å	Å	Å	Å	Å	Å	Å	Å	Å	Å	Å	Å		kJ/mol	J/mol×K	
Cisplatin	2.370	2.383	3.610	2.742	0.37	5.99	2.087	2.03	3.953	2.401	0.31	5.14	–0.85	16a	19.67	–15	29
	2.390	2.399	3.667	2.819	0.43	6.07		2.042	4.135	2.42		5.24	–0.83	16a*			
		2.277	3.183	2.693		5.46		2.027	3.885	2.344		5.04	–0.42	30			
		2.361	3.862	2.798		6.22		2.082	4.083	2.467		5.27	–0.96	16d*			
trans-$[Pt(NH_3)_2L^T(H_2O)]^{n+}$														27			
$L^T = H_2O$	2.066			2.408			2.066			2.426							
$L^T = NH_3$	2.109			2.470			2.109			2.476							
$L^T = OH^-$	2.190			2.689			2.190			2.688							
$L^T = F^-$	2.140			2.561			2.140			2.562							
$L^T = Cl^-$	2.180			2.566			2.180			2.566							
$L^T = Br^-$	2.203			2.581			2.203			2.581							
$L^T = H_2S$	2.136			2.446			2.136			2.450							
$L^T = CH_3S^-$	2.281			2.826			2.281			2.880							
$L^T = SCN^-$	2.179			2.570			2.179			2.583							
$L^T = CN^-$	2.224			2.581			2.224			2.581							
$L^T = PH_3$	2.189			2.483			2.189			2.484							
$L^T = CO$	2.125			2.396			2.125			2.396							
$L^T = NO_2^-$	2.219			2.564			2.219			2.564							
$L^T = CH_3^-$	2.335			3.684			2.335			3.785							
$L^T = H^-$	2.319			3.075			2.319			3.294							
$L^T = C_2H_4$	2.197			2.268			2.197			2.734							
Carboplatin				2.42						2.38				88	88.4	–15	31
Oxaliplatin		2.00	3.47	2.45		5.47		2.01	3.19	2.34		4.79	–0.68	32			
		2.00	3.46	2.48		5.46		2.08	3.28	2.44		4.92	–0.54	32*			
Rhodium Tetracarboxylate	2.07			2.93	0.86		2.07			2.64	0.57			89	49.0±1.0	–60	33
$[(\eta^6\text{-benzene})Ru^{II}(en)Cl]^+$	2.418			3.090	0.67		2.244			2.620	0.38			21	79.5±3.4	–30.8±11.5	34
		2.424	4.138	3.099		6.56		2.142	3.898	2.586		5.69	–0.88	35			
		2.479	4.221	3.238		6.70		2.168	4.271	2.884		6.12	–0.58	35*			
NAMI-A	2.42	2.44	4.86	3.679	1.26	7.30	2.23	2.125	4.642	3.127	0.90	6.81	–0.49	18c			
	2.42	2.387	4.506	3.92	1.50	6.89	2.23	2.141	4.608	3.23	1.00	7.15	0.26	18c*			
	2.43	2.45	4.30	2.99	0.56	6.75	2.21	2.14	4.69	2.56	0.35	5.55	–1.20	18a			
	2.44	2.45	4.12	4.26	1.82	6.57	2.20	2.15	4.68	3.89	1.69	8.15	1.58	**			
ICR	2.44	2.48	4.16	3.21	0.77	6.64	2.24	2.16	4.62	2.74	0.50	5.95	–0.69	19	117.0±7.0	55.0±23.0	36
	2.43	2.43	4.07	4.12	1.69	6.50	2.23	2.14	4.60	3.71	1.48	7.83	1.33	**			
TzICR	2.434	2.455	4.078	3.520	1.09	6.53		2.156	4.537	3.020		6.54	0.01	18d			
$(2\text{-}NH_2)$TzICR	2.450	2.462	4.084	3.044	0.59	6.55	2.227	2.252	4.765	2.606	0.38	5.65	–0.09	18d			

* optimization in solution, ** data in this work Σ_{RA} – the sum of the metal-leaving ligand bond RA(L) and the metal entering ligand RA(E) in the reactant complex; Σ_{TS} – the sum of the metal-ligands bonds of the transition state involved in substitution.

Table S2. Geometrical parameters of Ru(III) species formed during aquation of **1–4**

		1st step						2nd step (*cis*)							2nd step (*trans*)						
		R	**RA**	**TS**	**PA**	**P**	**P[b]**	**R**	**RA**	**TS**	**PA**	**P**	**P[a]**	**P[b]**	**R**	**RA**	**TS**	**PA**	**P**	**P[a]**	**P[b]**
1	Ru–Cl	2.44	2.45	4.26	4.68			2.35	2.37	2.88	4.01				2.33	2.35	2.85	4.17			
	Ru–O_w		4.12	3.89	2.15	2.20			4.03	2.65	2.16	2.16/2.21	2.20			4.03	2.40	2.06	2.07/2.16	2.24	
	Ru–O_h						1.96						1.96	1.98/1.99						1.93	1.99/2.04
2	Ru–Cl	2.43	2.43	4.12	4.60			2.38	2.39	3.60	4.00				2.31	2.32	2.84				
	Ru–O_w		4.07	3.71	2.14	2.23			4.20	3.51	2.17	2.19/2.18	2.23			4.20	2.38		2.11/2.11	2.26	
	Ru–O_h						1.99						1.96	1.99/2.00						1.92	2.01/2.02
3	Ru–Cl	2.45		4.26				2.39		3.60					2.30		2.85				
	Ru–O_w			3.50		2.23				3.34		2.18/2.19	2.22				2.40		2.11/2.11	2.25	
	Ru–O_h						1.96						1.97	1.97/1.97						1.93	2.00/2.00
4	Ru–Cl	2.44		3.79				2.38		3.59					2.32		2.84				
	Ru–O_w			3.41		2.22				3.38		2.18/2.19	2.22				2.39		2.12/2.12	2.25	
	Ru–O_h						1.96						1.97	1.97/1.97						1.91	2.05/2.05

R reactants, **RA** reactants adducts **TS**-transition stratures, **PA** products adducts **P** products. Ru–Cl bond broken during aquation, Ru–O_w ruthenium aqua ligand bond formed during aquation. Ru–O_h rutheniium hydroxido ligand bond, formed by deprotonation of aqua ligand.
[a] hydroxido complexes [b] di-hydroxido complexes

Table S3. Geometrical parameters of Ru(II) species formed during aquation of **5–8**

		1st step					2nd step (*cis*)						2nd step (*trans*)					
		R	**TS1**	**TS2**	**P**	**P[b]**	**R**	**TS1**	**TS2**	**P**	**P[a]**	**P[b]**	**R**	**TS1**	**TS2**	**P**	**P[a]**	**P[b]**
5	Ru–Cl	2.55	4.17				2.52	3.75					2.44	4.70				
	Ru–O_w			3.36	2.27					2.20/2.23	2.24				3.32	2.15/2.18	2.32	
	Ru–O_h					2.07					2.07	2.07/2.09					2.06	2.11/2.19
6	Ru–Cl	2.54	3.61				2.57	3.49					2.43	4.54				
	Ru–O_w			3.82	2.27					2.23/2.24	2.27				4.17	2.17/2.17	2.37	
	Ru–O_h					2.08					2.08	2.10/2.10					2.06	2.15/2.16
7	Ru–Cl	2.57	3.53				2.58	3.32					2.46					
	Ru–O_w			3.96	2.23					2.22/2.22					3.80	2.16/2.17		
	Ru–O_h					2.08												
8	Ru–Cl	2.55	3.89				2.50	3.71					2.45	4.84				
	Ru–O_w			3.82	2.23				4.30	2.22/2.22	2.23				3.53	2.16/2.16	2.33	
	Ru–O_h					2.19					2.04	2.05/2.05					2.02	2.09/2.09

R reactants, **TS**-transition states (**TS1/TS2** first/second step of **D** mechanism), **P** products. Ru–Cl bond broken during aquation, Ru–O_w ruthenium aqua ligand bond formed during aquation. Ru–O_h rutheniium hydroxido ligand bond, formed by deprotonation of aqua ligand.
[a] mono-hydroxido complexes [b] di-hydroxido complexes

Table S4. Computed pK_a of mono and di-aqua species

	mono-aqua	*cis*-di-aqua		*trans*-di-aqua	
	pK_a	pK_a1	pK_a2	pK_a1	pK_a2
1	3.4	–0.4	6.5	–1.8	10.0
2	4.3	2.0	8.7	1.0	10.8
3	3.1	–0.6	6.6	0.5	11.5
4	2.3	–2.4	6.1	–3.4	8.0
5	18.6	13.7	19.5	14.6	20.9
6	16.4	17.1	19.0	19.0	20.0
7	16.0	16.1	17.8		
8	12.7	15.0	16.7	16.9	18.0

Table S5. Free energies relative to separated reactants of the species involved in the aquation process up to the second step (kcal/mol) of Ru(II) compounds. Dissociative mechanism

	R	TS1**D1***	I1	TS1**D2**	P1	*cis*-TS2**D1**	*cis*-I2	*cis*-TS2**D2**	*cis*-P2	*trans*-TS2**D1**	*trans*-I2	*trans*-TS2**D2**	*trans*-P2
5	0	12.9	2.4	11.7	–5.6	10.0	3.1		–5.9	16.0	2.2	15.9	–6.0
6	0	11.8	4.6	10.5	0.1	7.6	3.5		–2.3	16.8	5.3	11.0	–4.2
7	0	9.5	4.0	10.3	–1.8	7.7	4.1		–3.8		4.7	9.2	–5.8
8	0	12.1	5.2	11.3	–1.7	10.7	5.6	12.1	–2.5	18.9	6.7	11.4	–4.5

* The digit following the transition states designator (TS) denotes the aquation step. The first and second steps of **D** mechanism are symbolized by **D1** and **D2** respectively.

Table S6. Free energies relative to separated reactants of the species involved in the aquation process up to the second step (kcal/mol) of ruthenium(II) compounds. Interchange mechanism

	R	TS1	P1	cis-TS2	cis-P2	trans-TS2	trans-P2
5	0		–5.6	14.2	–5.9	21.9	–6.0
6	0		0.1	13.6	–2.3	23.6	–4.2
7	0	13.6	–1.8	13.2	–3.8	22.6	–5.8
8	0	16.1	–1.7	16.8	–2.5	24.8	–4.5

Table S7. Interaction energies of the metal orbitals with the axial ligands orbitals in **2–4** and **6–10** (kcal/mol)

Orbital	Representation		Formula	**9**	**10**	**2**	**6**	**3**	**7**	**4**	**8**
	C_{2h}	C_{2v}									
d_{z2},5s	a_g	a_1	a_1	–69.8	–61.4	–65.5	–57.0	–65.0	–56.6	–64.5	–58.2
$5p_z$	b_u	b_1	b_u	–16.5	–17.4	–17.7	–17.2	–21.1	–20.5	–20.1	–20.4
$4d_{yz}$	b_g	a_2	a_2	–23.1	–35.5	–15.6	–31.3	–15.8	–33.1	–20.9	–54.0
$4d_{xz}$	a_g	b_1	b_1–b_u	–20.0	–31.3	–9.4	–13.2	–12.7	–16.4	–12.9	–16.6
$4d_{xy}$	b_g	b_2	b_g–a_2	–3.9	–2.7	–7.4	–5.3	–6.0	–3.6	–5.2	–1.3
$4d_{x2–y2}$	a_g	a_1	0								
$5p_x$	b_u	a_1	0[a]								
$5p_y$	a_u	b_2	a_u	–3.3	–5.1	–2.8	–3.3	–3.0	–3.9	–3.2	–5.8

[a] assumption

Table S8. Decomposition of interaction energy between $[RuCl_4]^{-/2-}$ and the axial ligands in **2**, **3** and in their reduced forms **6** and **7** (kcal/mol)

	C_{2h}				C_{2v}			
	2	**6**	**3**	**7**	**2**	**6**	**3**	**7**
E_{int}	–75.7	–55.1	–87.9	–79.1	–75.6	–55.2	–86.8	–77.7
E_{solv}	–79.9	–214.3	–63.6	–191.0	–80.0	–214.3	–63.1	–192.3
$E_{int+solv}$	–155.6	–269.4	–151.5	–270.1	–155.6	–269.5	–149.9	–270.0
ΔE_{Pauli}	183.6	197.5	183.6	197.9	183.5	197.4	183.3	197.5
ΔE_{elst}	–165.6	–158.5	–172.6	–176.0	–165.5	–158.5	–172.5	–175.7
ΔE_{orb}	–93.7	–94.1	–98.9	–101.0	–93.7	–94.1	–97.6	–99.4
$\Delta E_{\Gamma i}$: C_{2h} (C_{2v})								
a_g (a_1)	–75.0	–70.2	–79.1	–74.3	–65.5	–57.0	–65.0	–56.6
b_g (a_2)	–23.0	–36.5	–21.8	–36.7	–15.6	–31.3	–15.8	–33.1
a_u (b_1)	–2.8	–3.3	–3.0	–3.9	–27.1	–30.4	–33.8	–36.9
b_u (b_2)	–17.7	–17.2	–21.1	–20.5	–10.3	–8.6	–9.2	–7.5

Table S9. Basis set dependence of the charge transfer between metal orbitals and axial ligands orbitals in **2–4** and **6–10** (C_{2h})

Representation	**9**	**10**	**2**	**6**	**3**	**7**	**4**	**8**
C_{2h}								
a_g	0.43(0.46)	0.39(0.39)	0.32(0.36)	0.28(0.31)	0.33(0.36)	0.29(0.31)	0.33(0.35)	0.31(0.32)
a_u	0.05(0.07)	0.07(0.12)	0.05(0.06)	0.11(0.13)	0.06(0.06)	0.15(0.17)	0.08(0.09)	0.29(0.32)
b_g	0.00(0.00)	0.00(0.00)	0.00(0.00)	0.00(0.00)	0.00(0.00)	0.00(0.00)	0.00(0.00)	0.00(0.00)
b_u	0.00(0.20)	0.00(0.18)	0.00(0.12)	0.00(0.03)	0.00(0.11)	0.00(0.10)	0.00(0.10)	0.00(0.02)

Values are computed at B3LYP/ZORA level using QZV4P basis at ruthenium and other atoms. Values in paranthesis are computed by using TZV2P quality basis.

Table S10. Basis set dependence of the charge transfer between metal orbitals and axial ligands orbitals in **2–4** and **6–10** (C_{2v})

Representation	**9**	**10**	**2**	**6**	**3**	**7**	**4**	**8**
C_{2v}								
a_1	0.43(0.46)	0.39(0.39)	0.32(0.36)	0.28(0.31)	0.33(0.35)	0.29(0.30)	0.33(0.35)	0.31(0.32)
a_2	0.04(0.04)	0.07(0.12)	0.05(0.06)	0.11(0.13)	0.06(0.06)	0.15(0.17)	0.08(0.09)	0.29(0.32)
b_1	0.00(0.20)	0.12(0.16)	0.00(0.11)	0.00(0.11)	0.00(0.10)	0.00(0.10)	0.00(0.10)	0.00(0.03)
b_2	0.00(0.00)	0.00(0.03)	0.00(0.00)	0.00(0.00)	0.00(0.00)	0.00(0.00)	0.00(0.00)	0.00(0.00)

The values are computed at B3LYP/ZORA level using QZV4P basis at ruthenium and other atoms. Values in paranthesis are computed by using TZV2P quality basis.

Table S11. Decomposition of interaction energy in *trans*,*trans* -[$RuCl_2(OH_2)(Hpz)_2$] (*trans*-di-aqua-**7**) and *trans*,*trans* -[$RuCl_2(OH_2)(Hind)_2$] (*trans*-di-aqua-**8**) (kcal/mol)

	C_{2h}		C_{2v}	
	trans-di-aqua-**7**	*trans*-di-aqua-**8**	*trans*-di-aqua-**7**	*trans*-di-aqua-**8**
E_{int}	–98.0	–95.7	–96.7	–94.7
E_{solv}	–26.7	–26.5	–27.8	–27.2
$E_{int+solv}$	–124.7	–122.1	–124.5	–121.9
ΔE_{Pauli}	192.3	208.6	191.9	208.5
ΔE_{elst}	–187.8	–196.3	–187.6	–196.3
ΔE_{orb}	–102.5	–108.0	–101.1	–106.9
$\Delta E_{\Gamma i}$: C_{2h} (C_{2v})				
a_g (a_1)	–78.5	–80.7	–62.2	–64.3
b_g (a_2)	–24.9	–30.8	–19.2	–25.9
a_u (b_1)	–3.4	–3.7	–33.9	–34.4
b_u (b_2)	–18.9	–19.0	–9.0	–8.5

Table S12. Computed standard redox potentials in eV vs NHE

	Y											
	Cl	**SH_2**	**MeSH**	**Me_2S**	**Ade**	**OH_2**	**Gua**	**Im**	**NH_3**	**$MeNH_2$**	**MeS^-**	**OH^-**
1–Y	0.07	0.42	0.32	0.29	0.31	0.27	0.12	0.14	0.14	0.11	–0.34	–0.65
2–Y	–0.25	0.12	0.03	–0.01	–0.10	–0.18	–0.27	–0.25	–0.29	–0.29	–0.68	–0.89
3–Y	–0.19	0.31	0.25	0.18	0.10	0.02	–0.04	–0.03	–0.03	–0.07	–0.56	–0.72
4–Y	0.02	0.40	0.36	0.29	0.22	0.16	0.11	0.10	0.09	0.04	–0.42	–0.50
pK_a (exp)	–8.00				< –2.0[49]	–1.70	~3[49]	7.11[48]	9.25	10.64	10.40	15.75

Table S13. Experimental and computed pK_a's values of free azoles

	calc	exp[48]
H–Ind	1.1	1.25
H–Pz	3.1	2.64
H–Im	7.8	7.11

Table S14. Computed standard redox potentials in eV vs NHE, at ε = 10

	Y											
	Cl	**SH_2**	**MeSH**	**Me_2S**	**Ade**	**OH_2**	**Gua**	**Im**	**NH_3**	**$MeNH_2$**	**MeS^-**	**OH^-**
1–Y	–0.53	0.20	0.14	0.04	0.02	–0.05	–0.15	–0.12	–0.10	–0.13	–0.93	–0.95
2–Y	–0.70	0.10	0.02	–0.04	–0.10	–0.19	–0.30	–0.26	–0.27	–0.30	–1.08	–1.28
3–Y	–0.88	–0.15	–0.24	–0.27	–0.35	–0.45	–0.57	–0.54	–0.56	–0.56	–1.29	–1.51
4–Y	–0.48	0.19	0.12	0.06	0.09	0.04	–0.14	–0.11	–0.09	–0.11	–0.89	–1.18
pK_a (exp)	–8.00				< –2.0[49]	–1.70	~3[49]	7.11[48]	9.25	10.64	10.40	15.75

Table S15. Predicted activation (ΔG_a) and reaction free energies (ΔG_r) in kcal/mol of the aqua substitution in mono–aqua complexes of **1–4** by **Y** (Chart 2)

	ΔG_a									
	SH_2	**MeSH**	**Me_2S**	**Ade**	**Gua**	**Gua***	**Im**	**NH_3**	**$MeNH_2$**	**MeS^-**
1–OH_2	21.7	22.8	24.0	26.5	23.7	27.6	23.2	24.5	24.2	28.9
2–OH_2	19.8	20.0	20.9	20.8	20.1	22.3	18.9	23.7	22.6	23.3
3–OH_2	20.8	21.5	21.7	21.5	20.1	19.7	20.3	21.2	24.5	20.6
4–OH_2	21.3	22.2	21.7	21.7	20.6	23.7	20.0	20.3	24.1	20.6
	ΔG_r									
1–OH_2	–2.6	–5.2	–5.3	–2.7	–1.9	–9.1	–13.3	–14.0	–15.0	–20.7
2–OH_2	–4.1	–6.6	–6.4	–6.8	–3.8	–15.9	–14.2	–14.4	–14.7	–22.9
3–OH_2	–3.8	–6.7	–7.3	–5.3	–4.7	–14.3	–14.6	–14.2	–15.5	–24.6
4–OH_2	–3.5	–6.3	–6.9	–5.5	–5.4	–10.4	–14.5	–14.3	–15.5	–24.9

Table S16. Predicted activation ΔG_a and reaction free energies ΔG_r in kcal/mol of the biological models **Y** (Chart 2) binding to **5–OH_2 : 8–OH_2**.

Second step of **D** mechanism

	ΔG_a									
	SH_2	**MeSH**	**Me_2S**	**Ade**	**Gua**	**Gua***	**Im**	**NH_3**	**$MeNH_2$**	**MeS^-**
5–OH_2	13.4	13.5	16.8	19.1	19.1	14.8	17.9	13.5	15.9	17.9
6–OH_2	9.7	10.0	11.4	11.2	13.4	6.5	11.9	9.0	8.9	11.4
7–OH_2	10.6	12.3	11.9	12.3	13.4	6.4	9.9	10.4	10.4	8.8
8–OH_2	11.8	11.8	12.7	12.3	14.1	10.1	10.4	11.9	11.8	11.1
	ΔG_r									
5–OH_2	–6.1	–7.1	–5.9	–3.7	1.7	–12.8	–10.1	–11.0	–11.5	–6.3
6–OH_2	–11.0	–11.6	–10.8	–8.7	–2.0	–17.5	–12.5	–11.9	–12.0	–10.4
7–OH_2	–10.6	–11.9	–11.3	–7.3	–3.1	–16.2	–13.4	–12.9	–13.2	–10.7
8–OH_2	–9.5	–11.1	–9.9	–7.1	–4.4	–16.3	–13.1	–12.7	–13.0	–10.9

Table S17. Characteristic metal-ligand bonds involved in the substitution process at Ru(III) centers in mono-aqua complexes of **1–4**.

		Reactants		Transition Structures										Products									
		R	**R***	**SH_2**	**MeSH**	**Me_2S**	**Ade**	**Gua**	**Gua***	**Im**	**NH_3**	**$MeNH_2$**	**MeS^-**	**SH_2**	**MeSH**	**Me_2S**	**Ade**	**Gua**	**Gua***	**Im**	**NH_3**	**$MeNH_2$**	**MeS^-**
1–OH_2	Ru–Cl[a]	2.33	2.30	2.29	2.29	2.29	2.29	2.34	2.34	2.28	2.30	2.30	2.39	2.35	2.36	2.37	2.37	2.36	2.32	2.38	2.36	2.37	2.43
	Ru–Cl																						
	Ru–O[b]	2.20	2.21	3.93	3.89	3.94	3.64	3.57	2.59	3.81	4.02	3.92	2.57										
	Ru–O*		2.16						2.21										2.10				
	Ru–S[c]			4.03	4.00	4.29							3.11	2.51	2.5	2.48							2.33
	Ru–N[d]						3.50	3.98	2.58	3.67	3.56	3.73					2.18	2.17	2.24	2.13	2.17	2.18	
2–OH_2	Ru–Cl[a]	2.31	2.31	2.28	2.28	2.28	2.28	2.28	2.31	2.28	2.28	2.29	2.33	2.33	2.34	2.34	2.34	2.34	2.34	2.35	2.34	2.35	2.46
	Ru–Cl																						
	Ru–O[b]	2.23	2.21	3.95	3.88	3.72	3.53	3.68	3.67	3.54	3.86	3.79	3.42										
	Ru–O*		2.19																2.16				
	Ru–S[c]			3.54	3.75	3.90							4.31	2.51	2.48	2.50							2.32
	Ru–N[d]						3.35	4.21	3.49	3.48	3.48	3.46					2.19	2.19	2.18	2.16	2.17	2.18	
3–OH_2	Ru–Cl[a]	2.30	2.32	2.27	2.27	2.27	2.27	2.28	2.27	2.27	2.27	2.29	2.32	2.32	2.33	2.33	2.34	2.33	2.33	2.34	2.33	2.33	2.46
	Ru–Cl																						
	Ru–O[b]	2.22	2.19	3.89	3.75	3.64	3.71	3.70	3.60	3.37	3.43	3.60	3.22										
	Ru–O*		2.18						2.11										2.10				
	Ru–S[c]			3.61	3.76	3.79							3.96	2.51	2.48	2.50							2.31
	Ru–N[d]						3.65	3.73	3.47	3.28	3.17	3.71					2.19	2.19	2.16	2.15	2.18	2.19	
4–OH_2	Ru–Cl[a]	2.32	2.32	2.28	2.27	2.27	2.27	2.27	2.31	2.29	2.27	2.29	2.32	2.31	2.32	2.33	2.35	2.32	2.33	2.34	2.33	2.33	2.45
	Ru–Cl																						
	Ru–O[b]	2.22	2.19	3.84	3.69	3.61	3.67	3.95	3.66	3.89	3.81	3.64	3.20										
	Ru–O*		2.18						2.10										2.16				
	Ru–S[c]			4.09	3.77	3.78							3.97	2.52	2.49	2.50							2.31
	Ru–N[d]						3.57	3.63	3.34	3.60	3.18	3.69					2.17	2.25	2.17	2.16	2.18	2.19	

[a] *trans* bonded Cl ligand to the leaving/entering ligand

[b] Ru–O(leaving water)

[c] Ru–S(entering sulfur containing ligands)

[d] Ru–N(entering nitrogen containing ligands)

* Substitution at *cis*-di-aqua species

Table S18. Characteristic metal-ligand bonds involved in the substitution process at Ru(II) centers in **5–OH_2 : 8–OH_2**. Second step of **D** mechanism

		Reactants		Transtition Structures										Products								
		R	**R***	**SH_2**	**MeSH**	**Me_2S**	**Ade**	**Gua**	**Gua***	**Im**	**NH_3**	**$MeNH_2$**	**MeS^-**	**SH_2**	**MeSH**	**Me_2S**	**Ade**	**Gua**	**Gua***	**Im**	**NH_3**	**$MeNH_2$**	**MeS^-**
5–OH_2	Ru–Cl[a]	2.44	2.44	2.39	2.39	2.39	2.38	2.42	2.37	2.38	2.39	2.38	2.39	2.50	2.48	2.48	2.48	2.48	2.43	2.49	2.49	2.49	2.52
	Ru–Cl																						
	Ru–O[b]	2.24	2.27																				
	Ru–O		2.24						2.18										2.18				
	Ru–S[c]			4.02	4.31	3.95							4.49	2.40	2.37	2.39							2.48
	Ru–N[d]						3.88	2.78	4.02	3.28	3.64	3.73					2.16	2.11	2.21	2.15	2.15	2.16	
6–OH_2	Ru–Cl[a]	2.43	2.44	2.38	2.38	2.39	2.38	2.39	2.39	2.39	2.38	2.38	2.44	2.46	2.47	2.47	2.47	2.47	2.45	2.48	2.48	2.48	2.54
	Ru–Cl																						
	Ru–O[b]	2.27	2.27																				
	Ru–O		2.27						2.21										2.19				
	Ru–S[c]			3.96	3.67	4.09							3.90	2.34	2.34	2.36							2.45
	Ru–N[d]						4.61	3.25	4.15	3.01	3.27	3.69					2.14	2.10	2.08	2.11	2.14	2.16	
7–OH_2	Ru–Cl[a]	2.46	2.45	2.37	2.37	2.38	2.40	2.38	2.37	2.39	2.37	2.37	2.42	2.44	2.45	2.45	2.47	2.45	2.46	2.50	2.46	2.46	2.50
	Ru–Cl																						
	Ru–O[b]	2.23	2.23																				
	Ru–O		2.23						2.20										2.18				
	Ru–S[c]			4.68	3.94	4.18							3.94	2.36	2.36	2.37							2.48
	Ru–N[d]						4.73	3.26	3.95	2.93	3.36	4.01					2.15	2.11	2.10	2.11	2.15	2.17	
8–OH_2	Ru–Cl[a]	2.45	2.45	2.36	2.37	2.36	2.37	2.40	2.37	2.38	2.36	2.36	2.40	2.43	2.44	2.44	2.48	2.43	2.45	2.47	2.45	2.45	2.49
	Ru–Cl																						
	Ru–O[b]	2.23	2.23																				
	Ru–O		2.23						2.18										2.18				
	Ru–S[c]			4.15	3.89	4.38							4.16	2.37	2.37	2.38							2.47
	Ru–N[d]						4.40	3.27	3.92	3.05	3.36	4.32					2.15	2.18	2.10	2.12	2.15	2.17	

[a] *trans* bonded Cl ligand to the entering ligand
[b] Ru–O(leaving water)
[c] Ru–S(entering sulfur containing ligands)
[d] Ru–N(entering nitrogen containing ligands)
* Substitution at *cis*-di-aqua species

Table S19. Ru(II) radii calibration to experimental data on energetics (kcal/mol) of the substitution process: $Ru^{II}L_5OH_2 + Y \rightarrow Ru^{II}L_5Y + H_2O$

Y					**OH_2**		**py**		**ACN**	
	r (Ru) Å	**R**	**TSD1**	**I**	**TSD2**	**P**	**TSD2**	**P**	**TSD2**	**P**
exp					19.9[90a]		16.2[90b]		16.7[90b]	
$[Ru^{II}(OH_2)_6]^{2+}$	1.48	0	12.29	5.98	12.29	0				
	1.58	0	14.01	8.33	14.01	0				
	1.68	0	15.23	10.30	15.23	0				
	1.78	0	16.05	11.87	16.05	0				
	1.88	0	16.71	13.17	16.71	0				
	1.98	0	17.26	13.98	17.26	0				
	2.08	0	17.67	14.68	17.67	0				
	2.18	0	17.84	15.26	17.84	0				
$[Ru^{II}(NH_3)_5(OH_2)]^{2+}$	1.48	0	12.51	1.89			15.40	–10.97	5.22	–18.77
	1.58	0	12.46	3.55			15.36	–10.98	5.86	–18.81
	1.68	0	12.53	4.61			15.31	–11.01	8.02	–18.72
	1.78	0	12.97	5.55			15.20	–11.05	7.98	–18.86
	1.88	0	13.29	6.25			15.23	–11.02	8.61	–18.81
	1.98	0	13.44	6.72			15.23	–11.03	8.88	–18.80
	2.08	0	13.53	7.07			15.05	–11.05	9.24	–18.81
	2.18	0	13.65	7.38			15.21	–11.06	9.42	–18.83

R-reactants, **TS**-transition states, **I**-intermediates, and **P** products in the limiting **D** mechanism with **D1**-first, and **D2**-second step.The calibration was started from default radius for ruthenium atoms as defined in Jaguar 7.0[80] (1.48 Å) with the step size of 0.1 Å. We have chosen the value of 2.08 Å for computations since the consideration of larger radii (2.18 Å) does not improve the activation energies of processes (ΔE ~ 0.2 kcal/mol by changing Ru radii from 2.08 Å to 2.18 Å) and the value of 2.18 Å already exceed the Ru–N(azole) bond distances. The calibration does not change the preference for the **D** over **Id** mechanism of aquation process of studied reduced species (Table S20).

Table S20. Influence of Ru(II) radii calibration on the ΔG_a (kcal/mol) of aquation of **7** and **8**

r (Ru^{II})	1.48		2.08	
Mechanism	**Id**	**D**	**Id**	**D**
7	14.8	9.4	13.6	10.3
8	17.9	17.7	16.1	12.1

IV.10. References

(1) (a) Jamieson, E. R.; Lippard, S. J. *Chem. Rev.* **1999**, *99*, 2467. (b) Fuertes, M. A.; Alonso, C.; Pérez, J. M. *Chem. Rev.* **2003**, *103*, 645. (c) Jakupec, M. A.; Galanski, M.; Keppler, B. K. *Rev. Physiol. Bioch. Pharmacol.* **2003**, *146*, 1. (d) Jung, Y.; Lippard, S. J. *Chem. Rev.* **2007**, *107*, 1387. Cisplatin: *cis*-diamminedichloridoplatinum(II); carboplatin: cis-diammine(1,1-cyclobutanedicarboxylato)platinum(II); oxaliplatin: (1*R*,2*R*-diaminocyclohexane)oxalatoplatinum(II).

(2) Rosenberg B.; Van Camp, L. *Nature*, **1969**, *222*, 385.

(3) Jakupec, M. A.; Galanski, M.; Arion, V. B.; Hartinger, C. G.; Keppler, B. K. *Dalton Trans.* **2008**, *2*, 183.

(4) Chifotides, H. T.; Dunbar, K. R. *Acc. Chem. Res.* **2005**, *38*, 146.

(5) Clarke, M. J. *Coord. Chem. Rev.* **2003**, *236*, 209.

(6) (a) Mestroni, G.; Alessio, E.; Sava, G.; Pacor, S.; Coluccia, M. In *Metal Complexes in Cancer Chemotherapy*. Keppler, B. K., Ed.; VCH: Weinheim, Germany, 1993, p. 157. (b) Mestroni, G.; Alessio, E.; Sava, G.; Pacor, S.; Coluccia, M.; Boccarelli, A. *Metal Based Drugs* **1993**, *1*, 41. (c) Sava, G.; Capozzi, I.; Clerici, K.; Gagliardi, R.; Alessio, E.; Mestroni, G. *Clin. Exp. Metastasis* **1998**, 16, 371. (d) Sava, G.; Alessio, E.; Bergamo, A.; Mestroni, G. *Top. Biol. Inorg. Chem.* **1999**, *1*, 143. (e) Alessio, E.; Mestroni, G.; Bergamo, A.; Sava, G. In *Metal Ions in Biological Systems*. Sigel, A.; Sigel, H., Ed.; Marcel Dekker: New York, 2004, Vol. 42, p 323.

(7) (a) Keppler, B. K.; Rupp, W.; Juh, U. M.; Enders, H.; Niebl, R.; Balzer, W. *Inorg. Chem.* **1987**, *26*, 4366. (b) Keppler, B. K.; Berger, M. R.; Heim, M. H. *Cancer Treatments Rev.* **1990**, *17*, 261.

(8) (a) Galanski, M.; Arion, V. B.; Jakupec, M. A.; Keppler, B. K. *Curr. Pharm. Des.* **2003**, *9*, 2078. (b) Rademaker-Lakhai, J. M.; van den Bongard, D.; Pluim, D.; Beijnen, J. H.; Schellens, J. H. M. *Clin. Cancer Res.* **2004**, *10*, 3717. (c) Hartinger, C. G.; Zorbas-Seifried, S.; Jakupec, M. A.; Kynast, B.; Zorbas, H.; Keppler, B. K. *J. Inorg. Biochem.* **2006**, *100*, 891.

(9) Gianferrara, T.; Bratsos, I.; Alessio, E. *Dalton Trans.* **2009**, DOI: 10.1039/b905798f.

(10) (a) Yan, Y. K.; Melchart, M.; Habtemariam, A.; Sadler, P. J. *Chem. Comm.* **2005**, *38*, 4764. (b) Ang, W. H.; Dyson, P. J. *Eur. J. Inorg. Chem.* **2006**, *20*, 4003.

(11) Pongratz, M.; Schluga, P.; Jakupec, M. A.; Arion, V. B.; Hartinger, C. G.; Allmaier, G.; Keppler, B. K. *J. Anal. At. Spectrom.*, **2004**, *19*, 46.

(12) Timerbaev, A. R.; Hartinger, C. G.;. Aleksenko S. S; Keppler, B. K. *Chem. Rev.*, **2006**, *106*, 2224.

(13) (a) Kelman, A. D.; Clarke, M. J.; Edmonds, S. D.; Peresie, H. J. *J. Clin. Hematol. Oncol.* **1977**, *7*, 274. (b) Clarke, M. J. In *Metal Complexes in Cancer Chemotherapy* Keppler, B. K. Ed.; VCH, Weinheim, 1993, p. 129.

(14) Brown, J. M.; Giaccia, A. J. *Cancer Res.* **1998**, *58*, 1408.

(15) Reisner, E.; Arion, V. B.; Keppler, B. K.; Pombeiro, A. J. L. *Inorg. Chim. Acta* **2008**, *6*, 1569.

(16) (a) Zhang, Y.; Guo, Z. J.; You, X. Z. *J. Am. Chem. Soc.* **2001**, *123*, 9378. (b) Cooper, J.; Ziegler, T. *Inorg. Chem.* **2002**, *41*, 6614 (c) Robertazzi, A.; Platts, J. A. *J. Comput. Chem.* **2004**, *25*, 1060. (d). Burda, J. V.; Zeizinger, M.; Leszczynski, J. *Comput. Chem.* **2005**, *26*, 907. (e) Lau, J. K.-C.; Deubel, D. V. *J. Chem. Theory Comput.* **2006**, *2*, 103.

(17) (a) Baik, M.-H.; Friesner, R. A.; Lippard, S. J. *J. Am. Chem. Soc.* **2003**, *125*, 14082. (b) Robertazzi, A.; Platts, J. A. *Chem. Eur. J.* **2006**, *12*, 5747.

(18) (a) Chen, J.; Chen, L.; Liao, S.; Zheng, K.; Ji, L. *J. Phys. Chem. B* **2007**, *111*, 7862. (b) Vargiu, A. V.; Robertazzi, A.; Magistrato, A.; Ruggerone, P.; Carloni, P. *J. Phys. Chem. B*, **2008**, *112*, 4401. (c) Besker, N.; Coletti, C.; Marrone, A.; Re, N. *J. Phys. Chem. B*, **2008**, *112*, 3871. (d) Chen, J.-C.; Chen, L.-M.; Liao, S.-Y.; Zheng, K.-C.; Ji, L.-N. *Phys. Chem. Chem. Phys.* **2009**, *11*, 3401.

(19) Chen, J.; Chen, L.; Liao, S.; Zheng, K.; Ji, L. *Dalton Trans*, **2007**, *32*, 3507.

(20) Besker, N.; Coletti, C.;Marrone, A.; Re. N. *J. Phys. Chem. B*, **2007**, *111*, 9955.

(21) Deubel, D. V.; Lau, J. K.-C. *Chem. Comm.* **2006**, 2451.

(22) Holler, E.; Schaller, E.; Keppler, B. K. *Arzneim.-Forsch. / Drug Res.* **1991**, *41*, 1065.

(23) (a) Deubel, D. V. *J. Am. Chem. Soc.* **2002**, *124*, 5834. (b) Deubel, D. V. *J. Am. Chem. Soc.* **2004**, *126*, 5999. (c) Lau, J. K.-C.; Deubel, D. V. *Chem.-Eur. J.* **2005**, *11*, 2849.

(24) Cebrian-Losantos, B.; Reisner, E.; Kowol, C. R.; Roller, A.; Shova, S.; Arion, V. B.; Keppler, B. K. *Inorg. Chem.* **2008**, *47*, 6513.

(25) Kamerlin, S. C. L.; Florian, J.; Warshel, A. *Chem. Phys. Chem.* **2008**, *9*, 1767.

(26) Rotzinger, F. P. *Chem. Rev.* **2005**, *105*, 2003.

(27) Chval, Z.; Sip, M.; Burda, J. V. *J. Comput. Chem.* **2008**, *29*, 2370.

(28) Chiorescu, I.; Deubel, D. V.; Arion, V. B.; Keppler, B. K. *J. Chem. Theory Comput.* **2008**, *4*, 499.

(29) Miller, S. E.; House, D. A. *Inorg. Chim. Acta* **1989**, *166*, 189.

(30) Burda, J. V.; Zeizinger, M.; Leszczynski, J. *J. Chem. Phys.* **2004**, *120*, 1253.

(31) Hay, R. W.; Miller, S. *Polyhedron*, **1998**, *17*, 2337.

(32) Lucas, M. F. A.; Pavelka, M.; Alberto, M. E.; Russo, N. *J. Phys. Chem. B* **2009**, *113*, 831.

(33) Pittet, P.-A.; Dadci, L.; Zbinden, P.; Abou-Hamdan, A.; Merbach, A. E. *Inorg. Chim. Acta* **1993**, *206*, 135.

(34) Wang, F.; Chen, H.; Parsons, S.; Oswald, I. D. H.; Davidson, J. E.; Sadler, P. *Chem. Eur. J.* **2003**, *9*, 5810.

(35) Burda, J. V. *Ref*

(36) Chatlas, J.; van Eldik, R.; Keppler, B. K. *Inorg. Chim. Acta* **1995**, *233*, 59.

(37) (a) Rotzinger, F. P. *J. Am. Chem. Soc.* **1996**, *118*, 6760. (b) Rotzinger, F. P. *J. Am. Chem. Soc.* **1997**, *119*, 5230.

(38) The difference between the sum of the bonds formed and broken during the aquation in TS and reactants adduct, which ultimately determines the change in the shape of the compound during the substitution process, and implicitly the volume change.

(39) (a) Bacac, M.; Hotze, A. C. G.; van der Schilden, K.; Haasnoot, J. G.; Pacor, S.; Alessio, E.; Sava, G.; Reedijk, J. *J. Inorg. Biochem.* **2004**, *98*, 402. (b) Sava, G.; Bergamo, A.; Zorzet, S.; Gava, B.; Casarsa, C.; Cocchietto, M.; Furlani, A.; Scarcia, V.; Serli, B.; Iengo, E.; Alessio, E.; Mestroni, G. *Eur. J. Cancer* **2002**, *38*, 427.

(40) (a) NAMI-A aquation rate constant at pH = 7–10: Bouma, M.; Nuijen, B.; Jansen, M. T.; Sava, G.; Flaibani, A.; Bult, A.; Beijnen, J. H. *Int. J. Pharm.* **2002**, *248*, 239. (b) ICR and KP1019 aquation rate constant: Küng, A.; Pieper, T.; Wissiack, R.; Rosenberg, E.; Keppler, B. K. *J. Biol. Inorg. Chem.* **2001**, *6*, 292.

(41) One should note that only the magnitude of the (Σ_{TS}–Σ_{RA}) parameter, without the inspection of the normal vibration modes in the transition state is not enough for a correct mechanism assessment. For example: the I_d mechanism is attributed to the process with large (Σ_{TS}–Σ_{RA}) parameter, only when the vibration mode of the imaginary frequency is

characteristic for concerted bending and stretching of the metal-entering and metal-leaving ligand bonds respectively.

(42) De Vito, D.; Sidorenkova, H.; Rotzinger, F. P.; Weber, J.; Merbach, A. E. *Inorg. Chem.* **2000**, *39*, 5547.

(43) The most reduced of the major redox active components in cells is the nicotinamide adenine dinucleotide phosphate ($NADPH/NADP^+$) couple, which has a value of approximately –400 mV. Because the $1/2O_2/H_2O$ couple has a value of approximately +800 mV, there is a large range over which variations in $E^{0'}$ of molecules reduced by NADPH and oxidized by O_2 can occur: Kirlin, W. G.; Cai, J.; Thompson, S. A.; Diaz, D.; Kavanagh, T. J.; Jones, D. P. *Free Rad. Biol. Med.* **1999**, *27*, 1208.

(44) Lever, A. B. P. *Inorg. Chem.* **1990**, *29*, 1271.

(45) (a) Morokuma, K. *J. Chem. Phys.* **1971**, *55*, 1236. (b) Ziegler, T.; Rauk, A. *Theor. Chim. Acta* **1977**, *46*, 1.

(46) By using this approach we can not compute separately the exact amount of donation to 5s or $4d_{z2}$ because they are totally symmetric in either C_{2h} or C_{2v}.

(47) (a) Landis, C. R.; Cleveland, T.; Firman, T. K. *J. Am. Chem. Soc.* **1995**, *117*, 1859. (b) Firman, T. K.; Landis, C. R. *J. Am. Chem. Soc.* **1998**, *120*, 12650. (c) Bayse, C. A.; Hall, M. B. *J. Am. Chem. Soc.* **1999**, *121*, 1348. (d) Frenking, G.; Froehlich, N. *Chem. Rev.* **2000**, *100*, 717. (e) Diefenbach, A.; Bickelhaupt, F. M.; Frenking, G. *J. Am. Chem. Soc.* **2000**, *122*, 6449. (f) Deubel, D. V. *J. Am. Chem. Soc.* **2002**, *124*, 12312. (g) Tai, H.-C.; Krossing, I.; Seth, M.; Deubel, D. V. *Organometalics* **2004**, *23*, 2343.

(48) Catalan, J.; Claramunt, R. M.; Elguero, J.; Laynez, J.; Menendez, M.; Anvia, F.; Quian, J. H.; Taagepera, M.; Taft, R. W. *J. Am. Chem. Soc.* **1988**, *110*, 4105.

(49) Lippert, B. In *Progress in Inorganic Chemistry*; Karlin, K. D., Ed.; Wiley & Sons: New York, 2005; Vol. 54, 385.

(50) (a) ICR aquation: Ni Dhubhghaill, O. M.; Hagen, W. R.; Keppler, B. K.; Lipponer, K.-G.; Sadler, P. J. *J. Chem. Soc. Dalton Trans.* **1994**, 3305. (b) KP1019 aquation: Pieper, T.; Peti, W.; Keppler, B. K. *Met.-Based Drugs* **2000**, *7*, 225.

(51) Among the selected library of ligands, disposed to acidification upon coordination to ruthenium, are also the N1 and exocyclic amine group of purine bases. These sites being not directly coordinated to the metal are less susceptible to metalation, as the distance to the metal is larger. The platination of the N7 guanine site induces a drop of 0.8 pKa units in the

N1 acidity enhancing the stability of Watson-Crick base pairing with cytosine in DNA.[49] The deprotonation of the exocyclic amino group of a purine base is less likely to occur (the reported shift of the exocyclic NH_2 group pK_a is ~ 4 units, from ~ 17 to > 13, upon adenine N7 coordination to Pt (II))[49] and therefore were not computed.

(52) Archontis, G.; Simonson, T. *J. Am. Chem. Soc.* **2001**, *123*, 11047.

(53) Monjardet-Bas, V.; Erizondo-Riojas, M. A.; Chottard, J. C.; Kozelka, J. *Angew. Chem., Int. Ed*. **2002**, *41*, 2998.

(54) Reisner, E.; Arion, V. B.; Guedes da Silva, M. F. C.; Lichtenecker, R.; Eichinger, A.; Keppler, B. K.; Kukushkin, V. Yu.; Pombeiro, A. J. L. *Inorg. Chem.* **2004**, *43*, 7083.

(55) Born, M. *Z. Physik* **1920**, *1*, 45.

(56) (a) Velders, A. H.; Bergamo, A.; Alessio, E.; Zangrando, E.; Haasnoot, E.; Casarsa, J. G.; Cocchietto, M.; Zorzet, S.; Sava, G. *J. Med. Chem.* **2004**, *47*, 1110. (b) Lipponer, K. G.; Vogel, E.; Keppler, B. K. *Met.-Based Drugs* **1996**, *3*, 243. (c) Velders, A. H.; Pazderski, L.; Ugozzoli, F.; Bianini-Cingi, M.; Manotti-Lanfredi, A. M.; Haasnoot, J. G.; Reedijk, J. *Inorg. Chim. Acta* **1998**, *273*, 259.

(57) Aquation rate constant $k = 6.3\times10^{-5}$ s^{-1}, ref. 29.

(58) Kratz, F.; Mulinacci, N.; Messori, L.; Bertini, I.; Keppler, B. K. *Met. Ions Biol. Med*. **1992**, *2*, 69.

(59) Wally, J.; Buchanan, S. K. *Biometals* **2007**, *20*, 249.

(60) Sun, H.; Li, H.; Sadler, P.J. *Chem. Rev*., **1999**, *99*, 2817.

(61) Millis, K. K.; Weaver, K. H.; Rabenstein, D. L. *J. Org. Chem.* **1993**, *58*, 4144.

(62) *CRC Handbook of Biochemistry and Molecular Biology. D. Physical and Chemical Data. Vol. 1*. Fasman, G. D. (Ed) 1985, p. 121.

(63) In contrast to the calculations presented in the ref. 18b which predict similar activation barriers for oxidized and reduced forms ICR and NAMI-A aquation, our data support experimental observation that reduction promotes aquation, since the reduced species hydrolyse much faster than ruthenium(III) complexes.[6b]

(64) Frühauf, S.; Zeller, W. J. *Cancer Res.* **1991**, *51*, 2943.

(65) Naqui, A.; Chance, B.; Cadenas, E. *Ann. Rev. Biochem.* **1986**, *55*, 137.

(66) Chance, B.; Sies, H.; Boveris, A. *Phys. Rev.* **1979**, *59*, 527.

(67) The H_2O_2 concentration of ~13 mM can be estimated from (a) the rate of H_2O_2 production in *HT29* colon cancer cell line ~0.1 nmol/10^4 cells/h: Szatrowski, T. P.; Nathan,

C. F.; *Cancer Res.* **1991**, *51*, 794; and (b) *HT29* average cell diameter of 11.4 μm: Katoh, M.; Feldhaus, S.; Schnitzer, T.; Bauer, S.; Schumacher, U. *Cancer Lett.* **2004**, *210*, 7.

(68) Halliwell, B.; Clement, M. V.; Long, L. H. *FEBS Letters*, **2000**, *486*, 10.

(69) Prousek, J. *Pure Appl. Chem.* **2007**, *79*, 2325.

(70) Yamazaki, I. *Quimica Nova* **1993**, *16*, 365.

(71) *Colon cancer cell line SW480*: KP1019 IC_{50} = 63 ± 3 μM: (a) Jakupec, M.A.; Reisner, E.; Eichinger, A.; Pongratz, M.; Arion, V. B.; Galanski, M.; Hartinger, C. G.; Keppler, B. K. *J. Med. Chem.* **2005**, *48*, 2831. ICR IC_{50} = 840 μM (not confirmed) (b) Arion, V. B.; Reisner, E.; Fremuth, M.; Jakupec, M. A.; Keppler, B. K.; Kukushkin, V. Yu.; Pombeiro, A. J. L. *Inorg. Chem.* **2003**, *42*, 6024. NAMI-A: no data. *HT29* KP1019 IC_{50} = 20 ± 10 μM; ICR IC_{50} >> 300 μM: (c) Kapitza, S.; Pongratz, M.; Jakupec, M. A.; Heffeter, P.; Berger, W.; Lackinger, L.; Keppler, B. K.; Marian, B. *J. Cancer Res. Clin. Oncol.* **2005**, *131*, 101. (d) NAMI-A IC_{50} = 339 ± 68: Groessl, M.; Reisner, E.; Hartinger, C. G.; Eichinger, R.; Semenova, O.; Timerbaev, A. R.; Jakupec, M. A.; Arion, V. B.; Keppler, B. K. *J. Med. Chem.* **2007**, *50*, 2185.

(72) Dougan, S. J.; Habtemariam, A.; McHale, S. E.; Parsons, S.; Sadler, P. J. *Proc. Natl. Acad. Sci.* **2008**, *105*, 11628.

(73) Becke, A. D. *J. Chem. Phys.* **1993**, *98*, 5648.

(74) Lee, C.; Yang, W.; Parr, R. G. *Phys. Rev. B* **1988**, *37*, 785.

(75) Gaussian 03, Revision D.01, Frisch, M. J. et al., Gaussian, Inc., Wallingford CT, 2004. www.gaussian.com

(76) Andrae, D.; Haeussermann, U.; Dolg, M.; Stoll, H.; Preuss, H. *Theor. Chim. Acta* **1990**, *77*, 123.

(77) (a) Hehre, W. J.; Ditchfield, R.; Pople, J. A. *J. Chem. Phys.* **1972**, *56*, 2257. (b) Binkley, J. S.; Pople, J. A.; Hehre, W. J. *J. Am. Chem. Soc.* **1980**, *102*, 939.

(78) Martin, J. M. L.; Sundermann, A. *J. Chem. Phys.* **2001**, *114*, 3408.

(79) (a) Tannor, D. J.; Marten, B.; Murphy, R. B.; Friesner, R. A.; Sitkoff, D.; Nicholls, A.; Ringnalda, M. N.; Goddard, W. A., III; Honig, B. *J. Am. Chem. Soc.* **1994**, *116*, 11875. (b) Marten, B.; Kim, K.; Cortis, C.; Friesner, R. A.; Murphy, R. B.; Ringnalda, M. N.; Sitkoff, D.; Honig, B. *J. Phys. Chem.* **1996**, *100*, 11775.

(80) Jaguar, version 7.0, Schrödinger, LCC, New York, NY, 2007. www.schrodinger.com.

(81) a) D. H. Wertz, *J. Am. Chem. Soc.* **1980**, *102*, 5316; b) M. H. Abraham, *J. Am. Chem. Soc.* **1981**, *103*, 6742.

(82) Jorgensen, W. L.; Briggs, J. M.; Gao, J. *J. Am. Chem. Soc.* **1987**, *109*, 6857.

(83) The free energy of proton in vacuo has only translational components: H = 1.481 kcal×mol^{-1}, and S = 26.014 cal×mol^{-1}K^{-1}.

(84) Tissandier, M. D.; Cowen, K. A.; Fendg, W. Y.; Gundlach, E.; Cohen, M. H.; Earhart, A. D.; Coe, J. V,; Tuttle, T. R. *J. Phys. Chem. A* **1998,** *102,* 7787.

(85) Lewis, A.; Bumpus, J. A.; Truhlar, D. G.; Cramer, C. J. *J. Chem. Ed.* **2004**, *81*, 596 incl. Addition/Correction.

(86) (a) te Velde, G.; Bickelhaupt, F.M.; van Gisbergen S. J. A.; Fonseca Guerra, C.; Baerends, E.J.; Snijders, J.G.; Ziegler, T. *J. Comput. Chem.* **2001,** *22*, 931. (b) ADF2007.01, SCM, Theoretical Chemistry, Vrije Universiteit, Amsterdam, The Netherlands. http://www.scm.com.

(87) (a) Van Lenthe, E.; Van Leeuwen, R.; Baerends, E. J.; Snijders, J. G. *Int. J. Quantum. Chem.* **1996**, *57*, 281. (b) Van Lenthe, E.; Ehlers, A.; Baerends, E. J. *J. Chem. Phys.* **1999**, *110*, 8943.

(88) Pavelka, M.; Lucas, M. F. A.; Russo, N. *Chem. Eur. J.* **2007**, *13*, 10108.

(89) Deubel, D. V.; Chifotides, H. T. *Chem. Commun.* **2007**, 3438.

(90) (a) $[Ru^{II}(OH_2)_6]^{2+}$:Rapaport, I.; Helm, L.; Merbach, A. E.; Bernhard, P.; Ludi, A. *Inorg. Chem.* **1988**, *27*, 873. (b) $[Ru^{II}(NH_3)_5(OH_2)]^{2+}$: Allen, R. J.; Ford, P. C. *Inorg. Chem.* **1972**, *11*, 679.

V. Electrochemistry of Antineoplastic Gallium, Iron and Ruthenium Complexes with Redox Non-Innocent α-N-Heterocyclic Chalcogensemicarbazones.

This chapter constitutes a collaboration between experiment and theory. Only sections V.4, V.5 and the theoretical parts of sections V.6, V.7 are being submitted as part of the thesis.

V.1. Abstract

The electrochemical properties of a series of α-N-heterocyclic chalcogensemicarbazones (HL), namely thiosemicarbazones, selenosemicarbazones and semicarbazones and their gallium(III), iron(III) and ruthenium(III) metal complexes with the general formula $[ML_2][Y]$ (M = Ga, Fe or Ru; Y = PF_6^- or NO_3^-) were studied in detail by cyclic voltammetry. All complexes show several, mostly reversible, redox waves attributable to the reduction of the non-innocent chalcogensemicarbazone ligand(s) at lower potentials (< –0.4 V *vs*. NHE) than the metal-centered iron or ruthenium redox waves (> 0 V *vs*. NHE) in organic electrolyte solutions. The cyclic voltammograms of the gallium complexes display at least two consecutive reversible one-electron reduction waves. These reductions are strongly shifted by ~0.6 V to lower potentials in the corresponding iron and ruthenium complexes. The ligand-centered reduction is supposed to take place at the $CH_3C{=}N$ double bond by comparing electrochemical, chemical and spectroscopic data. Quantum chemical calculations on the geometric and electronic structure of a thiosemicarbazone HL, the corresponding metal complexes $[Ga(L)_2]^+$ and $[Fe^{II}(L)_2]$, and the one-electron reduction product for each of these species support this assignment of the reduction site and elucidate the observed order of the ligand-centered redox potentials; $E_{1/2}([Fe^{II}(L)_2]) < E_{1/2}(HL) < E_{1/2}([Ga(L)_2]^+)$.

V.2. Introduction

Metal-based anticancer prodrugs may be activated selectively in the hypoxic tumor tissue upon reduction by biological reducing agents.[1,2] Electron-transfer can occur either to the metal-center, or, if in the biologically accessible range, to non-innocent ligands, resulting in reactive species capable of attacking biologically relevant target molecules either by ligand displacement at the low valent metal center or by radicals formed at the ligand entity, respectively. An "*activation-by-reduction*" step is thought to be important for platinum(IV) complexes which have been evaluated in clinical development, *e.g.* tetraplatin ([$PtCl_4$(1,2-$(NH_2)_2C_6H_4$)], abandoned), satraplatin ([$PtCl_2(OAc)_2(NH_3)(NH_2C_6H_5)$], phase III), and iproplatin ([$PtCl_2(OH)_2(NH_2{}^iPr)_2$], abandoned),[3] as well as for the activation of investigational ruthenium(III) prodrugs like *trans*-[$RuCl_4(Hind)_2$]$^-$ (KP1019) and *trans*-[$RuCl_4$(Him)(*S*-DMSO)]$^-$ (NAMI-A), both of which have already finished phase I clinical trials.[4-6] Indeed, an increasing metal-centered redox potential was shown to correlate with higher cytotoxicity for a series of platinum(IV)[7] and azole-based ruthenium(III) compounds.[8] Metal-centered redox pontenials can be tuned and predicted by application of Lever's parametrization method, facilitating markedly their design as bioreductive drugs.[1,9,10] Although hypoxia-selective organic drugs are under intensive investigation, *e.g.*, nitroimidazoles,[11] little is known about reductively activated metal-based compounds containing electronically non-innocent ligands with physiologically accessible redox potentials. One such example is ferrocenyl hydroxytamoxifen, containing a ferrocene-moiety attached to a hydroxylated form of the estrogen receptor modulator tamoxifen which shows high activity on estrogen receptor positive and negative cell lines.[12,13]

Thiosemicarbazones are versatile redox non-innocent ligands with a wide range of coordination modes in metal complexes, in particular when their binding capacity is further increased by condensation with an aldehyde or ketone containing an additional donor atom in a suitable position for chelation.[14] Beside their exciting coordination chemistry, thiosemicarbazones have evoked considerable interest because of their broad spectrum of pharmacological activity. In particular, α-*N*-heterocyclic thiosemicarbazones were found to possess antitumor, antimalarial, antibacterial, antifungal and antiviral activity.[15] The enzyme ribonucleotide reductase (RR) has been identified as the principal molecular target.[16]

Ribonucleotide reductase converts ribonucleotides to deoxyribonucleotides necessary for DNA synthesis and is highly expressed in tumor cells making it a suitable and well established target in cancer chemotherapy.[17] Initially, the inhibition of RR was attributed to the ability of thiosemicarbazones as strong chelators to remove iron from the enzyme active site, but later it was found that preformed iron chelates of some thiosemicarbazones with a terminal NH_2 group ($^4NH_2$) show higher RR inhibitory activity than the uncomplexed thiosemicarbazones.[1820] This is in agreement with data of 3-aminopyridine-2-carboxaldeyde thiosemicarbazone (*Triapine*®), an investigational drug currently in phase II clinical trials,[21] where an increase in cytotoxicity upon coordination to iron was reported.

We reported previously that in the presence of the reductant dithiothreitol (DTT) iron(III) complexes with ^4N-disubstituted α-N-heterocyclic thiosemicarbazone ligands show the fastest destruction of the R2 specific tyrosine free radical in mouse RR followed by the metal-free ligands and the corresponding gallium(III) complexes.[22] In the absence of DTT no radical quenching was observed, and the cytotoxicity data for the same compounds tested in the cancer cell lines 41M (ovarian carcinoma) and SK-BR-3 (mammary carcinoma) are in reversed order: the gallium complexes exhibited slightly higher cytotoxicity in the low nanomolar range in comparison to the metal-free ligand, whereas the iron(III) complexes displayed a much lower cytotoxicity in the micromolar range. Thus, iron is essential for the fast quenching of the tyrosyl radical in RR, but it is not solely responsible for the antitumor potency of the ^4N-disubstituted thiosemicarbazone derivatives suggesting the existence of additional molecular targets. The requirement of an adequate reductant (*e.g.*, DTT) for successful radical quenching indicates that the iron(III) complex is reduced to its iron(II) form prior radical quenching. Similar observations were reported previously for *Triapine*[23] and other thiosemicarbazones.[19,20]

These findings prompted us to prepare a series of gallium(III), iron(III) and ruthenium(III) complexes of the general formula $[ML_2][Y]$ (M = Ga, Fe and Ru; Y = PF_6^- or $FeCl_4^-$), where HL is a chalcogensemicarbazone ligand (Chart 1 and 2) and to investigate the effect of coordination to the metal on their metal- and ligand-centered redox properties by carrying out detailed electrochemical investigations and quantum chemical calculations. We were particularly interested to clarify if the redox properties/potentials of the prepared

compounds are of physiological relevance, *i.e.*, to elucidate whether a relation between their electrochemical properties and antiproliferative activity or R2 specific tyrosine free radical quenching ability can be found.

Chart 1. The chalcogensemicarbazone ligands used in this study

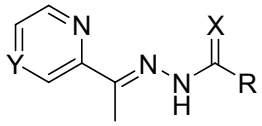

HL^{A} : X = S, Y = CH, R = $N(C_4H_8)$ (**A**)
HL^{B}: X = S, Y = CH, R = $N(CH_3)_2$ (**B**)
HL^{C}: X = S, Y = CH, R = $NH(C_6H_5)$ (**C**)
HL^{D}: X = S, Y = CH, R = $NH(p\text{-}C_6H_4NO_2)$ (**D**)
HL^{E}: X = S, Y = N, R = $N(C_4H_8)$ (**E**)
HL^{F}: X = S, Y = N, R = $N(C_5H_{10})$ (**F**)
HL^{G}: X = S, Y = N, R = $N(CH_3)_2$ (**G**)
HL^{H}: X = S, Y = N, R = $NH(C_6H_5)$ (**H**)
HL^{I}: X = S, Y = N, R = $NH(p\text{-}C_6H_4NO_2)$ (**I**)
HL^{J}: X = O, Y = CH, R = $N(CH_3)_2$ (**J**)
HL^{K}: X = Se, Y = CH, R = $N(CH_3)_2$ (**K**)

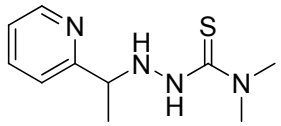

HL^{M} (**M**)

Chart 2. The library of metal chalcogensemicarbazonate complexes

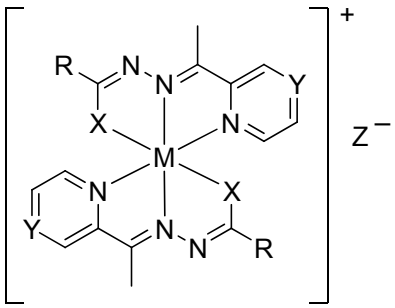

[ML2][Z]

M = Ga, L = L^A, Z = PF_6 (1A)

M = Ga, L = L^B, Z = PF_6 (1B)

M = Ga, L = L^C, Z = PF_6 (1C)

M = Ga, L = L^D, Z = NO_3 (1D)

M = Ga, L = L^E, Z = PF_6 (1E)

M = Ga, L = L^F, Z = PF_6 (1F)

M = Ga, L = L^G, Z = PF_6 (1G)

M = Ga, L = L^H, Z = NO_3 (1H)

M = Ga, L = L^I, Z = NO_3 (1I)

M = Ga, L = L^J, Z = PF_6 (1J)

M = Ga, L = L^K, Z = PF_6 (1K)

M = Fe, L = L^A, Z = PF_6 (2A)

M = Fe, L = L^B, Z = PF_6 (2B)

M = Fe, L = L^C, Z = PF_6 (2C)

M = Fe, L = L^D, Z = NO_3 (2D)

M = Fe, L = L^E, Z = PF_6 (2E)

M = Fe, L = L^F, Z = PF_6 (2F)

M = Fe, L = L^G, Z = PF_6 (2G)

M = Fe, L = L^H, Z = NO_3 (2H)

M = Fe, L = L^I, Z = NO_3 (2I)

M = Fe, L = L^A, Z = $FeCl_4$ (2'A)

M = Fe, L = L^B, Z = $FeCl_4$ (2'B)

M = Fe, L = L^E, Z = $FeCl_4$ (2'E)

M = Fe, L = L^F, Z = $FeCl_4$ (2'F)

M = Fe, L = L^G, Z = $FeCl_4$ (2'G)

M = Ru, L = L^B, Z = PF_6 (3B)

V.3. Electrochemical Studies

V.3.1. Ligand-Centered Reduction.

The electrochemical data for the metal complexes and ligands under study are summarized in Table 1 and Table S1, respectively, and their electrochemical behavior is shown in Scheme 1. In general, all complexes show several redox waves attributable to the reduction of the non-innocent thiosemicarbazone ligands at lower potentials (< –0.4 V *vs*. NHE) than the metal-centered redox waves for the iron and ruthenium complexes (> 0 V *vs*. NHE; see below). The cyclic voltammograms of 0.20 M [*n*-Bu_4N][BF_4]/CH_3CN solutions of the gallium thiosemicarbazonate complexes **1A**–**1I** display two consecutive reversible one-electron (as confirmed by controlled potential electrolysis of **1B**) redox waves with ${}^{ox}i_p$ /${}^{red}i_p$ = 1.0 at v > 50 mV/s with ΔE_p = 60 – 70 mV at 0.20 V/s (Scheme 1a, Figure 1). The redox potential of the first ligand reduction (wave ${}^{I}L^{red}$) occurs between –0.38 and –0.96 V, and the second (wave ${}^{II}L^{red}$) between –0.62 and –1.25 V *vs.* NHE depending on the ligand identity (Table 2). As expected, complex **1A** with the 2-pyridinyl and 4-pyrrolidinyl substituents at the thiosemicarbazone ligands shows the most negative redox potentials, whereas complex **1I** with the more electron–withdrawing moieties *p*-nitroanilinyl and 2-pyrazinyl (the latter being weaker σ-donor and stronger π-acceptor than the 2-pyridinyl moiety) has the most positive redox potential for the ligand centered reductions. After these two consecutive reversible reduction processes a third irreversible redox wave ${}^{III}L^{red}$ is observed for the pyridinyl complexes **1A** – **1C** between –1.63 and –1.81 V *vs*. NHE, whereas wave ${}^{III}L^{red}$ is a reversible one-electron reduction process at –1.35 and –1.56 V *vs*. NHE for the pyrazinyl containing complexes **1E** – **1H** and is followed by a fourth partial quasi-reversible one-electron reduction wave, ${}^{IV}L^{red}$, at *ca.* –1.80 V *vs*. NHE (ΔE_p = 100–150 mV) (Figure 2a). For complex **1H** this fourth reduction wave is irreversible because it overlaps with a further wave at *ca.* –1.95 V *vs*. NHE. Waves ${}^{III}L^{red}$ and ${}^{IV}L^{red}$ were not detected for **1D** and **1I**, both containing a nitro-group attached to the thiosemicarbazone ligand, but instead a quasi-reversible (ΔE_p = 90–100 mV) reduction of the NO_2 group[24] at $E_{1/2}$ = –1.04 and –1.01 V *vs.* NHE was observed, respectively. Complexes with nitro-derivatives are scarcely soluble in

CH_3CN and were therefore measured in 0.20 M [*n*-Bu_4N][BF_4]/DMF. However, no variations in redox properties/potentials of the complexes have been observed in DMF or CH_3CN electrolyte solutions as established for complex **2D**.

Table 1. Summary of the Electrochemical Data for the Metal Complexes

Gallium complexes					
			$E_{1/2}$ / $^{I}L^{red}$	$E_{1/2}$ / $^{II}L^{red}$	$E_{1/2}$ / $^{III}L^{red}$
1A			–0.96	–1.25	–1.81[c,e]
1B			–0.93	–1.22	–1.77[c,e]
1C			–0.79	–1.05	–1.63[c]
1D[b]			–0.70[c]	–0.84[c]	N/A[f]
1E			–0.60	–0.88	–1.56
1F			–0.58	–0.84	–1.49
1G			–0.58	–0.85	–1.51
1H			–0.46	–0.72	–1.35
1I[b]			–0.38[d]	–0.62[d]	N/A[f]
1J			–1.03	–1.34	–2.04[c]
1K			–0.94	–1.22	–1.73[c,e]
Iron complexes					
	$E_{1/2}$ / $^{C}Fe^{red}$	$E_{1/2}$ / $^{A}Fe^{red}$	$E_{1/2}$ / $^{I}L^{red}$	$E_{1/2}$ / $^{II}L^{red}$	E_p / $^{III}L^{red}$
2A	0.06	–	–1.62[d]	–2.01[c,g]	–2.01[c,g]
2B	0.08	–	–1.61[d]	–1.99[c,g]	–1.99[c,g]
2C	0.18	–	–1.44[d]	–1.72[d]	–2.15[c,e]
2D[b]	0.27	–	N/A[f]	N/A	N/A
2E	0.32	–	–1.23	–1.65	–2.12[c,e]
2F	0.32	–	–1.21	–1.64	–2.09[c,e]
2G	0.34	–	–1.22	–1.64	–2.13[c,e]
2H	0.43	–	–1.08	–1.47	–1.97[c,e]
2I[b]	0.51	–	N/A[f]	N/A	N/A
2'A	0.06	0.30	–1.60[c]		
2'B	0.08	0.30	–1.61[d]		
2'E	0.31[g]	0.31[g]	–1.20[c]		
2'F	0.31[g]	0.31[g]	–1.21[d]		
2'G	0.32[g]	0.32[g]	–1.22[d]		
Ruthenium complex					
	$E_{1/2}$ / $Ru^{III/II}$	$E_{1/2}$ / $Ru^{IV/III}$	$E_{1/2}$ / $^{I}L^{red}$	E_p / $^{II}L^{red}$	E_p / $^{III}L^{red}$
3B	+0.21	+1.27	–1.56	–2.00[c,g]	–2.00[c,e,g]

a) Potentials in V ± 0.01 *vs*. NHE in 0.20 M [*n*-Bu_4N][BF_4]/CH_3CN; b) measured in 0.20 M [*n*-Bu_4N][BF_4]/DMF; c) for the irreversible wave, the E_p values are given; d) $^{ox}i_p$ / $^{red}i_p$ between 0.6 and 0.8 at 0.2 V/s; e) two or multi electron process (see text); f) for complexes with nitro-containing ligands, the reduction of this group at *ca*. –1.0 V *vs.* NHE prevented the detection of further ligand-centered redox waves (see text); g) could not be detected as separate waves.

Scheme 1. Schematic overview of the electrochemical behavior of the studied Ga (a), Fe (b) and Ru (c) complexes

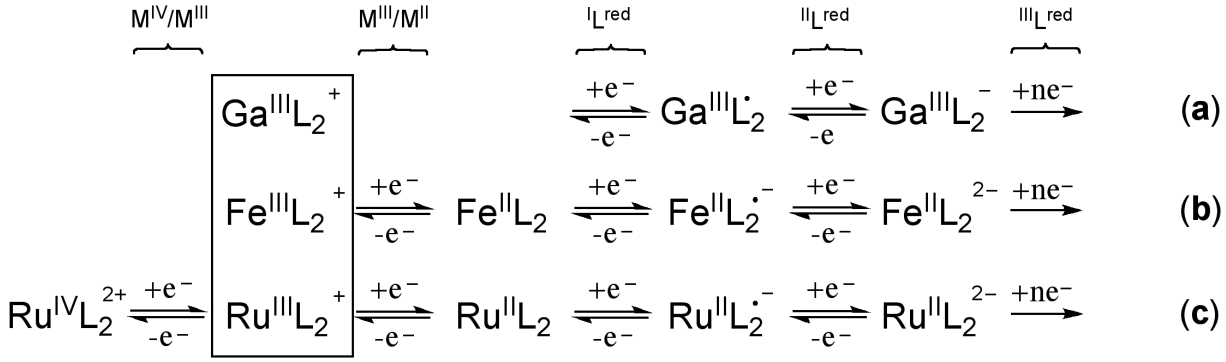

Figure 1. Cyclic voltammograms of (a) **1A** and (b) **1F** in CH_3CN containing 0.20 M [*n*-Bu_4N][BF_4] at a scan rate of 0.20 V s^{-1} using a platinum working electrode. Square wave voltammograms (SWVs; c) of 1.0 mM **1A** (black line) and **1F** (gray line) electrolyte solutions were measured with 2 mV step height, 25 mV pulse and 100 Hz frequency. The solid line on the bottom right refers to the current (10 μA) for a–c. For the assignment of waves, see text

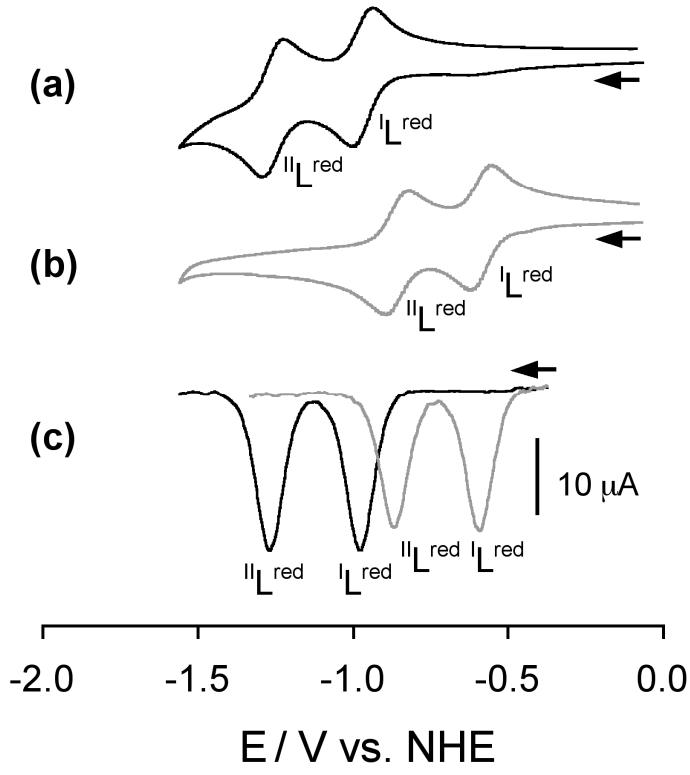

The influence of the chalcogen atom X of the chalcogensemicarbazone ligands (Chart 1) on the redox potential was studied with complexes **1B**, **1J** and **1K**, which contain a sulfur, oxygen or selenium atom, respectively. Complex **1J** (X = O) displays the lowest reduction potentials at –1.03 and –1.34 V *vs.* NHE for $^{I}L^{red}$ and $^{II}L^{red}$, respectively, whereas **1K** (X = Se) and **1B** (X = S) have a similar redox potential at –0.94 to –0.93 and –1.22 V *vs.* NHE for the corresponding redox waves. Thio- and selenosemicarbazone ligands are known to have comparable NMR spectra,[25] and the gallium complexes **1B** and **1K** also possess similar ^{1}H and ^{13}C NMR chemical shifts with the largest deviation in the ^{13}C NMR spectra of the C–X resonance (detected at 176.1 and 173.8 ppm, respectively).[22,26] Complex **1J** shows a considerably different spectrum with the C–X resonance at 167.1 ppm and strong high field shifts for both carbon resonances at the CH_3C=N moiety (**1B**: 14.9, 149.0 ppm; **1K**: 15.6, 147.4 ppm; **1J**: 12.6, 139.3 ppm); in accordance with the lower redox potential of complex **1J** (see below).

The ligand-centered reduction of **2A**–**2I** at the iron(II) center (for $Fe^{III} \rightarrow Fe^{II}$ process see below) is similar to the gallium analogues, although the corresponding redox potentials $^{I}L^{red}$ and $^{II}L^{red}$ are considerably more negative between –1.08 and –1.62 V, and –1.47 and –2.01 V *vs.* NHE, respectively (Scheme 1b, Figure 2b, Table 1). In the case of **2A** and **2B** the wave $^{II}L^{red}$ at –2.01 and –1.99 V *vs.* NHE overlaps with $^{III}L^{red}$ resulting in two indistinguishable redox waves. Complexes **2C**–**2H** are reduced at $^{III}L^{red}$ between –1.97 and –2.15, close to the solvent cut-off potential. The much lower redox potentials of the iron(II) complexes in comparison to the gallium(III) complexes can be explained at least partially by the different charges of the complexes. The uncharged iron(II) posses a higher electron density and is therefore harder reducible than the positively charged gallium(III) complex. For the nitro group containing complexes **2D** and **2I** only one irreversible reduction wave at –0.97 V and –0.93 V *vs.* NHE was detected which can be attributed to the reduction of the nitro group. This is only slightly shifted to more positive potential compared to that in the analogous gallium complexes. The presence of the tetrachloridoferrate counteranion in **2'A**–**2'G** prevented the accurate detection of the second reduction wave $^{II}L^{red}$ in these complexes, because the counteranion reacts readily with the ligand radical formed upon reduction at $^{I}L^{red}$.

The ruthenium complex **3B** shows the first ligand reduction at $E_{1/2}$ = –1.56 V *vs.* NHE (Scheme 1c, Figure 2c), whereas $^{II}L^{red}$, like for the pyridine containing iron complexes **2A** and **2B**, overlaps with $^{III}L^{red}$ resulting in an irreversible reduction wave at –2.00 V (Figure 3).

Figure 2. Cyclic voltammograms of **1G** (a), and **2E** (b), and **3B** (c) in CH_3CN containing 0.20 M [*n*-Bu_4N][BF_4] at a scan rate of 0.20 V s^{-1} using a glassy carbon working electrode, displaying the ligand (L^{red}), the Fe^{III}/Fe^{II} ($^{C}Fe^{red}$), and the Ru^{III}/Ru^{II} and Ru^{IV}/Ru^{III} redox couples

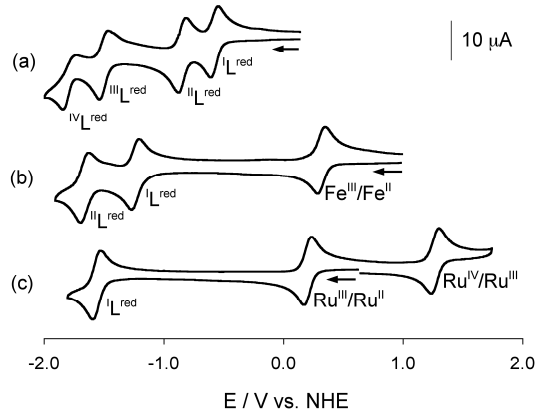

Figure 3. Cyclic voltammogram of **3B** in CH_3CN containing 0.20 M [*n*-Bu_4N][BF_4] at a scan rate of 0.20 V s^{-1} using a glassy carbon working electrode

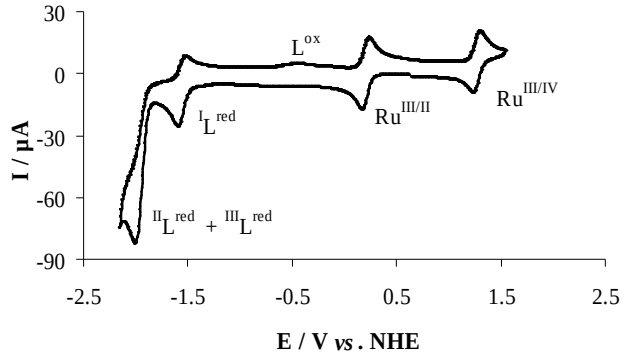

Increasing electron donor properties of substituents are known to increase the effective negative net charge on the corresponding compounds and result usually in a decrease of their redox potentials. Plotting the pK_a values of the attached amine moieties [dimethylamine (10.73), pyrrolidine (11.31), piperidine (11.12), aniline (4.87) and *p*-

nitroaniline (1.02)][27] *vs.* $E_{1/2}$ results in a linear relationship (Figure 7). By using the resultant linear equations (see caption of Figure 4 for the equations of $Fe^{III} \rightarrow Fe^{II}$ and $^{I}L^{red}$) and the pK_a values of the attached amine moieties the redox potentials of novel synthesized 2-acetylpyridine(pyrazine) thiosemicarbazone gallium(III) and iron(III) complexes in CH_3CN solution can be predicted. The increased redox potential of complexes containing a pyrazine (**1E**–**1I**, **2E**–**2I**) instead of a pyridine (**1A**–**1D**, **2A**–**2D**) moiety can also be rationalized by the increased net donor properties of the latter [E_L(pyridine) = 0.25 V, E_L(pyrazine) = 0.33][9] and the different pK_a-values [pK_a(pyrazine) = 0.65, pK_a(pyridine) = 5.23], respectively.[27]

Figure 4. Plot of pK_a values of attached amine moieties on thiosemicarbazone ligands *vs.* ligand- and metal-centered $E_{1/2}$ values for the gallium (**1A**–**1I**, top) and iron (**2A**–**2I**, bottom) complexes. For the complexes **2D** and **2I** the reduction of the nitro group prevented the detection of the ligand reductions. $^{C}Fe^{red} = Fe^{III}/Fe^{II}$ redox couple of complex cation; L^{red} = ligand-centered reduction; thiosemicarbazonate complexes with pyrazine or pyridine moieties are shown separately and indicated with pz or py, respectively. Linear equations: Gallium complexes: $^{I}L^{red}$ (pz): E (V) = –0.3592 – 0.0206pK_a (r = 0.996); $^{I}L^{red}$ (py): E (V) = –0.6726 – 0.0247pK_a (r = 0.997). Iron complexes: $Fe^{III} \rightarrow Fe^{II}$ (pz): E (V) = 0.5244 –0.018pK_a (r = 0.995); $Fe^{III}/\rightarrow Fe^{II}$ (py): E (V) = 0.2847 – 0.0197pK_a (r = 0.995); $^{I}L^{red}$ (pz): E (V) = –0.9692 – 0.0227pK_a (r = 0.998); $^{I}L^{red}$ (py): E (V) = –1.3021 – 0.0284pK_a (r = 0.999)

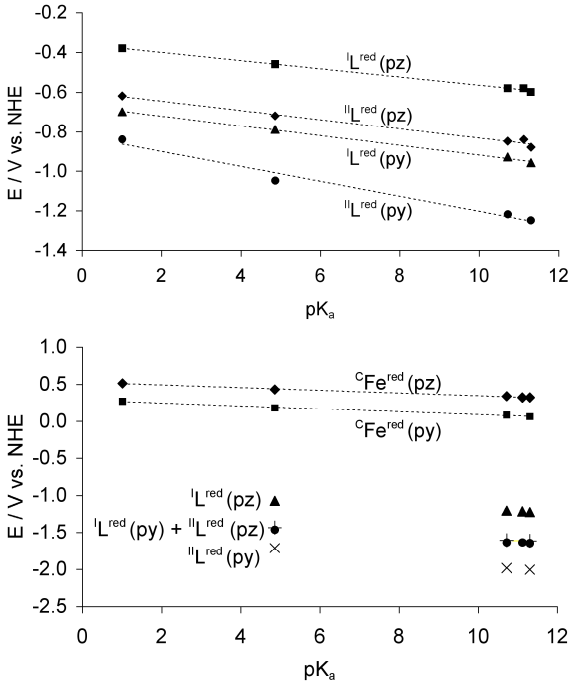

The metal-free thiosemicarbazone ligands **A–I** exhibit an irreversible reduction response at –1.01 to –1.47 V *vs.* NHE (Table S1). The second reduction wave could only be observed occasionally and was hardly reproducible indicating the instability of the radical formed after the first reduction process. For the *p*-nitrophenyl ligands **D** and **I** a quasi-reversible nitro reduction wave was detected at –1.04 and –1.03 V *vs.* NHE, respectively.[24] In agreement with the remote position of the nitro group in the ligands, these potentials are only slightly more negative than those of the corresponding ligands in the gallium and iron complexes. In addition, an irreversible pre-wave was observed at E_p = –0.82 and –0.80 V *vs.* NHE, respectively, which was also reported for *o*-nitrotoluene and *m*-nitrotoluene in aprotic solvents.[28] In contrast to the ligand centered reduction of the metal complexes where all ligands are forced to adopt the same configuration, the metal-free ligands are present as different isomers in solution, therefore showing no conclusive correlation between the E_p and pK_a values of the amine moieties of the ligand. In particular, for ligand **B** three different isomers were found in DMSO solution,[26] two of them with strong intramolecular hydrogen bonds, whereas ligand **H** in the same solvent did not undergo any isomerization (see NMR data). The metal-ion stabilizes the reduced ligand radicals preventing their decomposition in the time-scale of cyclic voltammetry and allowing for the observation of two or three reversible ligand-centered redox waves upon coordination. The gallium-complexes are reduced at ~0.3–0.8 V more positive redox potential than the uncoordinated ligands, whereas the same ligand centered reductions in the iron(II)- and ruthenium(II)-ions occur at ~0.0–0.4 V more negative redox potentials than in the metal-free thiosemicarbazones. Therefore complexation to different metal ions strongly influences the ligand centered redox potentials which offers the possibility to specifically shift the redox potentials into the physiologically accessible range.

V.3.2. Metal-Centered Redox Processes.

The cyclic voltammograms of the iron complexes **2A**–**2I** (Figure 5a, Table 1) display one reversible single-electron reduction wave, $^{C}Fe^{red}$, at 0.06 to 0.51 V *vs*. NHE, which is assigned to the $Fe^{III} \rightarrow Fe^{II}$ process of the cationic complex ($^{ox}i_p$ /$^{red}i_p$ = 1.0 for v > 0.05 V/s with ΔE_p = 0.60 – 0.70 V at 0.2 V/s). As observed for the ligand-centered redox behavior, an increasing net electron-donor character correlates with a decrease in redox potential. The

correlation of pK_a values with redox potentials for the coordinated thiosemicarbazone ligands also holds true for the iron-centered redox couples (Figure 4). Whereas complexes **2A**–**2I** showed only one reduction wave (Figure 5a), the analogous complexes **2'A**–**2'G** displayed a second wave at 0.31±0.01 V *vs*. NHE, which is attributed to the reduction of the tetrachloridoferrate anion, $^{A}Fe^{red}$ (Figure 5b). Wave $^{A}Fe^{red}$ overlaps in **2'E–2'G** with the reduction wave of the complex cation, and could not be resolved by CV or SVW scans, indicating that a set of two tridentate ligands **E – G** acts as a net electron-donor as strong as four tetrahedrally coordinated chlorido ligands. The current height in **2'E–2'G** (same concentration and experimental conditions) was approximately two-fold compared to **2E–2G** as confirmed by cyclic voltammetry (Figure 5c). Square wave voltammetry revealed that the unresolved wave in **2'E - 2'G** arises from an overlap of the Fe^{III}/Fe^{II} waves of the cationic iron-complex and the tetrachloridoferrate anion indicating the two-electron nature of this reduction wave, one from the reduction of the complex cation and one from the tetrachloridoferrate anion (Figure 5). The two-electron nature of the overlapped redox wave from **2'E - 2'G** was confirmed by controlled potential electrolysis of **2'F** at 0.14 V *vs.* NHE.

The ruthenium(III) complex shows two reversible metal centered redox waves with the first one at +0.21 V for the $Ru^{III}\rightarrow Ru^{II}$ redox couple and the second at +1.27 *vs.* NHE attributable to the $Ru^{III}\rightarrow Ru^{IV}$ redox process (Figure 2c). The 1.06 V difference for the Ru^{III}/Ru^{II} and Ru^{IV}/Ru^{III} redox couple is narrow compared to the commonly observed separation of these two redox waves of *ca.* 1.6 V for ruthenium complexes with octahedral coordination sphere in non-aqueous solvents.[29] However, this difference can be explained by the distortion of the octahedral geometry by the tridentate thiosemicarbazonate ligands, which makes direct comparisons with other sterically non-constrained complexes difficult.

Figure 5. Cyclic voltammograms (top) and square wave voltammograms (bottom, 2 mV step height, 25 mV pulse, 100 Hz frequency) of (a) **2A** (black), (b) **2'A** (gray), (c) **2'E** (black) in 0.20 M [*n*-Bu_4N][BF_4]/CH_3CN at a scan rate of 0.20 V s^{-1} by using a platinum working electrode. $^{C}Fe^{red}$ indicates the metal-centered reduction of the cathodic complex, and $^{A}Fe^{red}$ the reduction of the $[FeCl_4]^-$ counteranion

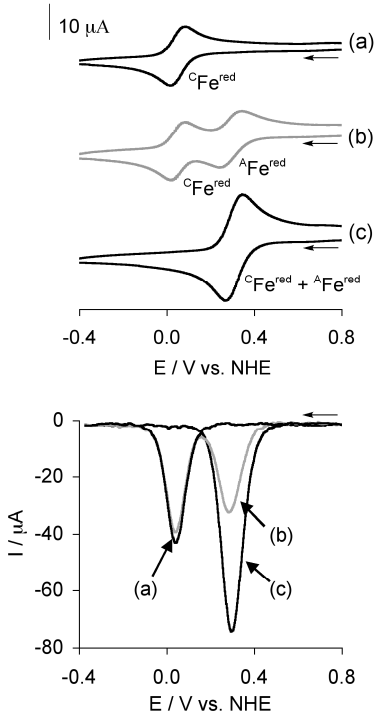

V.3.3. Location of Reduction Site.

Most of the literature dealing with electrochemical properties of α-*N*-heterocyclic thiosemicarbazone complexes are exclusively focused on the metal centered redox reactions,[3033] neglecting the ligand centered redox processes. If reductions are described which are associated with the ligand, the position where reduction takes place in the thiosemicarbazone moiety is either undefined[3436] or changes between the thione portion,[37] the azomethine part[38,39] or both of them,[40] whereas no further studies are described to support these assumptions. Detailed investigations on the reduction pathway were performed for the metal-free 2-formylpyridine thiosemicarbazone in methanol.[41] The data showed that the ligand will be first protonated at the azomethine nitrogen then cleaved at the N–N bond forming thiourea and the 2-pyridinemethaniminium ion which is then further reduced to

protonated 2-picolylamine. Two other reduction mechanisms were excluded in this study namely the reduction at the pyridine ring resulting in dihydropyridine and the formation of the thiol by reduction of the C=S double bond. The direct reduction of the azomethine bond is not discussed, but was already described 20 years before for the same ligand in water.[42] There is only one publication dealing with the metal ion influence on the redox potentials of a thiosemicarbazone ligand.[43] Although no reference electrode was reported, making a quantitative comparison impossible, the reported redox potentials of the perchlorate salt of the iron(III) complex **2B** and the ligand $\mathbf{HL^B}$ appeared at considerably different values for all reduction waves than observed in the present study. To the best of our knowledge this is the first detailed electrochemical study of the influence of metal ions on the redox properties of thiosemicarbazones and the influence of the chalcogen donor identity on the reduction processes.

There exist two possible locations, where the ligand-centered reduction of the complexes takes place: either at the C=N double bond of the 2-acetylpyridine moiety ($CH_3C=N$) or at the C=N double bond in close proximity to the chalcogen atom. Comparing the ^{13}C NMR data of the gallium complexes **1A** – **1I** with the $E_{1/2}$ redox potentials a good correlation can be found for both carbon resonance of the $CH_3C=N$ moiety (Figure 6 and Figure 7); an increasing redox potential at $^{I}L^{red}$ and $^{II}L^{red}$ correlates with enhanced electronic deshielding resulting in lower-field chemical shifts for the corresponding ^{13}C nucleus. In contrast no correlation could be found for the C–S resonance (**1A**: 172.9 ppm; **1B**: 176.1 ppm; **1C**: 172.5 ppm; **1D**: 172.4 ppm). Therefore, we suppose that the one-electron ligand-centered reduction site is located at the 2-acetylpyridine C=N bond. This is in agreement with quantum chemical calculations (see below) and the chemical reduction of this C=N bond for the metal-free and coordinated ligands. Addition of $NaBH_4$ to an ethanolic solution of ligand $\mathbf{HL^B}$ resulted in the reduction of the C=N bond and the formation of ligand $\mathbf{HL^M}$ which exhibits its first reduction wave only at –2.10 V *vs.* NHE. Similarly, reduction of the nitrate salt of **1B** (obtained by precipitation with diethyl ether prior to the addition of ammonium hexafluorophosphate) with $NaBH_4$ yielded a product containing the uncoordinated reduced ligand $\mathbf{HL^M}$ in around 50 % yield.

Figure 6. Plot of $\delta(^{13}C{=}N)$ of the $CH_3C{=}N$ moiety *vs.* $E_{1/2}$ of complexes **1A–1H**

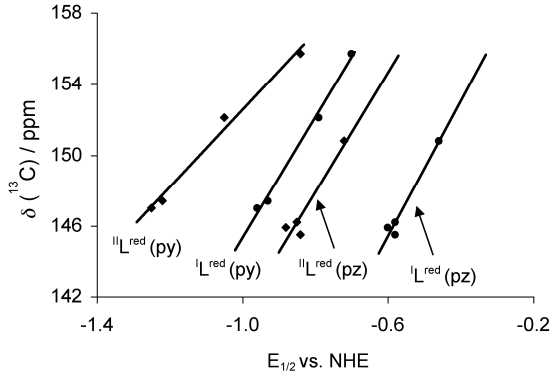

Figure 7. Plot of $\delta(^{13}CH_3)$ of the $CH_3C{=}N$ moiety *vs.* $E_{1/2}$ of complexes **1A–1H**

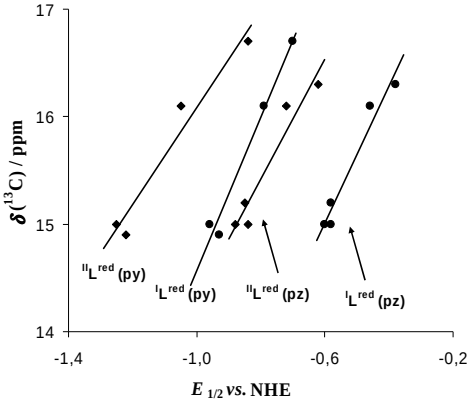

V.4. Quantum Chemical Studies.

Density functional calculations were performed to elucidate (*i*) why the ligand centered reductions of the iron(II) complexes $[Fe^{II}(\mathbf{L})_2]$ (formed by reduction of the iron(III) complex $[Fe^{III}(\mathbf{L})_2]^+$) have a *lower* standard reduction potential (SRP) than the non-metalated thiosemicarbazones (**HL**) and (*ii*) to locate the site of reduction at the thiosemicarbazone ligands. The reduction of a compound should be strongly facilitated by forming a complex with a dicationic metal ion, which should have been reflected by a considerably *higher* redox potential. The one-electron-reduction events involving the species, $(\mathbf{L^B})^-$, $\mathbf{HL^B}$, $[Ga(\mathbf{L^B})_2]^+$

and $[Fe^{II}(\mathbf{L}^{\mathbf{B}})_2]$, yielding their reduced forms, $(\mathbf{L}^{\mathbf{B}})^{2-}$, $(\mathbf{HL}^{\mathbf{B}})^{-}$, $[Ga(\mathbf{L}^{\mathbf{B}})_2]$ and $[Fe^{II}(\mathbf{L}^{\mathbf{B}})_2]^{-}$, respectively, have been investigated and compared. Note that the *deprotonated* species $(\mathbf{L}^{\mathbf{B}})^{-}$ shall serve as the intuitive reference compound in our calculations, as the reduction potential of $(\mathbf{L}^{\mathbf{B}})^{-}$ may be controlled by either protonation ($\mathbf{HL}^{\mathbf{B}}$) or metalation ($[Ga(\mathbf{L}^{\mathbf{B}})_2]^{+}$ and $[Fe^{II}(\mathbf{L}^{\mathbf{B}})_2]$). Table 2 shows an excellent agreement of our calculated and experimental SRPs, validating the computational approach employed for this study.

Table 2. Calculated and experimental standard redox potentials (SRP, in V *vs.* NHE), Hirshfeld partial charges in the oxidized and reduced forms, and LUMO energy level of the oxidized species (E_{LUMO}, in eV)

			partial charges						
	SRP		ox			red			
compound	calc	exp	M[a]	L1	L2	M[a]	L1	L2	E_{LUMO}
$(\mathbf{L}^{\mathbf{B}})^{-/2-}$	–1.65			–1.00			–2.00		1.14
$[Fe(\mathbf{L}^{\mathbf{B}})_2]^{0/-}$	–1.56	–1.61	0.02	–0.01	–0.01	0.02	–0.51	–0.51	–2.39
$(\mathbf{HL}^{\mathbf{B}})^{0/-}$	–1.15	–1.21	0.08	–0.08		0.08	–1.08		–3.00
$[Ga(\mathbf{L}^{\mathbf{B}})_2]^{+/-}$	–0.94	–0.93	0.32	0.34	0.34	0.32	–0.24	–0.08	–5.84

[a] H, Ga, and Fe, respectively

Figure 8 displays the predicted structures of the four species and their reduced forms. Only the isomers of $(\mathbf{L}^{\mathbf{B}})^{-}$ and $\mathbf{HL}^{\mathbf{B}}$ that are calculated to be most stable in acetonitrile solution are shown here, while all isomers and their relative free energies are given in Figure 9. The predicted bond lengths in $\mathbf{HL}^{\mathbf{B}}$ and $[Ga(\mathbf{L}^{\mathbf{B}})_2]^{+}$ are in good to excellent agreement with available X-ray crystallographic structures (Table S5). The calculations reveal structural changes in the entire compounds upon reduction. In the free ligand $(\mathbf{L}^{\mathbf{B}})^{-}$ (Figure 8, top), the C–S bond is elongated (+0.04 Å) upon reduction, the adjacent C=N bond is shortened (–0.04 Å), the N–N bond is elongated (+0.03 Å), the acetylpyridine C=N bond is elongated (+0.03 Å), the adjacent C–C bond is shortened (–0.04 Å), and the C=N bond in the pyridine is elongated (+0.04 Å). Similar structural changes occur when the protonated species HL^{B} is reduced (Figure 8). Upon reduction of $[Ga(\mathbf{L}^{\mathbf{B}})_2]^{+}$, such structural changes occur in one of the ligands (L1), whereas the distances in the second ligand (L2) do not change significantly (Table S5). In $[Fe^{II}(\mathbf{L}^{\mathbf{B}})_2]$, the structural changes occur in both ligands but to a lesser extent than those in L1 of $[Ga(\mathbf{L}^{\mathbf{B}})_2]^{+}$. The iron complex maintains its C_2 molecular symmetry upon one-electron reduction, as both ligands remain equivalent, whereas the gallium complex

becomes asymmetric. The reduction of the metal complexes is also accompanied by changes in the metal-ligand distances (Table 3). Both Ga–N bonds to L1 are significantly shortened (–0.09 Å each), while all other Ga-ligand bonds are elongated by up to 0.06 Å. In contrast, all Fe-ligand bond lengths are either elongated upon reduction or remain constant.

Figure 8. Calculated structures of the oxidized species $(L^B)^-$, HL^B, $[Ga(L^B)_2]^+$ and $[Fe^{II}(L^B)_2]$ (left) and their reduced forms (right). Bond lengths in Å

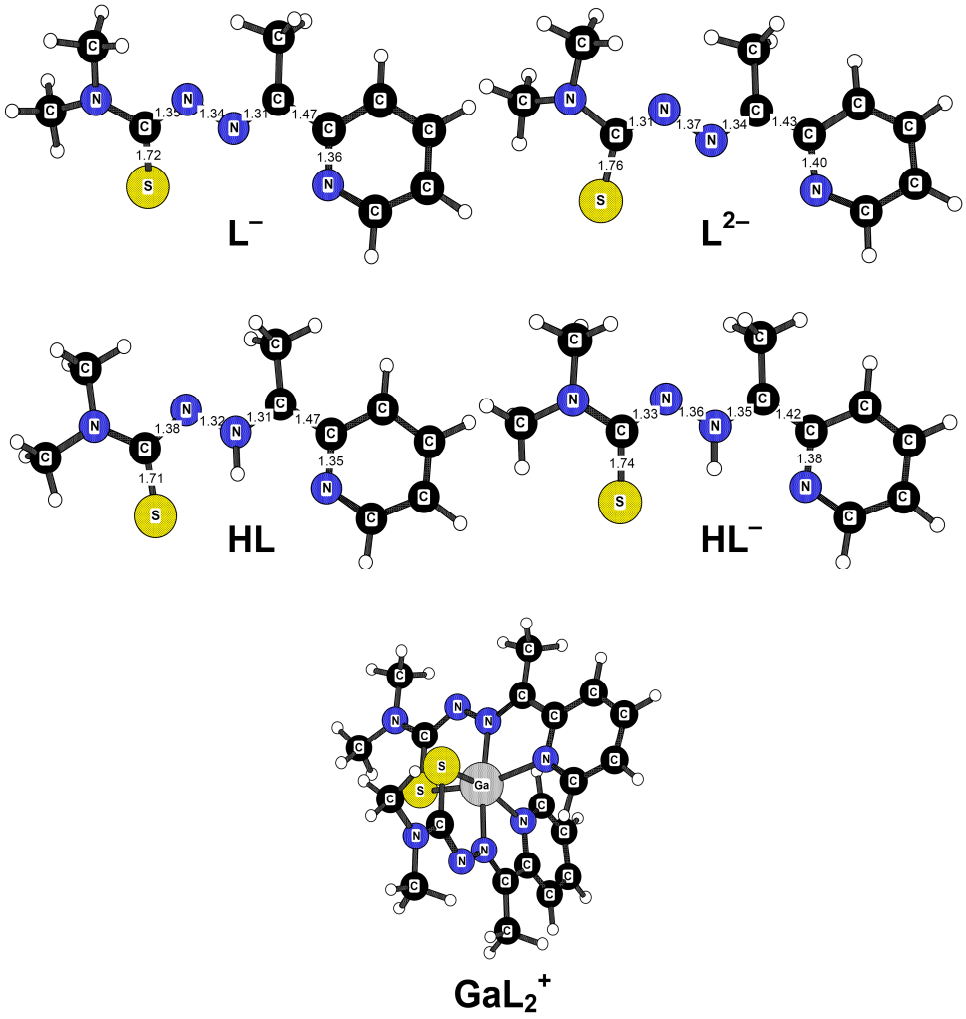

Figure 9. Calculated relative energies (in kcal/mol) of plausible isomers of 2-acetylpyridine *N*,*N*-dimethylthiosemicarbazone (**HL^{B}**) and its deprotonated form (**L^{B}**)$^{-}$ in acetonitrile

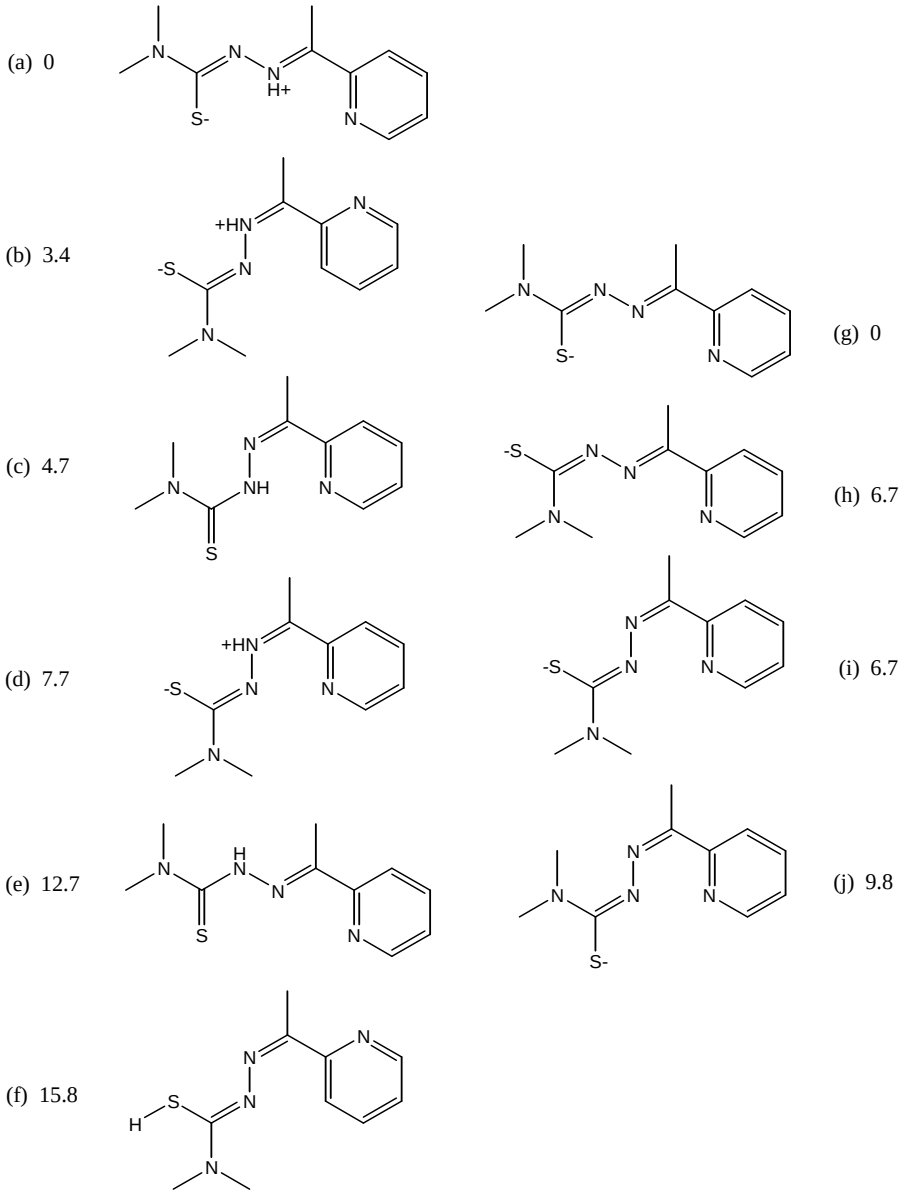

Table 3. Calculated metal-ligand bond lengths in Å

		metal–S		metal–N(N–N)		metal–	
compound	moiety	ox	red	ox	red	ox	red
[Ga(**L^{B}**)$_2$]$^{+/0}$	L1	2.39	2.43	2.09	2.00	2.18	2.10
	L2	2.39	2.45	2.09	2.15	2.18	2.21
[Fe(**L^{B}**)$_2$]$^{0/-}$	L1	2.36	2.39	1.94	1.94	1.99	1.99
	L2	2.36	2.39	1.94	1.94	1.99	1.99

Table 2 lists the electron-density-based Hirshfeld partial charges on the ligands, the metals, and the proton in the four species and their reduced forms. The calculated charges at the H, Fe, and Ga atoms in $\mathbf{HL^B}$, $[Fe^{II}(\mathbf{L^B})_2]$ and $[Ga(\mathbf{L^B})_2]^+$ are +0.08, +0.02, and +0.32, respectively, while the charge on each ligand is –0.08, –0.01, and +0.34, adding up to a total charge of 0, 0, and +1 in these compounds. Upon reduction, the charges at H, Fe, and Ga remain constant, while the additional electronic charge is distributed over the ligands. Equal charges on both ligands in the reduced iron complex, $[Fe^{II}(\mathbf{L^B})_2]^-$, but different charges on both ligands in the reduced gallium complex, $[Ga(\mathbf{L^B})_2]$, are consistent with the structural changes upon reduction and suggest that the one-electron reduction of the iron complex occurs on both ligands in a delocalized manner, whereas it occurs in the gallium complexes primarily on either ligand. Partial charges calculated using various other approaches are given in the Supporting Information (Table S4); note that the basis-function-based Mulliken partial charge on the Fe atom would change by –0.8 upon reduction, which would erroneously indicate a metal-centered reduction of the iron(II) complex.

Figure 10 displays the semi-occupied molecular orbital (SOMO) of the four reduced species $(\mathbf{L^B})^{2-}$, $(\mathbf{HL^B})^-$, $[Fe^{II}(\mathbf{L^B})_2]^-$, and $[Ga(\mathbf{L^B})_2]$. This orbital corresponds in each case to the lowest unoccupied orbital (LUMO) of the oxidized form (Figure 11). The LUMO energy levels of the oxidized species are also listed in Table 2 and correlate with the reduction potentials: the lower the LUMO energy, the easier the reduction. The SOMO of $(\mathbf{L^B})^{2-}$ and its conjugate acid $(\mathbf{HL^B})^-$ are very similar; they are distributed over the entire π system and have both bonding and antibonding character leading to the bond distance changes upon reduction (see above). For instance, as the SOMO of $(\mathbf{HL^B})^-$ has a bonding contribution to the C=N bond adjacent to the sulfur atom (marked with b in Figure 10), this bond is shortened when an electron occupies this orbital. The SOMO of $(\mathbf{HL^B})^-$ has an antibonding contribution to the C=N bond adjacent to the pyridyl group (marked with a in Figure 10), thus elongating this bond upon reduction. This result is consistent with the chemoselective hydrogenation of the latter C=N bond by $NaBH_4$ (see above). The SOMO of the reduced metal complexes show the same bonding and antibonding patterns as those in the SOMO of the free ligand. In the gallium complex, the SOMO is mainly distributed over either ligand. The asymmetric reduction with the strong shortening of the Ga–N bonds to either ligand maximizes the predominantly electrostatic interactions between the metal center and the reduced ligand. In contrast, the SOMO of the reduced iron complex is equally distributed over both ligands. It

contains a small fraction of a metal d orbital, which combines with the ligand orbitals in an antibonding fashion. Note that the Fe–N bond lengths change only insignificantly during reduction, indicating an enhanced Pauli repulsion between the ligand orbitals and the partially filled d shell in the reduced iron complex.

Figure 10. SOMO of the reduced species

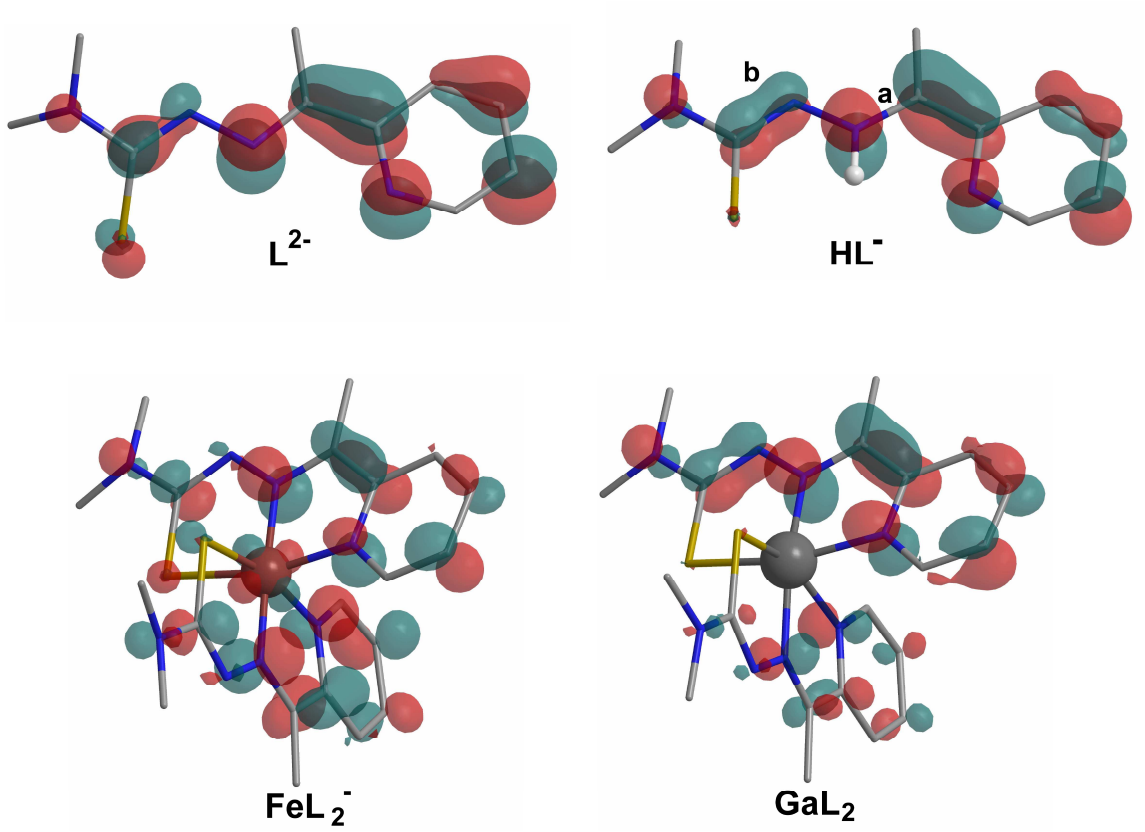

Figure 11. LUMO of the oxidized species $(\mathbf{L}^{\mathbf{B}})^{-}$, $\mathbf{HL}^{\mathbf{B}}$, $[Fe^{II}(\mathbf{L}^{\mathbf{B}})_2]$ and $[Ga(\mathbf{L}^{\mathbf{B}})_2]^{+}$

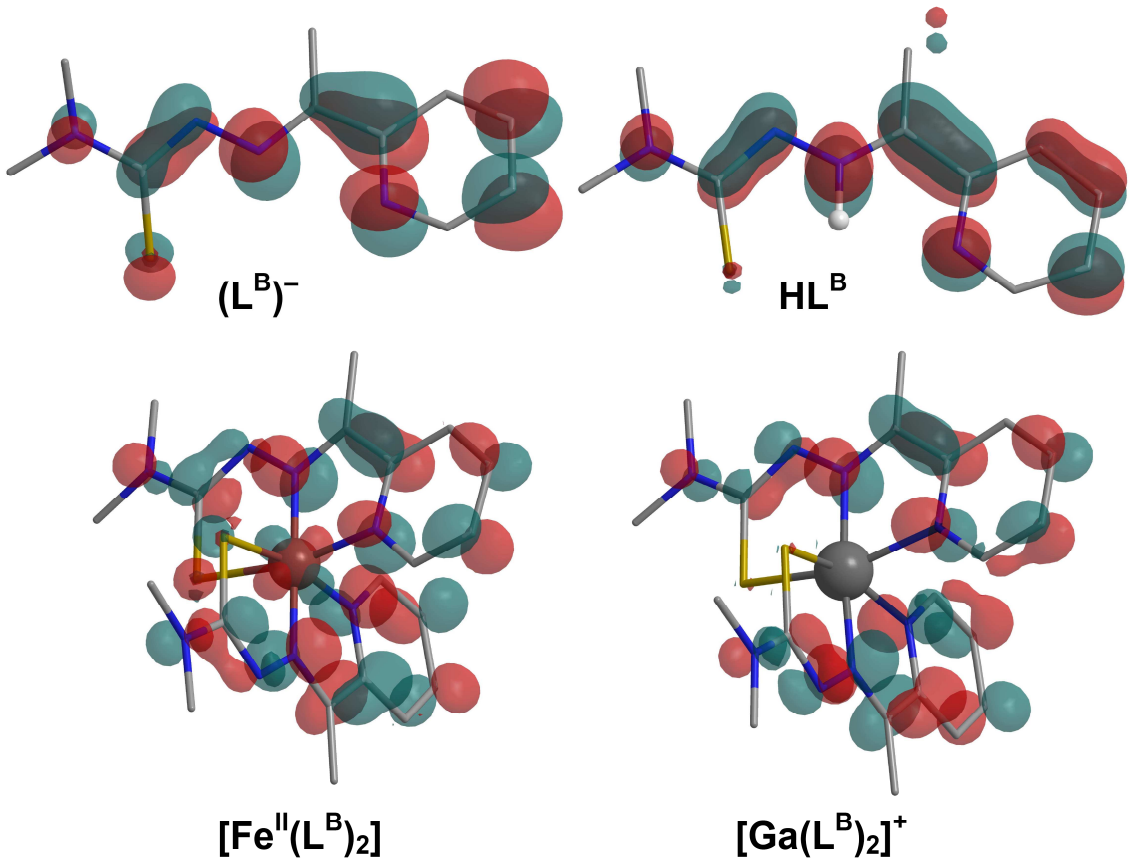

V.5. Computational Details.

The geometries of the deprotonated 2-acetylpyridine $^{4}N,^{4}N$-dimethylthiosemicarbazone ligand $(\mathbf{L}^{\mathbf{B}})^{-}$, its conjugated acid $\mathbf{HL}^{\mathbf{B}}$, the metal complexes $[Ga(\mathbf{L}^{\mathbf{B}})_2]^{+}$, $[Fe^{II}(\mathbf{L}^{\mathbf{B}})_2]$, and the reduced form of each of these species were optimized using the 3-parameter fit of exchange and correlation functionals of Becke[44a] (B3LYP), which includes the correlation functional of Lee, Yang, and Parr (LYP),[44b] as implemented in Gaussian 03.[45] The LANL2DZ effective core potentials (ECPs)[46] and the corresponding valence-basis sets were used on the metals and the 6-31G(d,p) basis sets were used on the other atoms. Vibrational frequencies calculated at this level confirm that all structures are minima on the potential energy surfaces. Improved energies were calculated by using a combination of the exchange functional of Becke[47a] and the correlation functional of

Perdew[47b] (BP86) together with the same ECPs and valence-basis set on the metal atoms but totally uncontracted and augmented with one set of f functions on Fe,[48] together with the 6-311+G(3d) basis set on the S atoms, and the 6-311+G(d,p) basis sets on the other atoms. Free energies in vacuo were calculated by adding corrections from unscaled zero-point energy (ZPE), thermal energy, work, and entropy evaluated at the B3LYP level at 298.15 K, 1 atm to the improved energies. Standard reduction potentials (SRPs) were calculated according to our previous approach,[49] which was carefully validated for the reduction of 61 ruthenium(III/II) complexes (bearing formal charges from 3+/2+ to 1–/2–) in four solvents and shall be readily transferable to other metal complexes, as the metal ion is not solvent-exposed in any of those Ru complexes. The SRP prediction is based on a thermodynamic cycle and involves the calculation of solvation free energies using the Poisson-Boltzmann finite element method[50] as implemented in Jaguar 7[51] with dielectric constant of 37.5 representing acetonitrile as the solvent. In the present work, the only difference to our previous SRP calculation approach[49] is the use of the BP86 functional for calculating improved energies, which leads to excellent agreement with experimental SRPs (see below) and was employed for similar purposes as well.[52a] The overestimation of the contribution of exchange energy by the B3LYP functional is well documented[52b] and may result in the overestimation of the stability of high-multiplicity spin states in iron complexes. A comparison of the relative energies of the electronic states of $[Fe^{II}(\mathbf{L}^{\mathbf{B}})_2]$ and $[Fe^{II}(\mathbf{L}^{\mathbf{B}})_2]^-$ and of the SRPs calculated using the BP86 and B3LYP improved energies is given in the Supporting Information (Table S2 and Table S3) and indicates that multireference approaches would be worth considering if permitted by the available computational resources. Other promising methods for this particular purpose include the spectroscopy oriented configuration interaction (SORCI) method and a ligand field theory (LFT)-based approach.[52c] Atomic partial charges at BP86 were calculated using the Mulliken[53a] scheme based on basis functions as implemented in Gaussian, the Hirshfeld[53b] scheme based on electron density as implemented in ADF,[54] and the ESP[53c] scheme of fitting atomic charges to reproduce the electrostatic potential in Jaguar.[51]

V.6. Conclusions

The electrochemical properties of a series of gallium-, iron-, and ruthenium-chalcogensemicarbazone complexes are investigated in detail. The electrochemical behavior of these complexes can be specified by (*i*) physiologically accessible metal-centered redox potentials for the iron(III) and ruthenium(III) complexes, (*ii*) formation of stable ligand radicals on the time-scale of cyclic voltammetry upon reduction of the non-innocent chalcogensemicarbazone ligands in aprotic solvents, (*iii*) quenching of these reductively induced ligand radicals by water, (*iv*) favorable shift of the ligand-centered redox potential in the physiologically accessible range for some gallium complexes when electron-withdrawing moieties are incorporated into the ligand, and (*v*) ligand-reduction for the gallium complexes occurs at the $CH_3C{=}N$ double bond. Quantum chemical calculations show that reduction of the coordinated and metal-free thiosemicarbazone ligands occurs at a π orbital that spreads over the entire thiosemicarbazone moiety with the reduction occurring on both ligands in the iron complex $[Fe^{II}(\mathbf{L^B})_2]$ and predominantly on either ligand in the gallium complex $[Ga(\mathbf{L^B})_2]^+$. The ligand-centered reductions $^{I}L^{red}$ and $^{II}L^{red}$ take place at 0.6–0.8 V more positive potentials for the gallium complexes than for the uncoordinated (protonated) ligands, which on the other hand are easier to reduce than the corresponding iron(II) complexes. The redox potentials increasing in the order $(\mathbf{L^B})^- < [Fe^{II}(\mathbf{L^B})_2] < \mathbf{HL^B} < [Ga(\mathbf{L^B})_2]^+$ correlate both with the calculated Hirshfeld partial charges on the thiosemicarbazone moieties in these compounds and with the energy levels of their LUMO, which becomes semi-occupied upon reduction. The intuitive assumption that the reduction of a compound is facilitated when it binds to a metal ion appears to be valid only if the *free ligand* $(\mathbf{L^B})^-$, in our case the thiosemicarabazonate, is considered as the reference compound, whereas a proton promotes the reduction of the thiosemicarbazone more strongly than does the iron(II) ion with its d^6 low-spin electron configuration.

V.7. Supporting Information

Table S1. Redox potentials[a] of the metal-free ligands $\mathbf{HL^A}$–$\mathbf{HL^M}$

Ligand	E_p / $^{I}L^{red}$
A	–1.26
B	–1.21
C[b]	–1.47
D[b]	N/A[c]
E	–1.06
F	–1.02
G	–1.01
H[b]	–1.31
I[b]	N/A[c]
J	–1.83
K	–1.13
M	N/A

a) Potentials in V ± 0.02 *vs*. NHE in 0.20 M [*n*-Bu_4N][BF_4]/CH_3CN; b) measured in 0.20 M [*n*-Bu_4N][BF_4] / DMF; c) for the nitro-containing ligands, only the reduction of this group at *ca*. –1.0 V *vs*. NHE and a pre-wave at *ca*. 0.80 V *vs*. NHE can be observed (see text).

Table S2. Comparison of standard reduction potentials (SRPs, in V vs. NHE) calculated at B3LYP and BP86

Compound	B3LYP	BP86	exp
$(\mathbf{L^B})^{-/2-}$	–1.81	–1.69	
$(\mathbf{HL^B})^{0/-}$	–1.18	–1.12	–1.21
$[Ga(\mathbf{L^B})_2]^{+/0}$	–1.35	–0.86	–0.93
$[Fe(\mathbf{L^B})_2]^{0/-}$	–2.00	–1.56	–1.61

Table S3. Relative energies (in kcal/mol) of plausible electronic states of $[Fe^{II}(\mathbf{L^B})_2]$ and $[Fe^{II}(\mathbf{L^B})_2]^-$

	multiplicity	B3LYP	BP86
$[Fe^{II}(\mathbf{L^B})_2]$	1	10.6	0
	3	5.9	15.0
	5	0	20.6
$[Fe^{II}(\mathbf{L^B})_2]^-$	2	13.5	0
	4	0	6.3

Table S4. Calculated partial charges on the ligands and on the metal or hydrogen

		Mulliken (lb)[a]		Mulliken (sb)[b]		ESP (sb)[c]		Hirshfeld[d]	
Compound	moiety	ox	red	ox	red	ox	red	ox	red
$(\mathbf{L}^{\mathbf{B}})^{-/2-}$		–1.00	–2.00	–1.00	–2.00	–1.00	–2.00	–1.00	–2.00
$(\mathbf{HL}^{\mathbf{B}})^{0/-}$	H	0.30	0.29	0.29	0.28	–0.04	–0.01	0.08	0.07
	L	–0.30	–1.29	–0.29	–1.28	0.04	–0.99	–0.08	–1.07
$[Ga(\mathbf{L}^{\mathbf{B}})_2]^{+/0}$	Ga	1.90	1.92	0.94	1.00	0.42	0.48	0.32	0.32
	L	–0.45	–0.96	0.03	–0.50	0.29	–0.24	0.34	–0.16
$[Fe(\mathbf{L}^{\mathbf{B}})_2]^{0/-}$	Fe	–0.82	–0.84	–0.02	–0.02	–0.16	–0.10	0.02	0.02
	L	0.41	–0.08	0.01	–0.49	0.08	–0.45	–0.01	–0.51

[a] Large basis set. Totally uncontracted LANL2DZ on Ga and augmented with one set of f functions on Fe, together with the 6-311+G(d,p) basis sets on the other atoms, and the 6-311+G(3d) on S.

[b] Small basis set. LANL2DZ on the metal, 6-31G(d,p) on the other atoms.

[c] Same small basis set, denoted LACVP** in Jaguar.

[d] Scalar relativistic ZORA, TZV2P basis on the metals and TZVP basis set on the other atoms.

Table S5. Calculated bond lengths (in Å)

		C1–S		C1–N1		N1–N2		N2–C2		C2-C3		C3–N3		Metal–S		Metal–N2		Metal–N3	
Compound		ox	red	ox	red	ox	red	ox	red	ox	red	ox	red	ox	red	ox	red	ox	red
$(\mathbf{L}^{\mathbf{B}})^{-/2-}$	Calc	1.719	1.757	1.364	1.327	1.340	1.373	1.331	1.356	1.464	1.442	1.373	1.414						
$(\mathbf{HL}^{\mathbf{B}})^{0/-}$	Calc	1.713	1.739	1.389	1.343	1.327	1.360	1.328	1.364	1.466	1.428	1.362	1.395						
	X-ray[a]	1.723		1.350		1.353		1.299		1.474		1.352							
$[Ga(\mathbf{L}^{\mathbf{B}})_2]^{+/-}$	Calc	1.755	1.759	1.362	1.346	1.338	1.355	1.331	1.343	1.464	1.445	1.370	1.387	2.412	2.453	2.089	2.057	2.141	2.119
	X-ray[b]	1.741		1.342		1.356		1.304		1.465		1.361		2.373		2.032		2.131	
$[Fe(\mathbf{L}^{\mathbf{B}})_2]^{0/-}$	Calc	1.747	1.752	1.349	1.336	1.358	1.369	1.344	1.355	1.442	1.428	1.383	1.400	2.318	2.341	1.902	1.902	1.942	1.944

$(L^B)^-$ 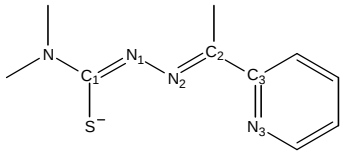

HL^B 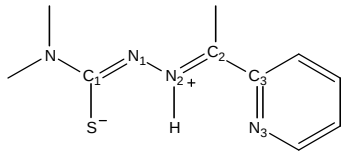

$[M(L^B)_2]$ 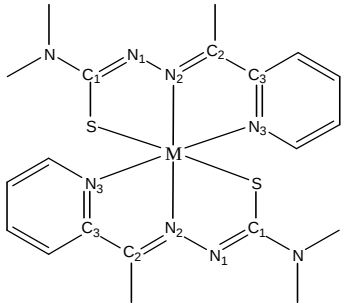

[a] Kowol, C. R.; Eichinger, R.; Jakupec, M. A.; Galanski, M.; Arion, V. B.; Keppler, B. K. J. Inorg. Biochem. **2007**, *101*, 1946.

[b] Arion, V. B.; Jakupec, M. A.; Galanski, M.; Unfried, P.; Keppler, B.K. J. Inorg. Biochem. **2002**, *91*, 298.

V.8. References

(1) Reisner, E.; Arion, V. B.; Keppler, B. K.; Pombeiro, A. J. L. *Inorg. Chim. Acta* **2008**, *361*, 1569.

(2) Clarke, M. J.; Zhu, F.; Frasca, D. R. *Chem. Rev*. **1999**, *99*, 2511.

(3) Hall, M. D.; Hambley, T. W. *Coord. Chem. Rev*. **2002**, *232*, 49.

(4) Alessio, E.; Mestroni, G.; Bergamo, A.; Sava, G. *Curr. Top. Med. Chem*. **2004**, *4*, 1525.

(5) Clarke, M. J. *Coord. Chem. Rev*. **2003**, *236*, 209.

(6) Hartinger, C. G.; Zorbas-Seifried, S.; Jakupec, M. A.; Kynast, B.; Zorbas, H.; Keppler, B. K. *J. Inorg. Biochem.* **2006**, *100*, 891.

(7) Hall, M. D.; Amjadi, S.; Zhang, M.; Beale, P.J.; Hambley, T. W. *J. Inorg. Biochem.* **2004**, *98*, 1614.

(8) Jakupec, M. A.; Reisner, E.; Eichinger, A.; Pongratz, M.; Arion, V. B.; Galanski, M.; Hartinger, C. G.; Keppler, B. K. *J. Med. Chem.* **2005**, *48*, 2831.

(9) Lever, A. B. P. *Inorg. Chem*. **1990**, *29*, 1271.

(10) Reisner, E.; Arion, V. B.; Eichinger, A.; Kandler, N.; Giester, G.; Pombeiro, A. J. L.; Keppler, B. K. *Inorg. Chem*. **2005**, *44*, 6704.

(11) Brown, J. M. *Cancer Res.* **1999**, *59*, 5863.

(12) Top, S.; Tang, J.; Vessieres, A.; Carrez, D.; Provot, C.; Jaouen, G. *Chem. Commun*. **1996**, 955.

(13) Hillard, E.; Vessieres, A.; Thouin, L.; Jaouen, G.; Amatore, C. *Angew. Chem., Int. Ed.* **2006**, *45*, 285.

(14) (a) Gerbeleu, N. V.; Arion, V. B.; Burgess, J. *Template Synthesis of Macrocyclic Compunds*, Wiley-VCH, Weinheim, 1999, Chapter 2. (b)Casas, J. S.; Garcia-Tasende, M. S.; Sordo, J. *Coord. Chem. Rev.* **2000**, *209*, 197.

(15) West, D. X.; Padhye, S. B.; Sonawane, P. B. *Struct. Bond.* **1991**, *76*, 1.

(16) Moore, E. C.; Zedeck, M. S.; Agrawal, K. C.; Sartorelli, A. C. *Biochemistry* **1970**, *9*, 4492.

(17) Shao, J.; Zhou, B.; Chu, B.; Yen, Y. *Curr. Cancer Drug Targets* **2006**, *6*, 409.

(18) Saryan, L. A.; Ankel, E.; Krishnamurti, C.; Petering, D. H. *J. Med. Chem.* **1979**, *22*, 1218.

(19) Preidecker, P. J.; Agrawal, K. C.; Sartorelli, A. C.; Moore, E. C. *Mol. Pharmacol.* **1980**, *18*, 507.

(20) Thelander, L.; Gräslund, A. *J. Biol. Chem.* **1983**, *258*, 4063.

(21) Finch, R. A.; Liu, M.-C.; Cory, A. H.; Cory, J. G.; Sartorelli, A. C. *Adv. Enzyme Regul.* **1999**, *39*, 3.

(22) Kowol, C. R.; Berger, R.; Eichinger, R.; Roller, A.; Jakupec, M. A.; Schmidt, P. P.; Arion, V. B.; Keppler, B. K. *J. Med. Chem.* **2007**, *50*, 1254.

(23) Shao, J.; Zhou, B.; Di Bilio, A. J.; Zhu, L.; Wang, T.; Qi, C.; Shih, J.; Yen, Y. *Mol. Cancer Ther.* **2006**, *5*, 586.

(24) Geske, D. H.; Ragle, J. L.; Bambenek, M. A.; Balch, A. L. *J. Am. Chem. Soc.* **1964**, *86*, 987.

(25) Castle, T. C.; Maurer, R. I.; Sowrey, F. E.; Went, M. J.; Reynolds, C. A.; McInnes, E. J. L.; Blower, P. J. *J. Amer. Chem. Soc.* **2003**, *125*, 10040.

(26) Kowol, C. R.; Eichinger, R.; Jakupec, M. A.; Galanski, M.; Arion, V. B.; Keppler, B. K. *J. Inorg. Biochem.* **2007**, *101*, 1946.

(27) *CRC Handbook of Chemistry and Physics*, ed. D. R. Lide, CRC Press, 2004.

(28) Nunez-Vergara, L. J.; Bonta, M.; Navarrete-Encina, P. A.; Squella, J. A. *Electrochim. Acta* **2001**, *46*, 4289.

(29) Reisner, E., Arion, V. B.; Guedes da Silva, M. F. C.; Lichtenecker, R.; Eichinger, A.; Keppler, B. K.; Kukushkin, V. Yu.; Pombeiro, A. J. L. *Inorg. Chem.* **2004**, *43*, 7083.

(30) Maji, M.; Ghosh, S.; Chattopadhyay, S. K.; Mak, T. C. W. *Inorg. Chem.* **1997**, *36*, 2938.

(31) Prabhakaran, R.; Renukadevi, S. V.; Karvembu, R.; Huang, R.; Mautz, J.; Huttner, G.; Subashkumar, R.; Natarajan, K. *Eur. J. Med. Chem.* **2008**, *43*, 268.

(32) Sengupta, P.; Dinda, R.; Ghosh, S.; Sheldrick, W. S. *Polyhedron* **2003**, *22*, 447.

(33) Ainscough E. W.; Brodie A. M.; Denny W. A.; Finlay G. J.; Ranford J. D. *J. Inorg. Biochem.* **1998**, *70*, 175.

(34) Kovala-Demertzi, D.; Domopoulou, A.; Demertzis, M. A.; Papageorgiou, A.; West, D. X. *Polyhedron* **1997**, *16*, 3625.

(35) Costa, R. F. F.; Rebolledo, A. P.; Matencio, T.; Calado, H. D. R.; Ardisson, J. D.; Cortes, M. E.; Rodrigues, B. L.; Beraldo, H. *J. Coord. Chem.* **2005**, *58*, 1307.

(36) Graminha, A. E.; Vilhena F. S.; Batista A. A.; Louro S. R. W.; Ziolli R. L.; Teixeira L. R.; Beraldo H. *Polyhedron* **2008**, *27*, 547.

(37) Aguirre, M.; Borras, J.; Castineiras, A.; Garcia-Monteagudo, J. M.; Garcia-Santos, I.; Niclos, J.; West, D. X. *Eur. J. Inorg. Chem.* **2006**, 1231.

(38) Adsule, S.; Barve, V.; Chen, D.; Ahmed, F.; Dou, Q. P.; Padhye, S.; Sarkar, F. H. *J. Med. Chem.* **2006**, *49*, 7242.

(39) Chattopadhyay S. K.; Chattopadhyay D.; Banerjee T.; Kuroda R.; Ghosh S. *Polyhedron* **1997**, *16*, 1925.

(40) Demertzis M. A.; Yadav P. N.; Kovala-Demertzi D. *Helv. Chim. Acta* **2006**, *89*, 1959.

(41) Pessoa M. M. B.; Andrade G. F. S.; dos Santos M. R.; Temperini M. L. A. *J. Electroanal. Chem.* **2003**, *545*, 117.

(42) Vire, J. C.; De Jager, R. L.; Dupont, D. G.; Patriarche, G. J.; Christian, G. D. *Fresenius J. Anal. Chem.* **1981**, *307*, 277.

(43) Kovala-Demertzi, D.; Domopoulou, A.; Demertzis, M. A.; Valdes-Martinez, J.; Hernandez-Ortega, S.; Espinosa-Perez, G.; West, D. X.; Salberg, M. M.; Bain, G. A.; Bloom, P. D. *Polyhedron* **1996**, *15*, 2587.

(44) (a) Becke, A. D. *J. Chem. Phys.* **1993**, *98*, 5648–5652. (b) Lee, C.; Yang, W.; Parr, R. G. *Phys. Rev. B* **1988**, *37*, 785.

(45) Gaussian 03, Revision D.01, Frisch, M. J. et al., Gaussian, Inc., Wallingford CT, 2004. www.gaussian.com.

(46) (a) Wadt, W. R.; Hay, P. J. *J. Chem. Phys.* **1985**, *82*, 284–298. (b) Hay, P. J.; Wadt, W. R. *J. Chem. Phys.* **1985**, *82*, 299.

(47) (a) Becke, A. D. *Phys. Rev. A* **1988**, *38*, 3098–3100. (b) Perdew, J. P. *Phys. Rev. B* **1986**, *33*, 8822.

(48) Ehlers, A. W.; Böhme, M.; Dapprich, S.; Gobbi, A.; Höllwarth, A.; Jonas, V.; Köhler, K. F.; Stegmann, R.; Veldkamp, A.; Frenking, G. *Chem. Phys. Lett.* **1993**, *208*, 111.

(49) Chiorescu, I.; Deubel, D. V.; Arion, V. B.; Keppler, B. K. *J. Chem. Theory Comput.* **2008**, *4*, 499.

(50) (a) Tannor, D. J.; Marten, B.; Murphy, R. B.; Friesner, R. A.; Sitkoff, D.; Nicholls, A.; Ringnalda, M. N.; Goddard, W. A., III; Honig, B. *J. Am. Chem. Soc.* **1994**, *116*, 11875.

(b) Marten, B.; Kim, K.; Cortis, C.; Friesner, R. A.; Murphy, R. B.; Ringnalda, M. N.; Sitkoff, D.; Honig, B. *J. Phys. Chem.* **1996**, *100*, 11775.

(51) Jaguar, version 7.0, Schrödinger, LCC, New York, NY, 2007. www.schrodinger.com.

(52) (a) Ketterer, N. A.; Fan, H.; Blackmore K. J.; Yang, X.; Ziller, J. W.; Baik, M.-H.; Heyduk, A. F. *J. Am. Chem. Soc.* **2008**, *130*, 4364. (b) Reiher, M.; Salomon, O.; Hess, B. A. *Theor. Chem. Acc.* **2001**, *107*, 48. (c) Fouqueau, A.; Casida, M. E.; Daku, L. M. L.; Hauser, A.; Neese, F. *J. Chem. Phys.* **2005**, *122*, 44110/1.

(53) (a) Mulliken, R. S. *J. Chem. Phys.* **1955**, *23*, 1833–1840. (b) Hirshfeld, F. L. *Theor. Chim. Acta* **1977**, *44*, 129. (c) Chirlian, L. E.; Miller, M. *J. Comput. Chem.* **1987**, *8*, 894.

(54) (a) te Velde, G.; Bickelhaupt, F.M.; van Gisbergen S. J. A.; Fonseca Guerra, C.; Baerends, E. J.; Snijders, J.G.; Ziegler, T. *J. Comput. Chem.* **2001,** *22*, 931. (b) ADF2007.01, SCM, Theoretical Chemistry, Vrije Universiteit, Amsterdam, The Netherlands. http://www.scm.com.

Curriculum Vitae

Ion Chiorescu

Contact Information

e-mail: ion.chiorescu@univie.ac.at
current address: Institute of Inorganic Chemistry, University of Vienna, Währinger Str. 42, A-1090 Vienna, Austria.
phone: +43 650 7614668

Personal Information

Date of birth: 27.05.1979
Place of birth: Singerei, Republic of Moldova
Marital status: single
Languages: Romanian (native), Russian (native), English (fluent), French (fluent), German (basics)

Education

2004- PhD student, Institute of Inorganic Chemistry, Vienna, Austria

2001-2003 Master in Physical Chemistry (in French), University of Bucharest. Research assistant in the laboratory of molecular structure of the Institute of Physical Chemistry "I.G. Murgulescu", Bucharest, Romania

February 2003-July 2003 visiting scholarship Marseille, Université de Provence

1997-2001 Chemistry studies, Faculty of Chemistry, University of Bucharest

1996-1997 Chemistry studies, Faculty of Chemistry, State University of Moldova, Chisinau, Moldova

1993-1996 High School "Mihai Eminescu", profile Chemistry-Biology, Singerei, Moldova

Publications

Chiorescu, I.; Deubel, D. V.; Arion, V. B.; Keppler, B. K. "Quantum Chemical Studies of Ruthenium(III) Anticancer Complexes" *in preparation*.

Kowol, C. R.; Reisner, E.; **Chiorescu, I.**; Arion, V. B.; Galanski, M.; Deubel, D. V.; Keppler, B. K. "An electrochemical study of antineoplastic gallium, iron and ruthenium complexes with redox non-innocent α-N-heterocyclic chalcogensemicarbazones" *Inorg. Chem.* **2008**, *47*, 11032–11047.

Chiorescu, I.; Deubel, D. V.; Arion, V. B.; Keppler, B. K. "Computational electrochemistry of ruthenium anticancer agents. Unprecedented benchmarking of implicit solvation methods" *J. Chem Theory Comput.* **2008**, *4*, 499–506.

Bicker, W.; **Chiorescu, I.**; Arion, V. B.; Lämmerhofer, M.; Lindner, W. "Contributions to chromatographic chiral recognition of permethrinic acid stereoisomers by a quinine carbamate chiral selector: evidence from X-ray diffraction, DFT computations, NMR and thermodynamic studies" *Tetrahedron: Asymmetry* **2008**, *19*, 97–110.

Schmid, W. F.; Zorbas-Seifried, S.; John, R. O.; Arion, V. B.; Jakupec, M. A.; Roller, A.; Galanski, M.; **Chiorescu, I.**; Zorbas, H.; Keppler, B. K. "The First Ruthenium-Based Paullones: Syntheses, X-ray Diffraction Structures, and Spectroscopic and Antiproliferative Properties in Vitro" *Inorg. Chem.* **2007**, *46*, 3645.

Reisner, E.; Arion, V. B.; Rufinska, A.; **Chiorescu**, **I.**; Schmid; W. F.; Keppler, B. K. "Isomeric $[RuCl_2(dmso)_2(indazole)_2]$ complexes: ruthenium(II)-mediated coupling reaction of acetonitrile with 1*H*-indazole" *Dalton Trans*. **2005**, *14*, 2355.

Constantinescu, T.; Ionita, P.; **Chiorescu**, **I.**; Ionita G. "Hydrazyl, Nitronyl-, and Imino-Nitroxides: Synthesis, Properties and Reaction with Nitric Oxide and Nitrogen Dioxide" *Centr. Eur. J. Chem.* **2003**, *1*, 465.

Ionescu, S.; **Chiorescu, I.**; Hillebrand, M. "Theoretical study of non-radiative deactivation pathways for some heterocyclic compounds. I. Pyrrolyl-izoxazole derivatives" *J. Mol. Str. THEOCHEM*, **2003**, *630*, 125.

Conference Contributions

Chiorescu I. "Computational Electrochemistry of Ruthenium Anticancer Agents" Oral presentation, COST meeting during 9th European Biological Inorganic Chemistry Conference (EUROBIC 9), Wroclaw, Poland. September 4-5, **2008**.

Chiorescu I. "Computational Electrochemistry of Ruthenium Anticancer Agents" Oral presentation, Workshop "*Anorganische Chemie in Österreich*", Graz, Austria. March 17-18, **2008**, P. 20.

Chiorescu, I.; Stepanenko, I. N.; Arion, V. B.; Krokhin, A. A.; Keppler, B. K. "Theoretical studies on $OsCl_3(azole)_3$: isomerism, redox properties, electronic and vibrational spectra" Abstracts of the 13th International Conference on Biological Inorganic Chemistry, Vienna, Austria. July 15-20, **2007**, P456, S226.

Chiorescu I., Stepanenko I. N., Arion V. B., Krokhin A. A., Scaffidi-Domianello Y. Yu., Keppler B. K. "Geometrical Isomerism in $OsCl_3(azole)_3$: a Density Functional Theory Study" Abstracts of EUROBIC 8 **(***8th European Biological Inorganic Chemistry Conference*), Aveiro, Portugal. July 2-7, **2006**, PS7.17, P. 333.

Chiorescu I. "Density Functional Theory Investigation of Geometrical Isomerism in $[Ru^{II}Cl_2(dmso)_2(ind)_2]$" Oral Presentation *Workshop Anorganische Chemie in Österreich (4.WACÖ)*, Eisenstadt, Austria. April 10-11, **2006**.

Chiorescu, I.; Reisner, E.; Arion, V. B.; Keppler B. K. "Geometrical Isomerism in $[RuCl_2(dmso)_2(ind)_2]$: a Density Functional Study" Symposium: "*Novel Approaches for Discovery and the Development of Anticancer Agents"* CESAR, Vienna, Austria. July 7-9, **2005**.

Bandula, R.; Caragheorgheopol, A.; **Chiorescu, I.**; Savonea, F. "Investigation of the micropolarity in ternary block copolymer–organic solvent–technical toilets systems by absorption honest" *3rd International Conference of the Chemical Societies of the South-Eastern Countries,* Bucharest, Romania. September 22-25, **2002.**

Ionescu, S.; **Chiorescu**, **I.**; Hillebrand, M. "Molecular modelling of the excited states of some heteroaromatic derivatives" *3rd International Conference of the Chemical Societies of the South-Eastern Countries,* Bucharest, Romania. September 22-25, **2002**.

Ionescu, S.; **Chiorescu, I.**; Hillebrand, M. "Theoretical study of non-radiative deactivation pathways for some heterocyclic compounds. Pyrrolyl-izoxazole derivatives " *6th World Congress of Theoretically Oriented Chemists,* Lugano, Switzerland. August 4-9, **2002**.

Chiorescu, I.; Ionescu, S.; Merisor, E.; Maior, O.; Hillebrand, M. "Theoretical studies of non-radiative deactivation pathways for some pyrrolyl-izoxazole derivatives" *International conference on Chemistry and Chemical Engineering*, Bucharest, Romania. September 13-15, **2001**.